NORTHWESTERN UNIVERSITY

Modeling the dynamical neural systems on different timescales

A DISSERTATION

SUBMITTED TO THE GRADUATE SCHOOL

IN PARTIAL FULFILLMENT OF THE REQUIREMENTS

for the degree

DOCTOR OF PHILOSOPHY

Field of Engineering Sciences and Applied Mathematics

By

Xize Xu

EVANSTON, ILLINOIS

September 2021

ABSTRACT

Modeling the dynamical neural systems on different timescales

Xize Xu

With neurons as its primary computational components, the brain operates at multiple timescales. In this thesis, we focus on two timescales: on a relatively slow timescale on the order of hours to days, the brain adapts to the environment it is exposed to and learns its circuitry by altering the connections between neurons through synaptic plasticity; on a relatively fast timescale on the order of tens of milliseconds, collective oscillations or brain rhythms emerge from synaptic interactions within neuronal circuits, which have been suggested to play an important role in routing information across cortical regions.

In Chapter 2, we explore how learning in visual cortex is achieved by synaptic plasticity, particularly in a model of binocular matching of orientation selectivity in mouse primary visual cortex (V1). Right after eye-opening, binocular cells in mouse V1 have different preferred orientations for input from the two eyes. With normal visual experience during a critical period, these preferred orientations evolve

and eventually become well matched. To gain insight into the matching process, we develop a computational model of a cortical cell receiving orientation-selective inputs via plastic synapses. The model captures the experimentally observed matching of the preferred orientations, the dependence of matching on ocular dominance of the cell, and the relationship between the degree of matching and the resulting monocular orientation selectivity. Moreover, our model puts forward testable predictions: i) The matching speed increases with initial ocular dominance; ii) While the matching improves more slowly for cells that are more orientation-selective, the selectivity increases faster for better matched cells during the matching process. This suggests that matching drives orientation selectivity but not vice versa; iii) there are two main routes to matching: the preferred orientations either drift towards each other or one of the orientations switches suddenly. The latter occurs for cells with large initial mismatch and can render the cells monocular.

In Chapter 3, we investigate the synchronization of different γ-rhythms arising in different brain areas, which has been implicated in various cognitive functions. In particular, we focus on the effect of ubiquitous neuronal heterogeneity on the synchronization of ING (interneuronal network gamma) and PING (pyramidal-interneuronal network gamma) rhythms. The synchronization properties of rhythms depend on the response of their collective phase to external input. We therefore determine the macroscopic phase-response curve for finite-amplitude perturbations (fmPRC) of ING- and PING-rhythms in all-to-all coupled networks comprised of linear (IF) or quadratic (QIF) integrate-and-fire neurons. For the QIF networks we complement

the direct simulations with the adjoint method to determine the infinitesimal macroscopic PRC (imPRC) within the exact mean-field theory. We show that intrinsic neuronal heterogeneity can qualitatively modify the fmPRC and the imPRC. Both PRCs can be biphasic and change sign (type II), even though the phase-response curve for the individual neurons is strictly non-negative (type I). Thus, for ING rhythms, external inhibition to the inhibitory cells can, in fact, advance the collective oscillation of the network, even though the same inhibition would lead to a delay when applied to uncoupled neurons. This paradoxical advance arises when the external inhibition modifies the internal dynamics of the network by reducing the number of spikes of inhibitory neurons; the advance resulting from this disinhibition outweighs the immediate delay caused by the external inhibition. These results explain how intrinsic heterogeneity allows ING- and PING-rhythms to become synchronized with a periodic forcing or another rhythm for a wider range of frequency mismatches. Our results identify a potential function of neuronal heterogeneity in the synchronization of coupled γ-rhythms, which may play a role in neural information transfer via communication through coherence.

Acknowledgments

This thesis marks the end of my Ph.D. career. I could not have survived it on my own. I am grateful to a lot of people along the way. My clumsy writing may not express how much I appreciate the support from you, but I will try my best.

First of all, I would like to thank my advisor, Professor Hermann Riecke, for giving me the opportunity to be a Ph.D. student and providing great support throughout my graduate career. It is my honor working with him, through which I have learned so many good qualities as a researcher. Moreover, I am grateful for his incredible patience with my unsatisfying English skills, presentation skills, slowness in understanding and procrastination. Whenever I get discouraged or need help, he has always been there with enthusiasm and wisdom to support and guide me, even though sometimes it is his nap time in the early afternoon. Also, I want to thank Marge, Charlie, Toby and Sasha for inviting me at family dinners.

I also would like to thank Professor William Kath and Professor Danny Abrams for being on my thesis committee and reviewing this thesis with their busy schedule. I was always nervous and intermittently blanked out when I presented my research to them in the qualification exam and every annual progress report. They are strict but encouraging. I have benefited a lot from their comments and suggestions on my research, presentation skill and postdoc searching. Moreover, I enjoyed the eight

courses instructed by them despite that I paid for six courses of eight as a master student.

I thank our lab collaborator Professor Jianhua Cang, who is at The University of Virginia. During the collaboration, he provided great insights, supports and suggestions. The experience of interacting with his lab has enhanced my ability to explain and write about computational results with biology perspectives in mind. Most of all, through working with him, I have learned the joy of collaborative research.

I appreciate all my friends who have provided great support and encouragement during my graduate career. In particular, many thanks to lab fellows Hongyu Meng, Avinash Karamchandani, Lae Kim, Angelia Wang, who have made my daily life in Northwestern funny and distracted. Moreover, special thanks to Dr. Rui Yan. We have known each other since mid-school. Even though we do research in different areas, he has always been willing to help whenever I had questions in the experimental side of neuroscience.

The biggest gift from the six years of life at Northwestern is knowing my wife, who has brought great enjoyment and laughter into my life. We are blessed with the opportunity to stay together during my Ph.D. career because she has been able to study in The University of Chicago. She stands strong beside me through the ebb and flow of my graduate life. I am grateful for all her care and love in this journey, as well as the delicious foods she cooks.

Last but not least, I thank my parents in China. The video chat with them is the most relaxing and enjoyable moment of every week. They are always the first

ones I turn to when I want to blow off steam. They know little about my research, but they know how to comfort and inspire me best. We sometimes quarreled, again, only because they know how to comfort and inspire me best.

I dedicate this thesis to my loving grand uncle, Wenyuan Zhang, who brought great fun and taught me a wide range of knowledge during my childhood.

Table of Contents

List of Figures

List of Tables

CHAPTER 1

Introduction

With about one hundred billion neurons continuously interacting with thousands of other neurons by electrical signals via hundreds of trillions of tiny specialized structures called synapses, our brain is one of the most sophisticated architecture in nature. At every single instant of time, our brain undergoes a complex process, which receives information from the external environment, analyzes the corresponding situations and then makes decisions accordingly. Mathematical modeling based on experimental data has been proven to be a powerful tool to study the computational principle of the neural system in the brain. Not only can the modeling reproduce the experimental result but also generate meaningful and testable predictions, which in turn guide experimental designs. Moreover, mathematical modeling enables one to explore various situations in the brain that cannot be tested experimentally. Much of mathematical modeling in neuroscience concerns dynamical systems. In the brain, there are multiple interacting dynamical systems operating on timescales from milliseconds to years.

On the milliseconds scale, single neurons fire action potentials to propagate signals between each other: when an action potential occurs, an electrical signal is emitted through the presynaptic axon. Such an electrical signal causes neurotransmitter

to be released into the synaptic cleft and attach to the postsynaptic neurotransmitter receptor, allowing ions to cross the postsynaptic membrane and causing the membrane potential to change. Moreover, the synaptic interactions within neuronal circuits can give rise to collective oscillations or rhythms in frequency bands on various timescales: delta (1–4 Hz), theta (4–8 Hz), alpha (8-12), beta (13–30 Hz), gamma (30–100 Hz). The collective oscillations are characterized by their frequency, amplitude and phase. The amplitude of collective oscillations, which measures the extent of local synchronization in a neural ensemble, has been linked to various cognitive functions. Such macroscopic rhythms have been suggested to play an important role in routing information across cortical regions. The coherence of rhythms between brain areas has been reported and is suggested to be associated with cognitive tasks such as selective attention [**1**].

On a slower timescale, synaptic plasticity occurs. Synaptic plasticity refers to the activity-dependent changes in the effect of a synaptic signal from one neuron to another. The expression of synaptic plasticity concerns a large range of timescales from milliseconds to months. Depending on the function and the timescale it operates on, synaptic plasticity can be divided into three categories: i) Short-term plasticity, which takes place on a milliseconds-to-minutes timescale [**2**], allows synapses to play a number of computational functions in neural circuits including neural coding and information processing [**3**]. It has also been considered as one of the neural mechanisms subserving short-term working memory [**4**]. ii) Homeostatic plasticity, which is also referred to as 'synaptic scaling', occurs on a slower timescale on the order of

hours to days [**5**]. It plays a critical role in stabilizing synaptic connectivity during experience-dependent plasticity and protein turnover as well as preventing the firing rates from becoming saturated during developmental changes in synaptic inputs [**6**]. iii) Long-term plasticity, which includes long-term potentiation (LTP) and long-term depression (LTD), involves changes in synaptic strength lasting for minutes or longer. It is considered as the primary mechanism for learning and memory [**7**, **8**], in which the consolidation process takes hours or longer. Furthermore, long-term plasticity occurs drastically during the developmental phase of the sensory system [**9**].

In this thesis, we explore the dynamics of two neural mechanisms operating on different timescales. In Chapter 2, we investigate how the learning in visual cortex is achieved by long-term synaptic plasticity, particularly in a model of binocular matching of orientation selectivity in mouse V1. We develop a computational model of a cortical cell receiving orientation-selective inputs via plastic synapses, which captures key experimental results and puts forward testable predictions. This result has been published [**10**]. In Chapter 3, we investigate the synchronization of different γ-rhythms (30-100 Hz) arising in different brain areas. In particular, we focus on the effect of the ubiquitous neuronal heterogeneity on the synchronization of ING (interneuronal network gamma) and PING (pyramidal-interneuronal network gamma) rhythms. We show that the intrinsic neuronal heterogeneity can qualitatively modify the fmPRC and the imPRC of both PING and ING rhythm, which enhances their ability to be synchronized with a periodic forcing or another rhythm for a wider range in the mismatch of their frequencies. This result has also been published [**11**].

CHAPTER 2

Development and binocular matching of orientation selectivity in visual cortex: a computational model

2.1. Introduction

Animals receive information about the world through multiple modalities (vision, audition, touch, etc). For these information streams to provide a meaningful representation of the sensory world they have to be merged in a coherent fashion; only then do they enable the brain to better detect events, analyze the corresponding situations and then make decisions accordingly. Typically, this coherence is only acquired during a postnatal critical period [**12**].

The merging of across-modality information has been extensively investigated in the cat superior colliculus (SC) [**13**–**16**] as well as the optic tectum of the barn owl [**17**], where multisensory neurons integrate the information they receive from upstream unisensory neurons in different sensory channels (e.g., visual and auditory). Like in other sensory systems, the capability of SC multisensory neurons to engage in multisensory integration is not innate but learned gradually during postnatal life as a consequence of normal multisensory experience. Two main results of the multisensory neurons' learning process in SC are the initial development of large, unisensory receptive fields for visual and auditory input and their subsequent contraction and

matching across modalities. This can enhance the degree to which the neurons' receptive fields for visual and auditory inputs pertain to the same spatial location and enables the neuron to extract coherent information from the different modalities.

Matching of different information streams can also play an important role within a single modality. In the visual system, for instance, neurons in the visual cortex prefer similar orientations through the two eyes. As in the multisensory case, this binocular matching requires normal sensory experience. Shortly after eye-opening cortical cells in layer 2/3 of mouse visual cortex V1 have quite different monocular preferred orientations through each eye [**18**]. With normal binocular visual experience these preferences become binocularly matched to the adult level by postnatal day 31 (P31) [**18**], which corresponds to the end of the critical period for ocular dominance plasticity [**19**].

Inspired by these experimental results and to gain insight into general matching mechanisms, we developed a computational model for the development and matching of input preferences of neurons receiving multi-channel input via plastic synapses. In the case of multisensory SC neurons the input preferences would correspond to visual and auditory receptive fields. For concreteness, we will focus here on the binocular matching in V1, where the input preferences correspond to orientation preferences.

The development of visual cortex has been studied extensively over the years. Many studies have used a firing-rate framework for the neurons as well as for the synaptic plasticity [**20**], which assumes, in particular, that the pre- and postsynaptic spike trains are uncorrelated. Since the spiking of cortical cells is driven by

fluctuations in the input rather than its mean [**21**], it is not clear whether the correlations are sufficiently negligible. We therefore considered a single spiking neuron with synapses whose plasticity is spike-dependent [**22**]. It received separate inputs from each eye. Motivated by the fact that in a multi-source system upstream neurons gain selectivity before the downstream neurons [**12**, **23**], we chose the inputs from the upstream neurons to be orientation-selective. This is consistent with complex cells in V1 receiving oriented inputs from simple cells. The evolution of the synaptic weights was driven by stimuli representing gratings with randomly switching orientation. In an initial phase these inputs were uncorrelated between the two eyes to mimic spontaneous retinal or thalamic activity before eye opening [**24**]. After eye-opening the inputs were chosen to be perfectly correlated between left and right. Our aim was to keep the model as simple as possible, while still capturing a wide range of experimental observations. We therefore did not modify the plasticity rules when switching between these two phases and did not include a transition period (P15-P20) during which the input changes from being dominated by spontaneous activity to being dominated by visually-evoked activity [**25**].

Our model captures key experimental observations [**23**, **26**]:

(1) the matching is predominantly achieved by shifting the preferred orientation for input from the weaker eye.

(2) the resulting binocular orientation selectivity increases with decreasing mismatch.

In addition, the model provides insight into a number of further experimental observations and puts forward testable predictions:

(1) The matching speed increases with initial ocular dominance, suggesting ocular dominance as a key driver of the binocular matching process.

(2) While the matching improves more slowly for cells that are more orientation-selective, the selectivity increases faster for better matched cells during the matching process. This suggests that matching drives orientation selectivity but not vice versa

(3) The initial binocular preferred orientation is a good predictor for the matching outcome.

(4) There are two main routes to matching: the preferred orientations either drift towards each other or one of the orientations switches quite suddenly, involving a transient loss of binocularity, which can become permanent if it occurs towards the end of the critical period. While drifting occurs for small initial mismatch, switching is specific for large mismatch.

We expect that these results provide insight more generally into how neuronal systems can develop to integrate inputs from multiple sources coherently in order to generate normal neuronal function.

2.2. Methods

2.2.1. Neuron model

We used an adaptive exponential integrate-and-fire model [**27**] with an additional current describing an afterpotential depolarization [**28**]. In this model the evolution of the postsynaptic membrane potential $u(t)$ was given by

$$C\frac{d}{dt}u = -g_L(u - E_r) + g_L\Delta_T e^{\frac{u-V_T}{\Delta_T}} - w_{ad} + z + I\,, \tag{2.1}$$

where E_r was approximately the resting potential, C the membrane capacitance, g_L the leak conductance, and I the current stimulation. The exponential term mimicked the activation of sodium current. Upon reaching the peak voltage V_{peak}, the voltage u was reset to the fixed value V_{reset} . The parameter Δ_T was the slope factor and V_T was the (variable) threshold potential. The variable w_{ad} represented a hyperpolarizing adaptation current with dynamics given by

$$\tau_{w_{ad}}\frac{d}{dt}w_{ad} = a(u - E_r) - w_{ad}\,, \tag{2.2}$$

where $\tau_{w_{ad}}$ was the time constant of the adaptation of the neuron and a controlled the strength with which w_{ad} was driven. On firing, w_{ad} was increased by an amount b. The afterpotential depolarization was captured by the variable z. It was set to I_{sp} immediately after a spike and decayed then with a time constant τ_z,

$$\tau_z\frac{d}{dt}z = -z\,. \tag{2.3}$$

Refractoriness was modeled by employing an adaptive threshold V_T, which was set to $V_{T_{max}}$ immediately after a spike and decayed then to $V_{T_{rest}}$ with a time constant τ_{V_T},

$$\tau_{V_T} \frac{d}{dt} V_T = -(V_T - V_{T_{rest}}) \,. \tag{2.4}$$

Parameters for the neuron were taken from [**22**] and kept fixed throughout all simulations (see Table 2.1).

To test the robustness of our results we also used a simplified neuron model with both the adaptation current and afterdepolarization removed, with which we obtained very similar results.

2.2.2. Synaptic Inputs

Our model consisted of one postsynaptic binocular cell modeling a cortical cell in V1 receiving excitatory, tuned synaptic inputs (Fig.2.1A), driven by independent Poisson spike trains. In the first set of simulations these inputs were taken to be monocular. They were divided equally into 250 inputs from the left and 250 from the right eye, respectively. In addition, inhibitory, untuned synaptic inputs were introduced to capture the sublinear binocular integration observed experimentally [**29**] (Fig.2.2A). The monocular preferred orientations of the tuned excitatory synapses were linearly spaced between 0° and 180°. To mimic visual input consisting of gratings oriented at an angle θ_0 each excitatory synapse i with preferred orientation θ_i received as input a Poisson spike train with an average firing rate given by the von Mises distribution

Neuron model

Parameter	Value	Parameter	Value
C, membrane capacitance	281 pF	a, subthreshold adaptation	4 nS
g_L, leak conductance	35 nS	b, spike triggered adaptation	0.0805 nA
E_r, approximated resting potential	-70.6 mV	I_{sp}, spike current after a spike	400 pA
Δ_T, slope factor	2 mV	τ_z, spike current time constant	40 ms
V_T, threshold potential at rest	-50.4 mV	τ_{V_T}, threshold potential time constant	50 ms
V_{reset}, resetting voltage	-50.4 mV	$V_{T_{max}}$, threshold potential after a spike	30.4 mV
V_{peak}, spiking threshold	20 mV	k, argument of modified Bessel function for synaptic input	1.7
$\tau_{w_{ad}}$, adaptation time constant	144 ms	A, amplitude of the orientation-selective response of synapses	0.14
g_{ex}, excitatory synaptic conductance	35 nS	V_{ex}, reversal potential of the excitatory synapse	0 mV
g_{inh}, inhibitory synaptic conductance	40 nS	V_{inh}, reversal potential of the inhibitory synapse	-80 mV

Table 2.1. Parameters used in the model for the neuron. All parameters were set in advance on the basis of [**22**].

with center $2\theta_0$,

$$\nu_i = A\frac{e^{k\cos(2(\theta_i-\theta_0))}}{2\pi I_0(k)}. \tag{2.5}$$

Here the modified Bessel function of order 0, $I_0(k)$, provided the normalization and A controlled the overall amplitude of the input. The value of k was determined by matching the tuning width of ν_i to that observed for neurons in layer 4 [**30**, **31**]. All

excitatory and inhibitory synapses delivered conductance-based currents. The total synaptic current I_{syn} was given by

$$I_{syn} = \sum_{i=1}^{i=500} X_i \, w_i \, g_{ex} \, (V_{ex} - u) + g_{inh} \, (V_{inh} - u). \tag{2.6}$$

where g_{ex} (g_{inh}) was the excitatory (inhibitory) synaptic conductance, V_{ex} (V_{inh}) the reversal potential of the excitatory (inhibitory) synapses. The presynaptic Poisson spike trains were given by $X_i(t) = \sum_n \delta(t - t_i^{(n)})$ with i the index of the synapse and n counting the spikes in the train. The conductance g_{inh} of the inhibitory synapses was chosen to match the experimentally observed binocular sublinear integration ratio [**29**] (Fig.2.2A). Since the inhibitory synapses were not plastic, the timing of that input was not essential and we modeled it as a steady current rather than driven by spike trains. The difference in the strength of input from the ipsilateral eye and from the contralateral eye was not included in the model. Note that, effectively, the visual inputs in our model were all presented with the same spatial phase. Therefore, the difference in the phase dependence of the response of complex cells and simple cells in V1 was not considered in the model.

Besides the scenario with monocular input, we performed additional numerical simulations for scenarios with binocular inputs having various input characteristics. We used various distributions of the ODI and allowed various degrees of mismatch. Specifically, we investigated the following scenarios:

(1) the binocular inputs to each synapse are perfectly matched and the distribution of their ocular dominance is peaked at ODI=0.

(2) the binocular inputs to each synapse are unmatched with independent, uniformly distributed preferred orientations and the distribution of their ocular dominance is peaked at ODI=0.

(3) the binocular inputs to each synapse are perfectly matched and the distribution of their ocular dominance rises towards positive and negative ODI.

(4) the binocular inputs to each synapse are unmatched with independent, uniformly distributed preferred orientations and the distribution of their ocular dominance rises towards positive and negative ODI.

(5) same as (3) except the 40% of the inputs that had the most biased ODI in case 3 are made monocular.

(6) same as (4) except the 40% of the inputs that had the most biased ODI in case 4 are made monocular.

We present mostly results for cases 1,2. In case 1, the excitatory inputs were provided by 500 tuned synapses. For each of the 25 equally spaced preferred orientations there were 20 synapses, the ODI-values of which were spaced to obtain the distribution $f(x) = 0.75 - 0.75x^2$, $x \in [-1, 1]$. Thus, the ODI of cell j was given by $F^{-1}(\frac{j-1}{19})$, $j = 1, \ldots 20$, with $F(x)$ being the CDF of $f(x)$, $F(x) = 0.5 + 0.75x - 0.25x^3$. Case 3 was as case 1 except $f(x) = 0.125 + 1.125x^2$, $x \in [-1, 1]$. In case 2, the cell received 490 excitatory, tuned synaptic inputs. For each ODI-value there were 49 synapses with independently chosen preferred orientations. The ODI-values were chosen as in case 1. Case 4 is as case 2 except $f(x) = 0.125 + 1.125x^2$, $x \in [-1, 1]$. With binocular inputs, given a visual input oriented at θ_0, each excitatory synapse i with

preferred orientation θ_{il} through the left eye and θ_{ir} through the right eye received a Poisson spike train with an average firing rate given by the linear combination of the monocular firing rates (cf. (2.5)),

$$\nu_i = \frac{L}{L+R} A \frac{e^{k\cos(2(\theta_{il}-\theta_0))}}{2\pi I_0(k)} + \frac{R}{L+R} A \frac{e^{k\cos(2(\theta_{il}-\theta_0))}}{2\pi I_0(k)}. \tag{2.7}$$

where $\frac{R-L}{R+L} = \text{ODI}$. In case 1-6 we applied the same plasticity model and simulation protocol as in the monocular case.

2.2.3. Plasticity model

The excitatory synapses were chosen to be plastic while the strength of the inhibitory synapses was kept fixed. As plasticity model we chose the well-validated model of voltage-based STDP with homeostasis introduced in [**22**], which exhibited separate additive contributions to the plasticity rule for long-term depression (LTD) and for long-term potentiation (LTP),

$$\begin{aligned} \frac{d}{dt} w_i &= -A_{\text{LTD}}(\overline{\overline{u}})\, X_i\, [\overline{u}_- - \theta_-]_+ \\ &\quad + A_{\text{LTP}}\, \overline{x}_i\, [u - \theta_+]_+ [\overline{u}_+ - \theta_-]_+. \end{aligned}$$

The weights were limited by hard bounds, $w_{min} \leq w_i \leq w_{max}$. The LTP component depended on the postsynaptic membrane potential and a low-pass filtered version of the presynaptic spike train obtained via

$$\tau_x \frac{d}{dt} \overline{x}_i = -\overline{x}_i + X_i(t). \tag{2.8}$$

The low-pass filtered, postsynaptic membrane potentials $\bar{u}_{\pm}$ were obtained via

$$\tau_{\pm}\frac{d}{dt}\overline{u}_{\pm} = -\overline{u}_{\pm} + u(t) \tag{2.9}$$

and entered the plasticity rule through the rectifier denoted by $[\ldots]_+$. The amplitude $A_{\mathrm{LTD}}(\overline{\overline{u}}) = A^{(0)}_{\mathrm{LTD}}\frac{\overline{\overline{u}}^2}{u^2_{ref}}$ captured a homeostatic process based on the low-pass filtered square of the deviation of the membrane potential from the resting potential,

$$\tau_{th}\frac{d(\overline{\overline{u}}^2)}{dt} = -\overline{\overline{u}}^2 + \left(u(t) - E_r\right)^2 . \tag{2.10}$$

Thus, the key features of this plasticity model are that depression occurs when a presynaptic spike arrives and the average voltage $\overline{u}_-$ surpasses the threshold θ_-, while a synapse is potentiated if the momentary postsynaptic voltage $u(t)$ is above the threshold θ_+ and the average voltage $\overline{u}_+$ is above θ_- during a time of order τ_x after a presynaptic spike. Parameters for the plasticity model were kept fixed throughout all simulations (see Table 2.2).

2.2.4. Simulation

The initial strengths of the excitatory synapses were chosen randomly from a uniform distribution within $[w_{min}, w_{max}]$. For the first stage from $t = 0$ to $t = t_{\mathrm{switch}}$, we simulated monocular vision by presenting a random sequence of oriented visual inputs that were uncorrelated between the left and the right eye. The orientation of the visual input was randomly changed every 225 ms. This represented the monocular phase (MP) of the simulation (Fig.2.1B). Then, in the second, binocular phase

Plasticity model

Parameter	Value	Parameter	Value
θ_+, threshold potential for voltage	-45.3 mV	τ_-, time constant for filtered voltage $\overline{u}_-$	10 ms
θ_-, threshold potential for filtered voltage	-70.6 mV	τ_+, time constant for filtered voltage $\overline{u}_+$	7 ms
$A^{(0)}_{\mathrm{LTD}}$, amplitude of LTD	$7 \times 10^{-4}\mathrm{mV}^{-2}$	τ_x, time constant for the presynaptic spiking trace	15 ms
A_{LTP}, amplitude of LTP	$12 \times 10^{-4}\mathrm{mV}^{-2}$	τ_{th}, time constant for the homeostasis	1.2 s
w_{min}, lower bound for the synaptic weight	0	w_{max}, upper bound for the synaptic weight	1.6

Table 2.2. Parameters of the plasticity model. Parameters as used in [**22**] for visual cortex, except for $A^{(0)}_{\mathrm{LTD}}$, A_{LTP}, which have been increased to speed up the simulations.

(BP) from $t = t_{\mathrm{switch}}$ to $t = t_{\mathrm{final}}$, we simulated binocular vision by presenting a random sequence of oriented visual inputs that were identical for the two eyes. The orientation of the visual input was again changed randomly at the same frequency as in MP. Note that for cases 1, 3, 5, we did not include in our model an early phase during which the preferred orientations of upstream neurons become matched. We omitted the transition period (P15-P20) during which spontaneous activity and visually evoked activity are both driving plasticity [**25**]. To monitor the evolution of the preferred orientation we recorded all synaptic strengths every 250 ms. Monocular and binocular tuning curves were generated by testing the spiking response of the postsynaptic cell for the recorded synaptic strengths every 20s. To gather statistics, we ran the simulations multiple times ($n = 5600$ trials). Each trial produced an effectively different cell with different response properties.

To generate a well-controlled initial mismatch for the BP we shifted, right after MP, the synaptic strengths for inputs from one eye from 0° to 80° in steps of 10°.

All numerical simulations were performed with MATLAB. The code is available from the authors upon request.

2.2.5. Data analysis

We characterized the response of the postsynaptic neuron using the average spiking rate during windows with a duration of 1 second, both monocularly and binocularly. The tuning curve was generated by plotting the response magnitude against the orientation of the visual input. We defined the preferred orientation of the cell as the orientation that gave the largest response. This was done for monocular input yielding separate preferred orientations $O_{L,R}$ for the left and right eye, respectively, and for binocular input resulting in O_{bino}. The monocular/binocular spiking rate was defined as the response for the preferred orientations $O_{L,R}$ and O_{bino}, respectively. The mismatch ΔO in the preferred orientation was calculated as the smaller of the two values $|O_L - O_R|$ and $180° - |O_L - O_R|$. The global orientation selectivity index (gOSI) was computed as the magnitude of the sum $\frac{\sum R(\theta)e^{2\theta i}}{\sum R(\theta)}$ over all angles with $R(\theta)$ giving the firing rate response at orientation θ. The ocular dominance index (ODI) for each cell was calculated as $\frac{R-L}{R+L}$, where R and L represent the maximum response magnitude for input from the right and left eye, respectively. The ODI ranges from -1 and 1, where positive values indicate right bias and negative values indicate left bias. The prediction error for the matching outcome was the difference between

the predicted and the measured binocular preferred orientation. The decay rate of mismatch during binocular vision at time t (with mismatch $\Delta O(t)$) was determined by $-\frac{\Delta O(t+\Delta t)-\Delta O(t)}{\Delta O(t)\,\Delta t}$ with $\Delta t = 45$s. To reduce the impact of noise, we included in the computation of the matching rate only cells for which $\Delta O(t)$ was larger than 30°.

To analyze the evolution of the monocular tuning curves, we developed two quantifications, the bimodality index and the monocularity index. The bimodality index $\mathcal{B}$ quantified the maximal degree of bimodality of the monocular tuning curves throughout BP by measuring at each timepoint t during BP the response amplitude for the dominant and the subdominant preferred orientations. At each time t, for the left and right eye the dominant preferred orientation was defined as the orientation evoking the maximal response $R_l^{(dom)}(t)$ and $R_r^{(dom)}(t)$, respectively, after smoothing the tuning curves with a 4-mode Fourier filter (Fig.2.11A below). If the tuning curves exhibited an additional peak $R_{l,r}^{(sub)}(t)$, it defined the subdominant preferred orientation. If there was no such subdominant peak we set the corresponding amplitudes $R_{l,r}^{(sub)}(t)$ to 0. The bimodality index $\mathcal{B}$ was then computed as

$$\mathcal{B} = \max_{t \geq t_{switch}} \left(\max \left(\frac{\widetilde{R}_l^{(sub)}(t)}{\widetilde{R}_l^{(dom)}(t)}, \frac{\widetilde{R}_r^{(sub)}(t)}{\widetilde{R}_r^{(dom)}(t)} \right) \right),$$

where $\widetilde{R(t)}$ was obtained by smoothing the corresponding $R(t)$ in time using a piecewise cubic spline with 5 nodes to reduce noise. A bimodality index close to 1 characterized a cell whose tuning curve was quite bimodal at some time during the matching (Fig.2.11A and left panel in Fig.2.11B).

The monocularity index $\mathcal{M}$ measured the maximal degree of monocularity of the cell during BP. It was computed as

$$\mathcal{M} = 1 - \min_{t \geq t_{switch}} \left(\min \left(\frac{R_l^{(dom)}(t)}{R_l^{(dom)}(t_{switch})}, \frac{R_r^{(dom)}(t)}{R_r^{(dom)}(t_{switch})} \right) \right),$$

where the left and right monocular response amplitudes $R_{l,r}^{(dom)}(t_{switch})$ for the dominant preferred orientation at the onset of BP were used to scale the later response amplitudes. The closer this index is to 1, the more monocular the cell was at some time during BP (Fig.2.11B). We were particularly interested in how relatively strong monocular orientational receptive fields (ORF) matched. Here we loosely defined ORFs as those orientations to which the neuron responded significantly, i.e. the orientations for which the tuning curve is significantly above baseline. Focusing on relatively strong ORFs we calculated the bimodality and monocularity index only for cells that, at the onset of BP, had monocular gOSIs through each eye above 0.3, monocular maximal response above $0.8/s$, and mismatch larger than $20°$.

2.2.6. Robustness test

We tested the sensitivity of our results with respect to the five key parameters of the plasticity model (i.e., A_{LTP}, A_{LTD}, τ_x, τ_+, τ_-) by varying them by $\pm 20\%$. To do so the main results were condensed into correlations between different quantities characterizing the cells (Table 2.3). For instance, to test whether the matching rate decreased with increasing gOSI we measured the correlation between the matching rate and the gOSI across all cells and determined to what extent the correlation

changed when changing the parameters. To assess the significance of these changes we compared them with the 95% confidence interval of the correlation for the standard parameter set. Most correlations did not change significantly with these parameter changes. Even when the changes were quantitatively significant, the results still agreed qualitatively with those from the standard parameter set.

2.3. Results

The computational model consisted of one hypothetical binocular cell receiving excitatory, orientation-tuned inputs from each eye via plastic synapses [**22**] and inhibitory, untuned inputs from each eye via non-plastic synapses (Fig.2.1A). Through the inhibitory inputs the model captured the experimentally observed sublinear binocular integration [**29**] (Fig.2.2A). In analogy to the cortical balanced state [**21**], the firing of the cells was driven by fluctuations in the inputs rather than their mean value (Fig.2.2B) The computation involved a monocular (MP) and a binocular (BP) phase (Fig.2.1B). Since the stimulus sequence in both phases was random, repeated trials effectively generated an ensemble of cells with different response properties. The resulting distributions for the ocular dominance (ODI), the orientation selectivity (gOSI), and the remaining mismatch of the preferred orientations (ΔO) were consistent with the experimental data reported by [**31**] (Fig.2.3).

2.3.1. Synaptic plasticity captures binocular matching

The results obtained in our model are consistent with key aspects of previous experiments [**18**, **23**, **26**]. Using a tuning width for the inputs that corresponds to that

A Figure	**B** Quantity 1	**C** Quantity 2	**D** # of parameter sets outside the 95% confidence interval	**E** 95% confidence interval for the standard set
Fig.2.5A	Change δO_L in the left preferred orientation during BP	|ODI| at t_{switch}	0/10	(0.19,0.29)
Fig.2.5B	Change δO_R in the right preferred orientation during BP	|ODI| at t_{switch}	0/10	$(-0.29, -0.19)$
Fig.2.6A	Mean monocular gOSI at t_{switch}	Mismatch at t_{switch}	0/10	$(-0.05, 0.03)$
Fig.2.6B	Mean monocular gOSI ($t = 192.5s$)	Mismatch ($t = 192.5s$)	5/10	$(-0.29, -0.19)$
Fig.2.6D	Matching rate	Mean monocular gOSI	0/10	$(-0.24, -0.08)$
Fig.2.6F	Growth rate of gOSI	Mismatch	1/10	$(-0.41, -0.31)$
Fig.2.8B	Accuracy of predicting matching outcome with O_{bino} at $t = 191.25$s	Mismatch at $t = 191.25$s	0/10	$(-0.45, -0.34)$
Fig.2.8C	Accuracy of predicting matching outcome with O_{bino} at t_{switch}	Mismatch at t_{switch}	0/10	$(-0.24, -0.15)$
Fig.2.10B	Matching rate	|ODI|	0/10	$(0.02, 0.13)$
Fig.2.8B	Monocularity index $\mathcal{M}$	Mismatch at t_{switch}	3/10	$(0.29, 0.45)$
Fig.2.8A	Bimodality index $\mathcal{B}$	Mismatch at t_{switch}	1/10	$(0.30, 0.41)$
Fig.2.8C	Bimodality index $\mathcal{B}$	Monocularity index $\mathcal{M}$	2/10	$(0.39, 0.53)$

Table 2.3. Robustness test. For each figure listed (column labeled A), the correlation between 2 quantities characterizing the cell (columns B,C) was computed with a 95% confidence interval for the standard parameter set (column E) and the number of parameter sets was determined for which the correlation is outside that confidence interval (column D).

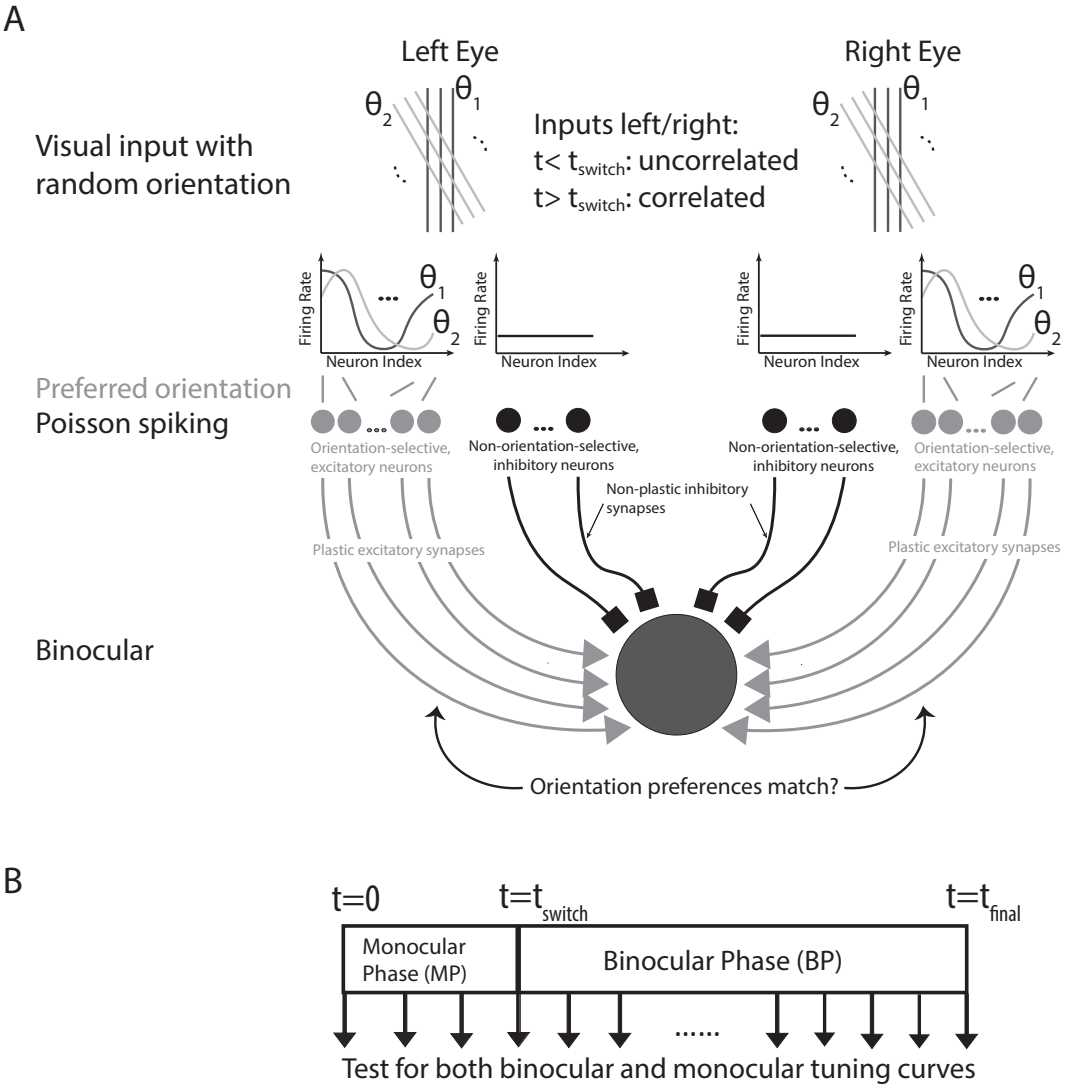

Figure 2.1. Computational Model. (A) The postsynaptic neuron received synaptic inputs as Poisson spike trains from excitatory, orientation-selective synapses and conductance-based current inputs from non-selective inhibitory synapses, divided equally into inputs from the left and the right eye. Random sequences of oriented visual input characterized by orientation θ were presented to each eye. Only excitatory synapses were plastic. (B) Simulation protocol: The orientation of the simulated visual input was randomly shifted every 225 ms. The left and right inputs were uncorrelated until $t_{\text{switch}} = 56.25s$ (monocular phase), then left and right inputs were identical (binocular phase).

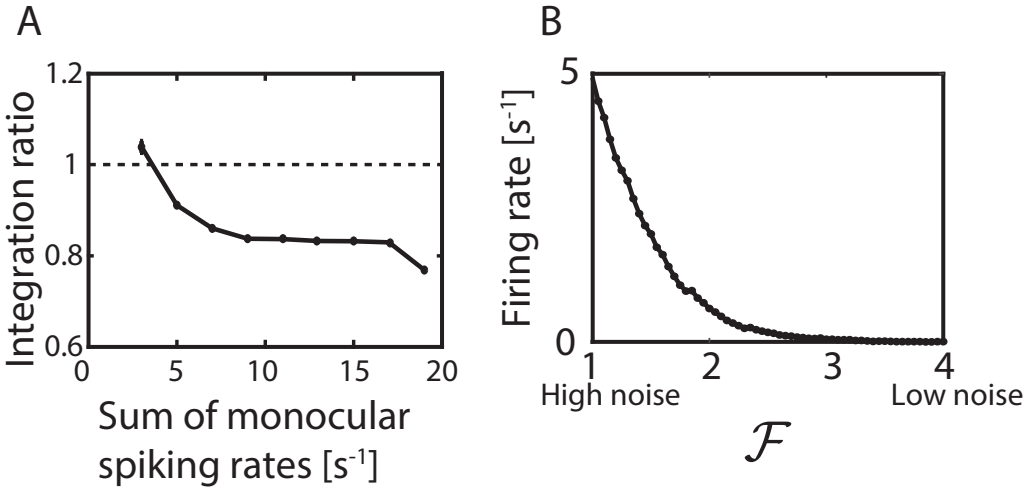

Figure 2.2. Sublinear integration ratio in the fluctuations-driven spiking network. (A) Sublinear integration ratio of the spiking rate. The ratio of the firing rate for binocular input during the binocular phase and the sum of the corresponding monocular rates is plotted against the sum of the monocular spiking rates. (B) Fluctuations drive the spiking. The firing rate of the cell goes to 0 when the fluctuations in the excitatory inputs are reduced by increasing the rates of the Poisson trains by a factor $\mathcal{F}$, while keeping the mean current fixed.

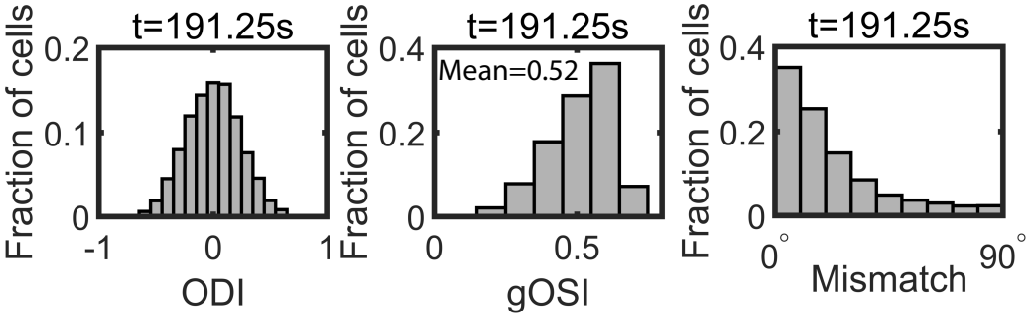

Figure 2.3. Distribution of the properties of the cells at the end of the binocular phase (BP). a) ODI, b) gOSI, c) mismatch ΔO.

of cells in layer 4 [**30**], our model reproduced the development of orientation selectivity for V1 cells with global orientation selectivity index (gOSI) and tuning width

similar to those found experimentally in layer 2/3 [**30**, **31**]. Also, the experimentally observed sublinear binocular integration [**29**] was captured in our model (Fig.2.2A).

Moreover, while right after eye-opening a fraction of V1 cells has been observed to have well-developed orientation selectivity, their monocular preferred orientations for input from the left and the right were poorly matched [**23**]. In fact, in some cells, they were nearly 90° apart, the maximal possible difference. This mismatch decreased substantially with age to reach the adult level by P30-P36 [**18**, **23**].

In our model, during the initial phase of MP multiple sets of synapses were potentiated. Due to the random distribution of the initial synaptic strengths, the randomly chosen orientations, as well as the variability of the number of spikes in the input Poisson spike trains the synaptic strengths did not vary smoothly with orientation. Nevertheless, the sets of potentiated synapses roughly specified monocular orientational receptive fields (ORFs) of the postsynaptic neuron, defined as those orientations for which the tuning curve is significantly above baseline. During MP these ORFs for input from the left and the right eye did not match (Fig.2.4A, 1 and 2 up to $t = t_{\text{switch}}$, marked by white dashed lines), which manifested itself also in non-matching orientation tuning curves (Fig.2.4B, 1 and 2).´

During BP both eyes received the same inputs. This allowed the potentiation of weak synapses that by themselves were not strong enough to drive a post-synaptic spike, if the synapses with the same preferred orientation but receiving input from the other eye were sufficiently strong to trigger a spike. This slowly modified the ORFs and the tuning curves (Fig.2.4A,B for $t > t_{switch}$), decreasing the mismatch

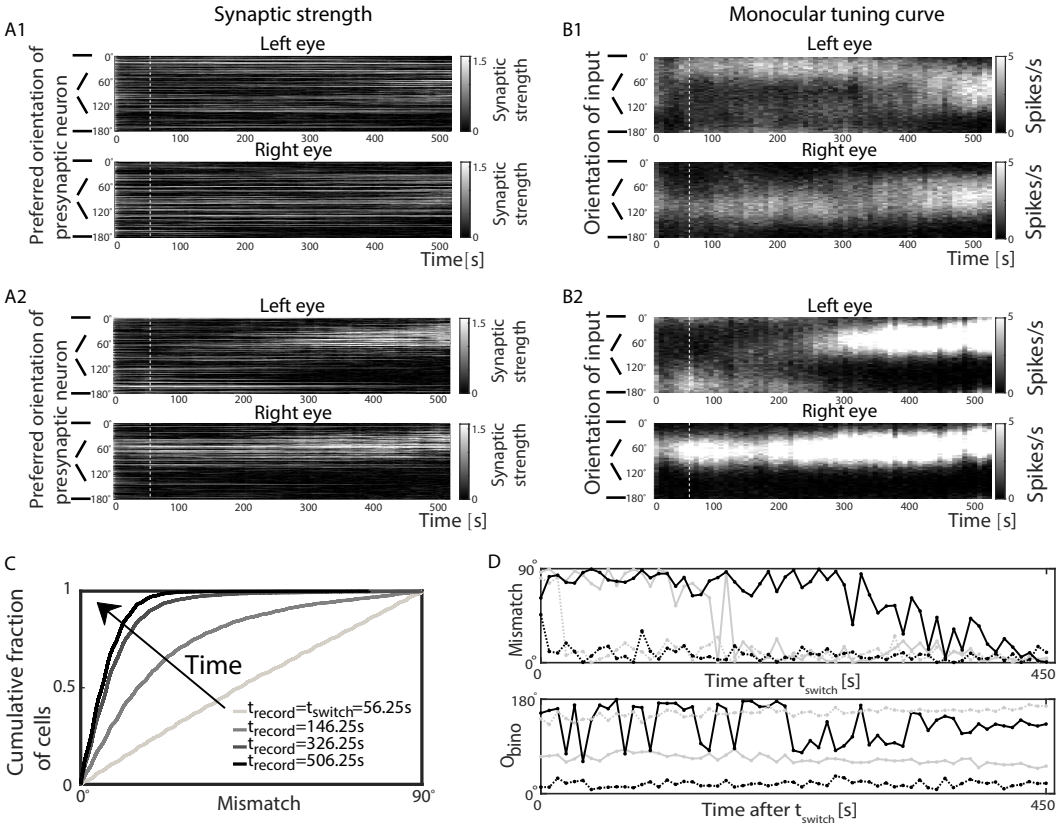

Figure 2.4. Binocular vision reduces the mismatch of the monocular preferred orientations. (A1,A2): Two examples of the temporal evolution of the synaptic strengths. The presynaptic neurons are ordered according to their preferred orientation (vertical axis), and their synaptic strengths are illustrated in greyscale as a function of time (horizontal axis). (B1,B2): Corresponding evolution of the monocular tuning curves through each eye. Greyscale indicates the firing rate of the cell in response to monocular input with an orientation as indicated along the vertical axis. In (A1,B1) the two monocular preferred orientations drifted toward each other while in (A2,B2) one monocular preferred orientation switched to the other discontinuously to achieve binocular matching. White dashed lines mark $t = t_{\text{switch}}$. (C): The cumulative distribution function of the mismatch at different times ($t_{\text{switch}} = 56.25$s; $n = 5600$ cells). (D) The evolution of the mismatch and the binocular preferred orientation O_{bino} for 4 cells during BP, showing representative trajectories. The solid black line represents the cell shown in (A1,B1). The solid grey line represents the cell shown in (A2,B2).

between the two monocular preferred orientations. Eventually, in almost all cells the preferences became matched within 20° (Fig.2.4C). The variability in the evolution of the cell properties was extremely high: cells could match early (dashed lines in Fig.2.4D) or late (solid lines), their preferred orientation could shift gradually (black lines) or it could switch suddenly (grey lines).

2.3.2. The effect of ODI on the matching outcome

It has been shown that three weeks of environmental enrichment (EE) can rescue the disrupted binocular mismatch caused by visual deprivation during the critical period [**26**]. These experiments revealed that ocular dominance plays a key role in the binocular matching process. In cells whose response was dominated by one of the two eyes, binocular matching was achieved by the orientation preference for input from the nondominant eye changing, while the orientation preference for input from the dominant eye did not change much.

Motivated by this experimental result, we determined for each cell the change $\delta O_{L,R}$ in the left and right monocular preferred orientations during BP as well as the ocular dominance index (ODI) right before BP. The statistics of $\delta O_{L,R}$ and ODI across many cells are shown in histograms of $\delta O_{L,R}$ for each value of the ODI (Fig.2.5A,B). As in the experiments, the range in the change of preferred orientation for input from the nondominant eye was much wider than that for the dominant eye. This asymmetry becomes very clear when considering - for each value of the ODI - the range in $\delta O_{L,R}$ that includes 90% of the cells; its upper limit is shown as solid

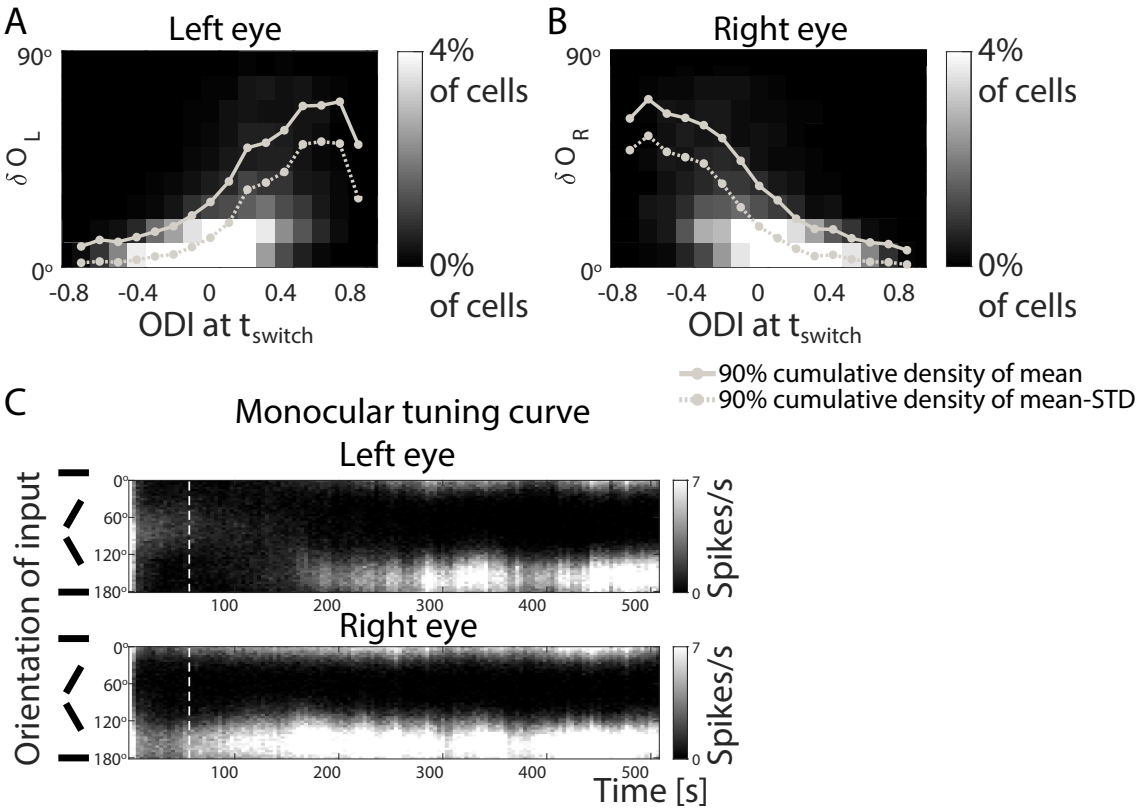

Figure 2.5. Preferred orientation mostly changes for nondominant eye. (A) Two-dimensional histogram in which the greyscale of each square bin indicates the percentage of cells whose monocular preferred orientation through the left eye changed by δO_L (vertical axis) during BP and that had an ODI at t_{switch} as given on the horizontal axis. (B) Same plot as (A), except for the right eye. In both (A) and (B) $t_{\text{switch}} = 56.25$s, $t_{\text{final}} = 506.25$s, $n = 5600$ cells. (C) The evolution of the monocular tuning curve for input from the left and right eye (cf. Fig.2.4B). White dashed lines mark $t = t_{\text{switch}}$. The scale of the greyscale map is capped to better show the difference between the left and right monocular firing rates at t_{switch} (ODI>0).

lines in Fig.2.5A,B. Since the preferred orientation is measured using Poisson spike trains it exhibits fluctuations. To illustrate that they do not reduce the asymmetry impact we also considered the cumulative distribution across cells of the mean of $\delta O_{L,R}$ minus the standard deviation of $\delta O_{L,R}$. Its 90%-point is given by the dashed

lines. Fig.2.5C shows an illustrative example in which at t_{switch} (white dashed line) the cell was dominated by the input from the right eye (ODI= 0.415). During BP the preferred orientation for input from the nondominant (left) eye changed substantially, while that for input from the dominant (right) eye did not evolve much.

2.3.3. The interaction between orientation selectivity and matching

Previous experimental results revealed an inverse relationship between mismatch and gOSI: cells with smaller orientation mismatch had greater orientation selectivity. This did not hold in mice whose binocular matching process was compromised by visual deprivation; their ΔO values spanned the entire $0° - 90°$ range for all gOSI values [**26**]. The histograms in Fig.2.6 show the relationship between mismatch and gOSI obtained in the model at the onset of BP at t_{switch} (Fig.2.6A) and at an intermediate time during BP (Fig.2.6B). Most cells were neither well-matched nor very selective at the end of MP (Fig.2.6A). Consistent with the experimental results, at intermediate times during BP the mismatch was small in highly orientation-selective cells (Fig.2.6B).

To gain insight into the relationship between the matching process and the sharpening of the orientation selectivity, we measured the evolution of the gOSI and the mismatch for different durations of the MP (Fig.2.6C and E). For $t_{switch} > 1250$s the gOSI reached a steady state during MP (Fig.2.6C). Remarkably, its saturation value was significantly lower than the value reached during BP, even if that BP followed an MP with short duration. This indicates that binocular vision enhanced

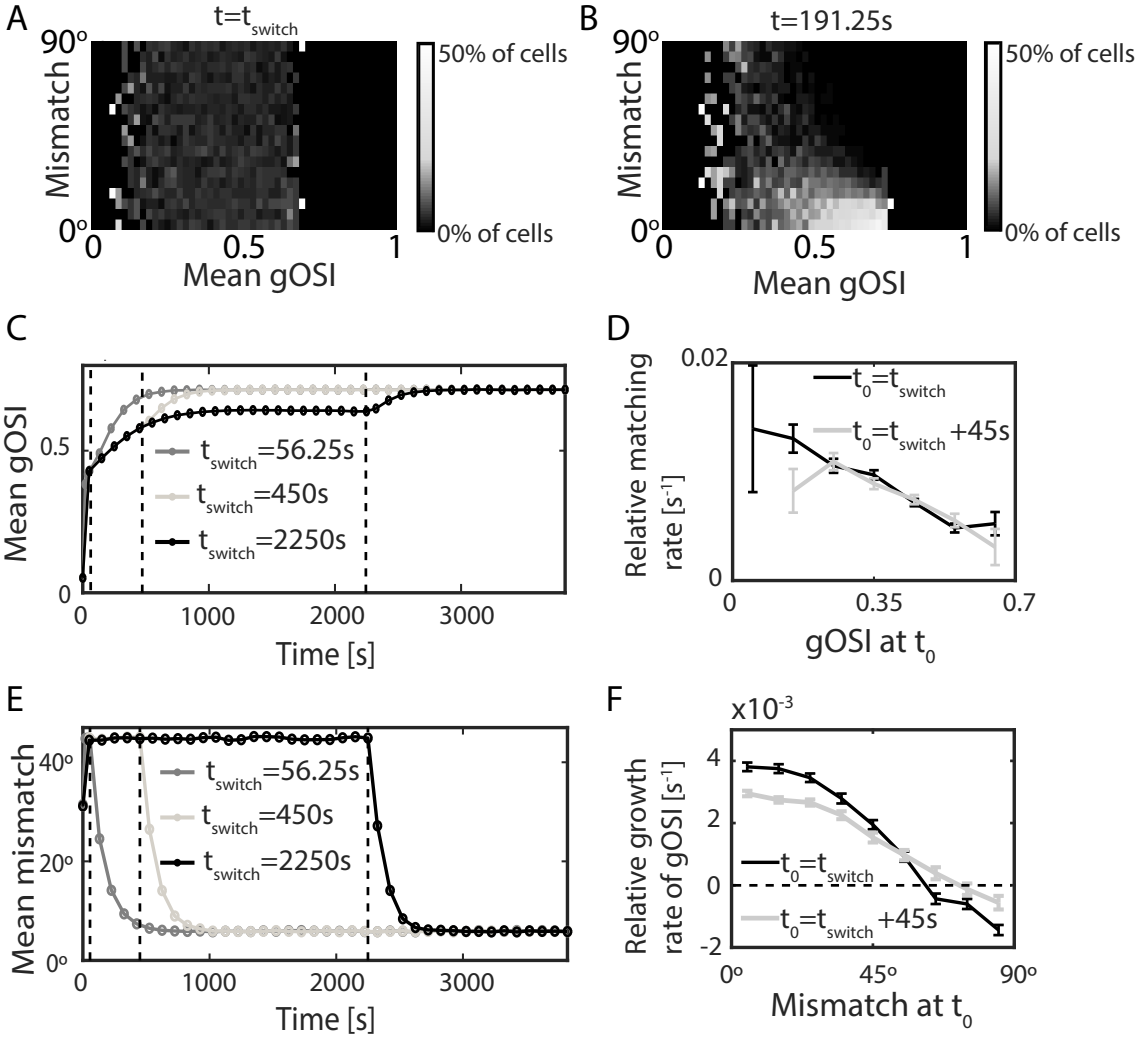

Figure 2.6. Matching leads the development of orientation selectivity during BP. (A,B): Histogram of the mismatch for different values of the mean monocular gOSI at $t = t_{\text{switch}} = 56.25$s. The histogram is normalized for each value of the mean monocular gOSI. (B) As (A), but for $t = 191.25$s during BP. Lower mismatch is correlated with higher orientation selectivity ($n = 5600$ cells). (C) Binocular vision enhances orientation selectivity. The evolution of gOSI for $t_{switch} = 56.25$s, 450s, 2250s (marked by dashed lines). ($n = 5000$ cells). (D) Less selective cells match faster. The relative matching rate is given by $-\frac{\Delta O(t_0+\Delta t)-\Delta O(t_0)}{\Delta O(t_0)\,\Delta t}$, where $t_0 = t_{switch}$ (black line), $t_{switch} + 45$s (grey line) with $\Delta t = 45$s. (E) Binocular vision matches monocular preferred orientations. The evolution of mismatch for $t_{switch} = 56.25$s, 450s, 2250s (marked by dashed lines). ($n = 5000$ cells, $t_{final} = t_{switch} + 562.5s$). (F) The growth rate of the gOSI decreased with increasing mismatch. The relative growth rate of the gOSI is given by $\frac{\Delta gOSI(t_0+\Delta t)-\Delta gOSI(t_0)}{\Delta gOSI(t_0)\,\Delta t}$, where $t_0 = t_{switch}$ (black line), $t_{switch} + 45$s (grey line) with $\Delta t = 45$s. In panel D and F the error bars denote the SEM.

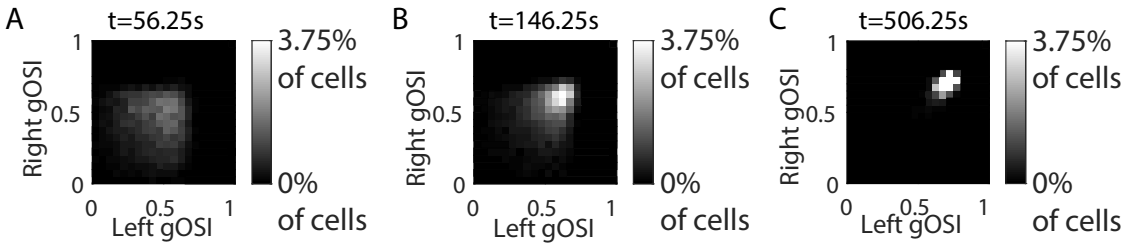

Figure 2.7. Binocular vision enhances and matches monocular orientation selectivity. Two-dimensional histograms of right and left gOSI at the onset (A, $t_{switch} = 56.25$s) and two intermediate times during BP (B, C). ($n = 5600$ cells)

the development of orientation selectivity. Further analysis showed that the mismatch decayed exponentially to its final value faster than the gOSI. By employing initial conditions with well-controlled mismatch (see Methods), we showed that less selective cells matched faster (Fig.2.6D) and the growth rate of the gOSI decreased with increasing mismatch (Fig.2.6F). Strikingly, for cells with large mismatch the growth rate could even be negative and the cells became less selective. With time, however, the mismatch of these cells decreased as it did for the other cells and eventually reached values for which the gOSI increased. This suggests that the matching process enhanced the orientation selectivity, while orientation selectivity was not a driving force of binocular matching but had, instead, a negative effect on matching speed.

Moreover, at the onset of BP the left and right orientation selectivities were often quite different from each other leading to a broad distribution across cells (Fig.2.7A). But binocular vision enhanced the selectivities and drove them to the same large value (Fig.2.7B and C).

2.3.4. Prediction of matching outcome

Next, we put forward testable predictions based on our model. We hypothesized that the binocular preferred orientation right before BP could predict the eventual matching outcome. We therefore defined the prediction error as the difference between the final binocular preferred orientation and that at the beginning of BP (Fig.2.8A). Overall, the binocular preferred orientation at t_{switch} was a quite good predictor for the preferred orientation at all time points during BP that we investigated (Fig.2.8B). Note that in Fig.2.8B the histogram of the prediction error was normalized separately for each value of the mismatch. This revealed that for small mismatch almost all cells had a prediction error of less than 20°, while for large mismatch the distribution of prediction errors was almost uniform. Thus, the mismatch that remained at a given time during BP indicated quite well whether the binocular preferred orientation at t_{switch} was a good predictor for the binocular preferred orientation at that later time.

Can the reliability of the prediction for the preferred orientation already be anticipated at t_{switch}? Indeed, already the *initial* mismatch was a good indicator for this reliability (Fig.2.8C): the prediction was quite accurate when the initial mismatch was small, while it became less reliable for large initial mismatch.

Since in the experiments the monocular, rather than the binocular tuning curves were measured [**26**], we tested how well the superposition of two monocular tuning curves at the onset of BP could predict the final, matched orientation. We found that at each time point the preferred orientation determined by the linear superposition of

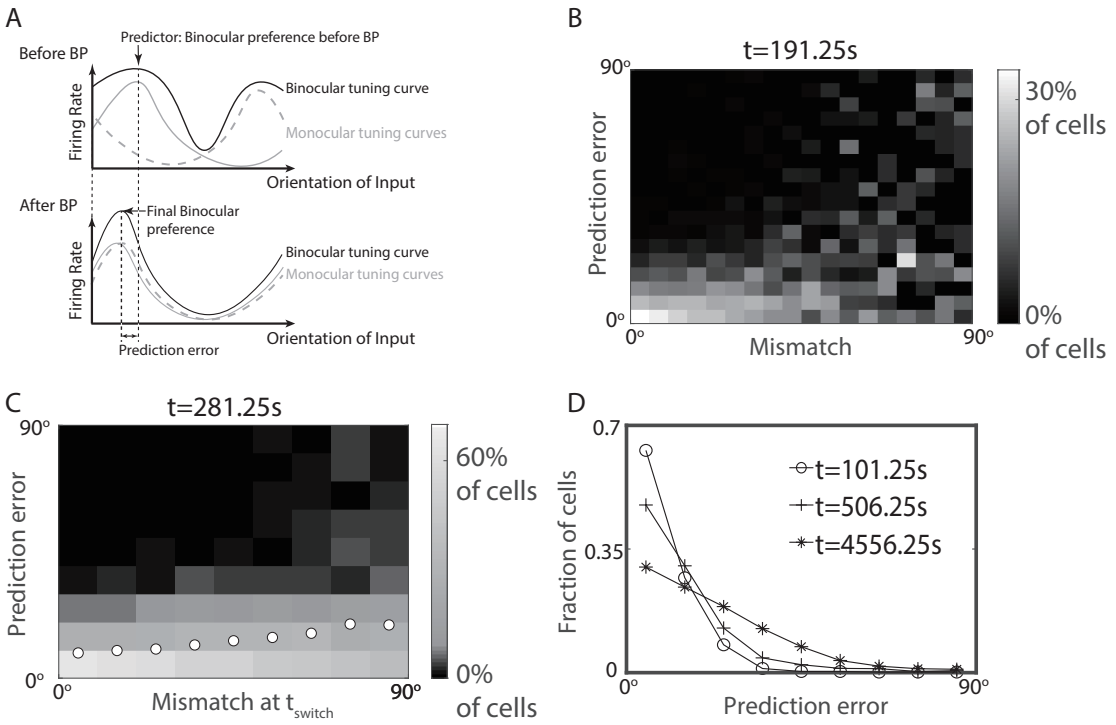

Figure 2.8. Binocular preferred orientation at the onset of BP predicts the preference after matching. (A): The prediction error was calculated as the difference between the binocular preferred orientation before and after BP. (B): The quality of the prediction decreased with increasing mismatch. Histogram of the prediction error for different values of the mismatch, both at the same time $t = 191.25$s. The histogram is normalized separately for each value of the mismatch. (C): The accuracy of prediction decreased with the *initial* mismatch. Like (B), but at $t = 281.25$s and using the *initial* mismatch. Circles represent the mean prediction error of the trials for each value of initial mismatch. (D): The mean prediction error increased with time. The distribution of the prediction error from well-matched cells (mismatch $< 20°$) at three intermediate times during BP. In all figures, $t_{\text{switch}} = 56.25$s and $n = 5600$ cells.

two monocular curves was close to the binocular preferred orientation and therefore it was also a good predictor for the matching outcome (Fig.2.9).

The matched preferred orientation that emerges in a given cell reflects the initial synaptic weights as well as the sequence of presented visual inputs. Since in our simulations the synapses were plastic throughout the simulation and the sequence of inputs was random, the binocular preferred orientation evolved on a slow timescale, wandering around in a diffusive manner. The distribution of the prediction error across cells therefore broadened with time as shown in Fig.2.8D for well-matched cells (mismatch less than 20°), implying a growing mean prediction error.

2.3.5. The speed of matching depends on the initial ODI

We next examined how initial ocular dominance affected the speed of the matching process. Figs.2.10A, 1, 2 and 3 show the histogram of the mismatch for various time points as a function of the magnitude |ODI| of the ocular dominance index at t_{switch}. For high initial |ODI| the mismatch decreased rapidly, while in many cells that had a lower initial |ODI| the matching proceeded more slowly (most clearly seen comparing $t = 146.25$s with $t = t_{switch}$). We quantified this in terms of the decay rate of the mismatch at time t given by $-\frac{\Delta O(t+\Delta t)-\Delta O(t)}{\Delta O(t)\Delta t}$ with $\Delta t = 45$s. Fig.2.10B shows the mean of the decay rates across cells for different ranges of the |ODI| at $t_0 = t_{switch}$ and $t_0 = t_{switch} + 45s$. This result is consistent with the intuition that cells with a low initial |ODI| have two monocular ORFs with similar overall synaptic strengths, which compete with each other during BP, slowing down the matching process. This effect of ocular dominance on the binocular matching rate reveals ocular dominance as a driver of the binocular matching process. Note that cells with an initial mismatch

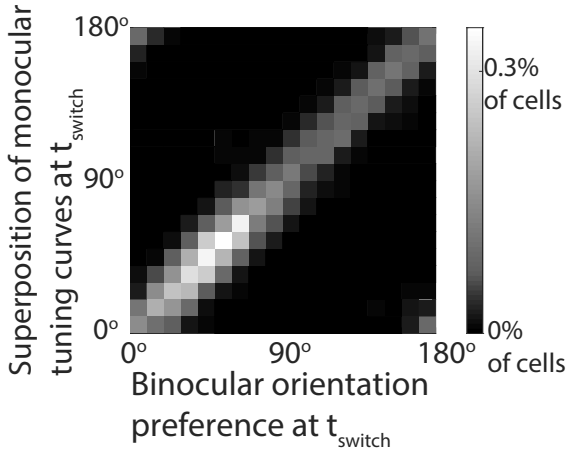

Figure 2.9. Binocular tuning is well approximated by the sum of the monocular tuning curves. Histogram of the binocular preferred orientation and the preferred orientation obtained from the sum of the two monocular tuning curves.

less than 40° were not included in Fig.2.10B, since here we were only interested in the matching processes starting with a state that was not well-matched. Similar values for the decay rates as shown in Fig.2.10B were obtained at other intermediate times during BP, suggesting an exponential decay of mismatch during BP.

2.3.6. The type of matching process depends on the initial mismatch

Finally, we investigated whether there are qualitatively different processes through which the binocular matching was obtained. There were at least two such processes: the two monocular preferred orientations could shift gradually towards each other (Fig.2.4B1), or one of the preferred orientations could switch to the other one discontinuously (Fig.2.4B2). The latter case was characterized by a period during which the tuning curve for one eye was bimodal, with the dominance switching from one peak to the other, leading to a discontinuity in the preferred orientation. During

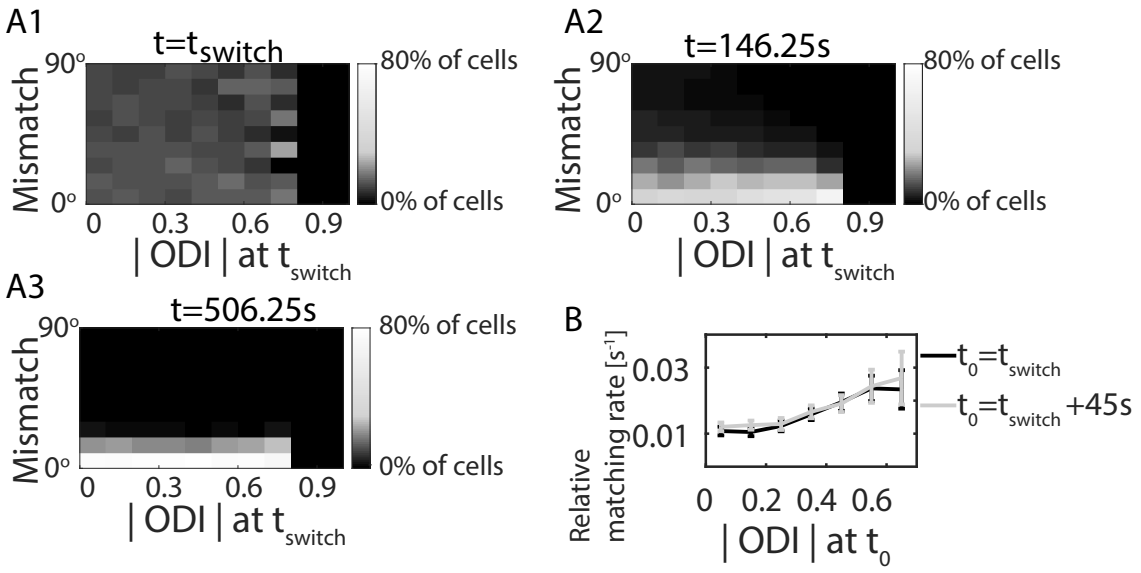

Figure 2.10. Binocular matching speed increases with the absolute value of initial ODI. (A1,2,3): Histograms of mismatch at different times for different values of the magnitude of ODI at t_{switch} ($t_{\text{switch}} = 56.25$s, $n = 5600$ cells). The histograms are normalized for each value of initial |ODI| separately. (B): The average relative matching rate during the time interval $[56.25\text{s}, 146.25\text{s}]$ against the ODI at $t_{\text{switch}} = 56.25$s and $t_{switch} + 45$s (3537 out of 5600 cells, the errobar gives SEM).

this time the cell responded only weakly to input from that eye; the cell was effectively monocular. This loss of binocularity could become permanent if it occurred towards the end of the binocular phase, which was referred to the critical period for ocular dominance plasticity. Similar result has been experimentally observed in later work [**32**]. In contrast, when the matching was achieved by shifting, the tuning curves of both eyes had only a single peak, which gradually shifted, and the cell remained binocular throughout BP (Fig.2.4B1).

Based on these observations we introduced a bimodality index $\mathcal{B}$ and a monocularity index $\mathcal{M}$ to characterize the matching process (see Methods and Fig.2.11A,B)

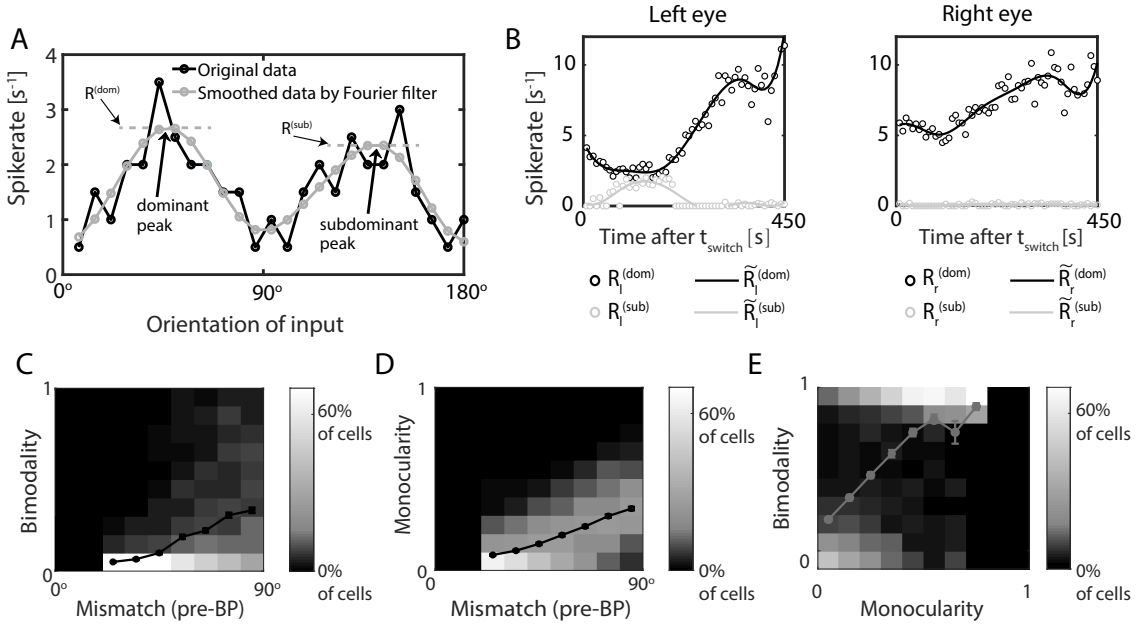

Figure 2.11. The type of matching depends on the initial mismatch. The bimodality index $\mathcal{B}$ and the monocularity index $\mathcal{M}$. (A) Identifying dominant and subdominant preferred orientations in each eye at time t. Black: noisy monocular tuning curve. Grey: smoothed data using a 4-mode Fourier filter (data from Fig.2.4B). (B) Temporal evolution of the dominant and the subdominant monocular response amplitudes $R_{l,r}^{(dom,sub)}$ of each eye. Circles: $R_{l,r}^{(dom,sub)}$, lines: data smoothed by a piecewise cubic spline with 5 nodes. The cell is bimodal through the left eye near time $t = 150$s and monocular through the right eye. (C) Histogram of the bimodality index $\mathcal{B}$ for different values of the mismatch at the onset of BP. (D) Histogram of the monocularity index $\mathcal{M}$ for different values of the mismatch at the onset of BP. (E) Combined histogram of the bimodality index $\mathcal{B}$ and the monocularity index $\mathcal{M}$. The lines in (C,D,E) denote the mean of the bimodality index $\mathcal{B}$ for different values of the mismatch (C) and the monocularity (E) and the mean of the monocularity index $\mathcal{M}$ for different values of the mismatch (D). Error bars denote the SEM, some of which were smaller than the symbol size.

and related it to the mismatch at t_{switch} (Fig.2.11C,D). For small initial mismatch, the cells showed little monocularity or bimodality throughout the matching process, implying that binocular matching was achieved by the monocular preferred

orientations shifting towards each other. If the initial mismatch was large, however, bimodality and monocularity were both larger and it was more likely that one of the two preferred orientations switched to the other. Thus, both, bimodality and monocularity, were equally suited to characterize the matching process; in fact, they were positively correlated (Fig.2.11E).

2.3.7. The dependence of matching on the input characteristics

So far we assumed for simplicity that all excitatory input synapses are monocular. However, cells in V1 vary substantially in their ocular dominance. To go beyond this simplification we therefore performed extensive additional numerical simulations to determine how the learning process and outcome depends on the input characteristics. We included inputs that were more realistic for the visual system, but covered also other situations that might be relevant for matching processes in multi-modal sensory processing. Specifically, we made the inputs binocular using various distribution of the ODI and allowed various degrees of mismatch. Here we illustrate the results for the following scenarios:

(1) the binocular inputs to each synapse are perfectly matched and the distribution of their ocular dominance is peaked at ODI=0.

(2) the binocular inputs to each synapse are unmatched with independent, uniformly distributed preferred orientations and the distribution of their ocular dominance is peaked at ODI=0.

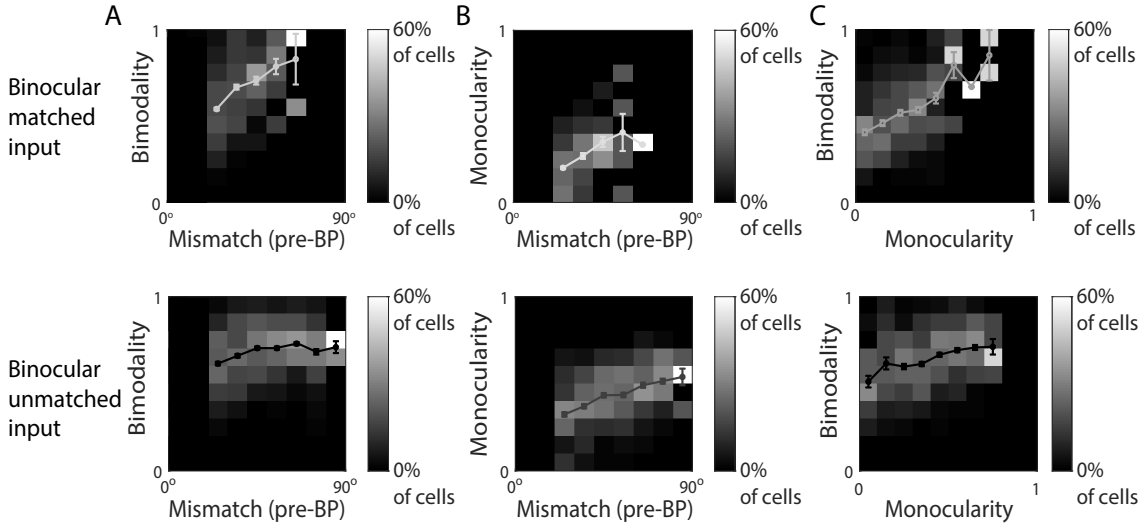

Figure 2.12. Shifting and switching depend on mismatch also for binocular inputs. Top row: binocular, perfectly matched inputs. Lower row: binocular, unmatched inputs. (A) Histogram of the bimodality index $\mathcal{B}$ for different values of the mismatch at the onset of BP. (C) Histogram of the monocularity index $\mathcal{M}$ for different values of the mismatch at the onset of BP. (C) Combined histogram of the bimodality index $\mathcal{B}$ and the monocularity index $\mathcal{M}$. The lines indicate the respective means with error bars denoting the SEM (the single point without errorbar in the top panel of (B,C) for the initial mismatch belonging to $(60°, 70°]$ represents a single cell).

Complex cells in the visual system are presumably best described by inputs in between these two cases, since under natural conditions simple cells match before complex cells [**18**] and exhibit a peaked ODI-distribution [**19**, **33**]. Thus, complex cells receive quite well, but not perfectly, matched inputs.

We found that in all cases with binocular and potentially unmatched inputs, key features of the matching process were qualitatively the same. In particular, matching predominantly occurred via shifting of the preferred orientations if the mismatch was small, while switching of the orientations occurred mostly for large mismatch (Fig.2.12).

The only significant differences arose for matched binocular inputs. While for unmatched binocular inputs the matching rate decreased with increasing gOSI, as was the case for the monocular inputs, this was not the case for matched binocular inputs (Fig.2.13A). In the latter case the mismatch of the cell response arises because different synapses provide inputs with different preferred orientations and different ODI. Thus, even though the left and right preferred orientations of a given synapse are the same, the strengths of the inputs from the left and right eye are not balanced. As a result, the orientation that dominates the overall input is in general not the same for the two eyes. For the mismatch of the cell to decrease it is then sufficient if its orientation selectivity increases, because this implies that the range of orientations that contribute to its input is reduced. This increase in the selectivity and the associated matching occurs already during the monocular phase. The difference in the matching mechanism also led to a difference in the dependence of the matching rate on the ODI (Fig.2.13B) and the dependence of the growth rate of the gOSI on the mismatch (Fig.2.13C). Performing additional simulations (see scenarios 3-6 listed in Methods), we found that this mechanism was less relevant when the inputs to each synapse were less matched or less binocular (i.e., more of the inputs to the cells had ODIs closer to 1 or -1).

2.4. Discussion

The role of plasticity in the development of the brain has been investigated extensively, with the visual system, particularly V1, serving as a prime example. Many

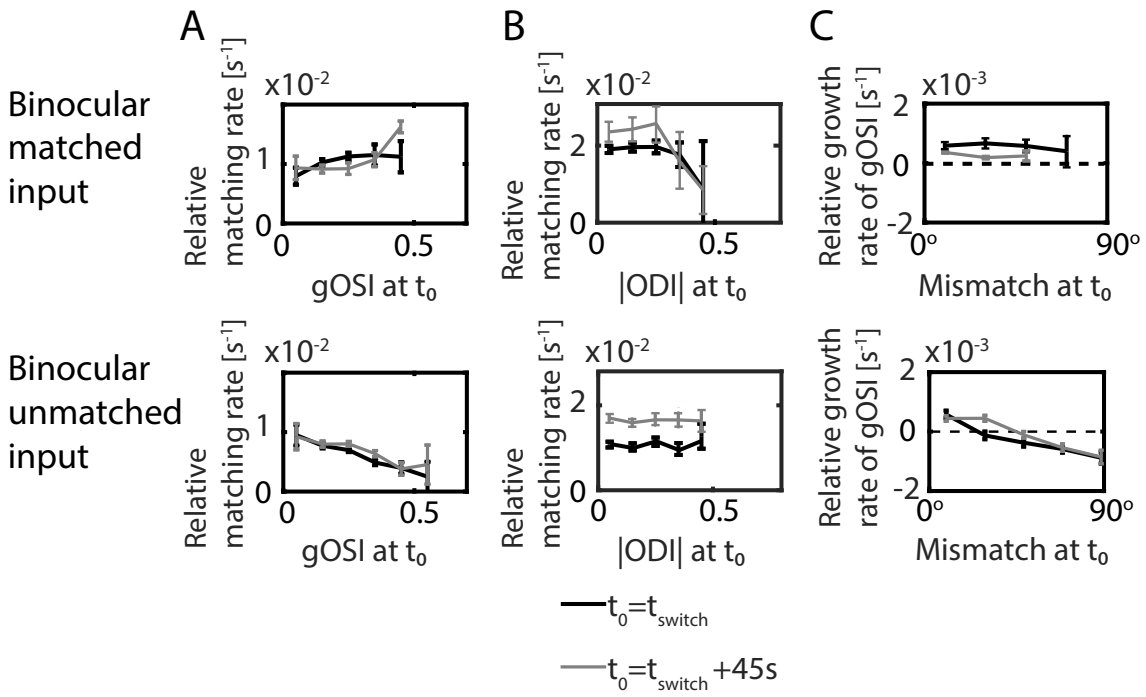

Figure 2.13. The interaction between ODI, gOSI and mismatch with binocular inputs. Top row: binocular matched inputs. Lower row: binocular, unmatched inputs. (A) The dependence of the matching rate on the gOSI. (B) The dependence of the matching rate on the |ODI|. (C) The dependence of the growth rate of the gOSI on the mismatch. error bars give the SEM. Results are shown for $t_0 = t_{switch}$ and for $t_0 = t_{switch} + 45s$. (See Fig.2.6D,F, Fig.2.10B). With binocular, unmatched inputs the behavior is as for monocular inputs. For binocular, matched inputs qualitative differences arise, particularly for the dependence of the matching rate on the gOSI (cf. Fig.2.6E,F).

of these studies were motivated by findings in cats, ferrets, and monkeys, where cellular response properties like ocular dominance and preferred orientation vary quite smoothly with position in visual cortex, leading to ocular dominance columns and orientation maps. The formation of these maps and columns has been described using Hebbian, correlation-based models [**20**, **34**–**36**]. From the perspective of multisensory integration the matching of the two monocular preferred orientations is of

particular interest. As shown by [**36**], this matching requires that the strengths of the two input-correlation modes are not too similar. The temporal evolution towards the matched configuration and the relation of this evolution to that of the orientation selectivity and ocular dominance has, however, not been addressed in [**36**]. Modeling synaptic plasticity using the BCM-model [**37**], the combined evolution of preferred orientation and ocular dominance has been investigated with focus on the impact of monocular and binocular deprivation [**38**]. To model strabism, this study also considered the case of uncorrelated inputs to the left and right eye. In that case all cells eventually became purely monocular in their model.

Our study has been motivated by recent experiments in mice [**18**, **23**, **26**], which focused on the process by which the two monocular preferred orientations become matched. We aimed to investigate to what extent these experimental findings can be captured in a relatively simple computational model. We therefore considered a single spiking neuron that receives orientation-selective inputs via plastic synapses.

For the plasticity mechanism we chose a well-accepted, biophysically somewhat detailed model [**22**] , which has been validated under quite a few, varied plasticity protocols, including in visual cortex. It reduces to the BCM-model [**37**], if the pre- and postsynaptic spike trains are uncorrelated and if their evolution is captured adequately within a firing-rate model. Since cortical cells in the balanced state respond to fluctuations in the input rather than its mean [**21**], it is not clear, however, whether the correlations are sufficiently negligible. Moreover, the stimuli used in

the experiments varied on a timescale that is not much longer than the interspike intervals [**30**]. We therefore did not perform that reduction.

For simplicity, we assumed that the synaptic plasticity mechanism does not change with eye-opening and the subsequent onset of the critical period for ocular dominance; only the inputs to the cortical neuron, which drive the synaptic plasticity, were taken to change from being uncorrelated between the two eyes before eye-opening to being correlated after eye-opening. This simplification is consistent with a number of experimental findings. In cats, orientation selectivity emerges already before eye-opening, driven by vision-independent spontaneous activity in the retina [**39**], and continues to increase after eye-opening. Until the onset of the critical period this increase does not depend on visual input [**40**]. Correspondingly, the onset of the critical period has been identified not as a change in the plasticity mechanism but as a transition from synaptic plasticity being driven predominantly by spontaneous activity to being driven mostly by visually evoked input [**25**]. This change results from an increase in inhibition, which reduces the weaker, spontaneous activity - but not the stronger, visually evoked activities - to magnitudes that are not sufficient to drive synaptic plasticity. Note that this scenario may vary across species [**39**, **41**].

We focused on complex cells, which receive orientation-selective inputs from simple cells, a situation that is analogous to that in multi-source systems in which

upstream neurons gain selectivity before the downstream neurons [**12**, **18**]. We explored a number of different scenarios. In the simplest situation, each synapse provided purely monocular, well-tuned input, corresponding to a situation in which each synapse represents a single source. In V1 of the mouse, simple cells in the binocular zone are binocular and their monocular preferred orientations can be quite well matched already during the period of interest [**18**]. This does, however, not imply that the monocular preferred orientations of the complex cells are already well-matched at that point, since the simple cells feeding into the complex cell, which have different preferred orientations, are dominated by different eyes, reflecting their broad distribution of the ODI. We investigated this situation for different ODI distributions. The results are qualitatively similar to those obtained in the monocular case, unless synapses providing inputs with ODI close to 0 dominate. In that case an additional matching mechanism becomes relevant.

Despite its simplicity, our model captured a number of fundamental experimental results for the development of orientation tuning in mouse V1 [**18**, **23**, **26**]. During the monocular phase a fraction of the cells became orientation-selective with respect to inputs from both eyes, but the preferred orientations were rarely matched. The matching occurred during the binocular phase and depended strongly on the ocular dominance of the neuron: for cells that were dominated by the input from one eye the matching process typically involved only small changes in the preferred orientation of the dominant eye, while the orientation of the weaker eye could change substantially [**26**]. For those cells the initial preferred orientation of the dominant eye is

a good predictor for the preferred orientation after matching. Considering all cells, in the model the initial binocularly preferred orientation predicts the final preferred orientation well. As in the experiment [**26**], the orientation selectivity was higher in well-matched cells and enhanced by correlated visual input [**31**]. Both results reflect the enhanced drive the cells receive once the monocular tuning curves overlap, which leads to stronger plastic changes as well as enhanced selectivity due to the synaptic homeostasis [**22**].

In the model the development of orientation selectivity and its matching are driven by different types of correlations in the inputs to the cells and therefore differ in their time course. Orientation selectivity starts to emerge already before eye-opening. After eye-opening visual input is expected to enhance cortical activity and with it the learning speed for orientation selectivity, consistent with the results of [**31**]. In the model the matching process requires correlated inputs from both eyes. It therefore suggests that matching does not start until eye-opening and persists then throughout the critical period. Indeed, experimental results suggest that at P15-P18, i.e., shortly after eye-opening, the matching of V1 cells is still close to chance level [**18**], which is consistent with the lack of matching in dark-reared mice [**23**]. However, already at the beginning of the critical period (P19-P21) the preferred orientations are somewhat matched [**18**]. Due to the presence of uncorrelated spontaneous activity during the phase between eye-opening and the critical period [**42**], the model suggests that during that phase the matching proceeds more slowly than during the critical period.

In the model, cells whose left and right monocular tuning curves overlap match more rapidly. Thus, for a given mismatch less selective cells are predicted to match faster. This is consistent with results obtained in mice that were reared in the dark from P1 to P30 [**23**]. At P30 the distribution of their mismatch was not statistically different from a uniform distribution and their selectivity was lower than that observed at the beginning of the critical period. As found in the model, their matching progressed faster than was the case for undeprived animals during the critical period. Conversely, binocular deprivation between eye-opening and the onset of the critical period has been found to increase the fraction of cells that have strong orientation selectivity [**40**] but large mismatch [**23**]. Our model predicts that their matching process will be slower.

Conversely, the model predicts that the mismatch affects the orientation selectivity. By manipulating the initial mismatch at fixed orientation selectivity, we showed that during the binocular matching process cells did not become more orientation-selective unless the mismatch was small enough to allow the monocular tuning curves to overlap.

Moreover, the overlap of the tuning curves is predicted to affect the matching process in a qualitative manner. For small mismatch, for which the tuning curves overlap significantly, the monocular preferred orientations are predicted to shift smoothly towards each other. For large mismatch, however, the model predicts that the response to input from one eye and its selectivity drop substantially during the evolution. If the plasticity period continues sufficiently long beyond that phase, this reduction

in response is only transient and the response eventually recovers with a preferred orientation that has switched to that of the input from the other eye. This switching process is predicted to be more likely after binocular deprivation between eye-opening and the onset of the critical period. If the switching occurs, however, late in the critical period, the remaining duration of the plastic period may not suffice for the recovery and the cell may remain essentially monocular. This has been reported experimentally for a fraction of L2/3 cells [**43**].

When the plasticity period in the model was sufficiently long, all cells became highly selective and very well matched, more so than observed experimentally [**23**]. This could result from an oversimplification of the plasticity mechanism or of the stimuli used in the simulations. Alternatively, it could suggest that biologically the overall plasticity process and its duration are not optimized specifically for orientation selectivity and matching, but could have additional objectives. This interpretation is supported by the observation that in the model the best orientation selectivity and matching would be achieved in the shortest time if there was no monocular period at all. However, it has been pointed out that such a monocular period during which contra- and ipsilateral inputs are uncorrelated is necessary to form retinogeniculate and geniculocortical connections with segregated eye-specific areas in LGN (reviewed by [**44**]).

In our model the plasticity resulted from changes in the synaptic weights that were driven by correlations between presynaptic spikes and the evolution of the postsynaptic voltage, combined with a homeostatic mechanism based on the postsynaptic

long-term activity [**22**]. We expect that most of our results do not depend qualitatively on the specific details of the plasticity mechanism as long as it has a Hebbian component that is based on the correlations between pre- and postsynaptic activities and that does not change the weights for low presynaptic activity, in combination with homeostatic regulation. Conceivably, the plasticity mechanism could have a strong structural component [**45**], which may be quite likely at this developmental stage of the animal.

To conclude, by modeling the development and binocular matching for a hypothetical cell in visual cortex V1, we captured a host of experimental results in mouse and give several predictions. Key elements of the model are the evolution and competition of two monocular receptive fields in the presence of correlated inputs. The simplicity of this framework makes it a good candidate to investigate the interaction between selectivity, channel-dominance, and mismatch of a specific physical property at the single neuron level during the matching process in multi-source experience-dependent sensory systems.

CHAPTER 3

Paradoxical phase response of gamma rhythms facilitates their entrainment in heterogeneous networks

3.1. Introduction

Collective oscillations or rhythms representing the coherent dynamics of a large number of coupled oscillators play a significant role in many systems. In the technological realm they range from laser arrays and Josephson junctions to micromechanical oscillators [**46**, **47**]. Among the important biological examples are the heart rhythm, the circadian rhythm generated by the suprachiasmatic nucleus [**48**], the segmentation clock controlling the somite formation during development [**49**], and brain waves [**50**]. One prominent brain rhythm is the widely observed γ-rhythm with frequencies in the range 30-100Hz. The coherent spiking of the neurons underlying this rhythm likely enhances the downstream impact of the neurons participating in the rhythm. The rhythmic alternation of low and high activity has been suggested to play a significant role in the communication between different brain areas [**51**, **52**]. That communication has also been proposed to be controlled by the coherence of the rhythms in the participating brain areas [**1**, **53**–**57**].

For collective oscillations or rhythms to play a constructive role in a system they need to respond adequately to external perturbations and stimuli. For instance, for the circadian rhythm it is essential that it is reliably entrained by light and phase-locks to the day-night cycle. Similarly, if rhythms are to play a significant role in the communication between different brain areas, their response to input from other areas represents a significant determinant of their function. Moreover, the stimulation and entrainment of γ-rhythms by periodic sensory input is being considered as a therapeutic approach for some neurodegenerative diseases [**58**].

Even small perturbations can affect oscillations significantly in that they can advance or delay the oscillations, i.e. they can change the phase of the oscillators. This change typically depends not only on the strength of the perturbation but, importantly, also on the timing of the perturbations and is expressed in terms of the phase response curve (PRC), which has been studied extensively for individual oscillators [**59**]. For infinitesimal perturbations the PRC can be determined elegantly using the adjoint method [**60**].

If the collective oscillation of a network of interacting oscillators is sufficiently coherent, that system can be thought of as a single effective oscillator. Consequently, the response of the macroscopic phase of the collective oscillation to external perturbations and the mutual interaction of multiple collective oscillations are of interest. The macroscopic phase-response curve (mPRC) has been obtained in various configurations, including noise-less heterogeneous phase oscillators [**61**, **62**], noisy identical phase oscillators [**63**, **64**], noisy excitable elements [**65**], and noisy

oscillators described by the theta-model [**66**], which is equivalent to the quadratic integrate-and-fire model for spiking neurons. Recent work has used the exact mean-field theory of [**67**], which is related to the Ott-Antonsen theory [**68**,**69**] and reduces the dynamics of networks of quadratic integrate-and-fire neurons to two coupled differential equations for the firing rate and the mean voltage, to develop a method to obtain the infinitesimal macroscopic PRC (imPRC) for excitatory-inhibitory spiking networks [**70**, **71**].

A key difference between the response of an individual oscillator to a perturbation and that of a collective oscillation is the fact that the degree of synchrony of the collective oscillation can change as a result of the perturbation, reflecting a change in the relations between the individual oscillators. Thus, the phase response of a collective oscillation to a brief perturbation consists not only of the immediate change in the phases of the individual oscillators caused by the perturbation, but includes also a change in the collective phase that can result from the subsequent convergence back to the phase relationship between the oscillators corresponding to the synchronized state, which is likely to have been changed by the perturbation [**62**]. Interestingly, it has been observed that the infinitesimal macroscopic phase response can be qualitatively different from the phase response of the individual elements. Thus, even if the individual oscillators have a type-I PRC, i.e. a PRC that is strictly positive or negative, the mPRC of the collective oscillation can be of type II, i.e. it can exhibit a sign change as a function of the phase [**65**, **66**, **72**].

Here we investigate the interplay between external perturbations and the internal interactions among neurons in inhibitory and in excitatory-inhibitory networks exhibiting γ-rhythms of the ING- and of the PING-type. We focus on networks comprised of neurons that are not identical, leading to a spread in their individual phases and a reduction in the degree of their synchrony. How does this phase dispersion affect the response of the macroscopic phase of the rhythm to perturbations? Does it modify the ability of the network to follow a periodic perturbation ?

We show that the dispersion in the phase together with the within-network interactions among the neurons can be the cause of a paradoxical phase response: an external perturbation that *delays* each individual neuron can *advance* the macroscopic rhythm. We identify the following mechanism underlying this paradoxical response: external perturbations that delay individual neurons sufficiently allow the within-network inhibition generated by early-spiking neurons to suppress the spiking of less excited neurons. This results in a reduced within-network inhibition, which reduces the time to the next spike volley, speeding up the rhythm. This paradoxical phase response increases with the neuronal heterogeneity and allows the network to phase-lock to periodic external perturbations over a wider range of detuning. Thus, the desynchronization within the network enhances its synchronizability with other networks. The mechanism is closely related to that underlying the enhancement of synchronization of collective oscillations by uncorrelated noise [**73**] and the enhanced entrainment of the rhythm of a homogeneous network to periodic input if that input exhibits phase dispersion across the network [**74**, **75**]. We demonstrate and analyze

these behaviors for networks of inhibitory neurons (ING-rhythm) and for networks comprised of excitatory and inhibitory neurons (PING-rhythm).

3.2. Methods

3.2.1. The network of integrate-and-fire (IF) neurons

Neuron model. Both E-cells and I-cells were modeled as leaky IF neurons, each characterized by a membrane potential $V_i(t)$ satisfying

$$\tau_{E,I}\frac{d}{dt}V_i = -(V_i - V_{rest}) + \frac{I_i^{(syn)}}{g_{syn}} + \frac{I_i^{(ext)}}{g_{ext}} + \frac{I_i^{(bias)}}{g_{bias}}\,, \tag{3.1}$$

where V_{rest} is the resting potential and $\tau_{E,I}$ the membrane time constants of the E- and I-cells, respectively. $I_i^{(syn)}(t) = \sum_j I_{ij}^{(syn)}(t)$ is the total synaptic current that the neuron receives from the other neurons within the network. $I_i^{(ext)}(t)$ is a time-dependent external input that represents perturbations applied to determine the fmPRC or, in the study of synchronization, the periodic input generated by the clock network. $I_i^{(bias)}$ denotes a tonic, neuron-specific excitatory bias current that implements the heterogeneity of the neuron properties, The corresponding conductances are denoted by g_{syn}, g_{ext}, and g_{bias}. Upon the i^{th} neuron reaching the spiking threshold V_{peak}, the voltage V_i was reset to the fixed value V_{reset}. Parameters for the neuron were kept fixed throughout all simulations (see Table 3.1). The local field potential (LFP) of the network was approximated as the mean voltage across all neurons $j = 1, ...N$ in the respective population.

Network model. We studied two types of networks: an ING network and a PING network. The ING network was modeled as an all-to-all inhibitory network of $N_I^{(ING)}$ interneurons. The PING network was modeled as a network of $N_I^{(PING)}$ interneurons and $N_E^{(PING)}$ principal cells with all-to-all interneuron-principal and principal-interneuron connections (i.e., without principal-principal and interneuron-interneuron connections). In PING, only principal cells received external input $I^{ext}(t)$.

To gain insight into the interaction between two ING rhythms, we considered the simplified situation in which all neurons in the network received strictly periodic input $I^{(ext)}$, which was generated by another ING network ('clock'). Similarly, for PING rhythms, the E-cells of the PING network received strictly periodic excitatory input $I^{(ext)}$ from another PING network through all-to-all connection between their E-populations.

Synaptic currents. We used delayed double-exponential conductance-based currents to model the excitatory and the inhibitory synaptic inputs from neuron j to neuron i,

$$I_{ij}^{(syn)}(t) = g_{syn}\frac{\tau_{E,I}}{\tau_2^{E,I} - \tau_1^{E,I}}\left(A_{ij}^{(2)}(t) - A_{ij}^{(1)}(t)\right)\left(V_{rev,j} - V_i(t)\right), \tag{3.2}$$

with the two exponentials $A_{ij}^{(1,2)}(t)$ satisfying

$$\frac{d}{dt}A_{ij}^{(1,2)}(t) = -\frac{A_{ij}^{(1,2)}(t)}{\tau_{1,2}^{E,I}} + \sum_k W_{ij}\delta(t - t_j^{(k)} - \tau_d)\,, \tag{3.3}$$

where $V_{rev,j}$ is the synaptic reversal potential corresponding to the synapse type, W_{ij} the dimensionless synaptic strength, and δ the Dirac δ-function. All synapses of the same type (I-I, I-E, E-I) were equally strong. The time constants of $A_i^{(1,2)}(t)$ satisfied $\tau_2^{E,I} > \tau_1^{E,I}$. The synaptic current was normalized to render the time integral independent of the synaptic time constants $\tau_{1,2}^{E,I}$. The inhibitory synaptic currents had a slower decay than the excitatory ones (cf. Table 3.1). We included an explicit synaptic delay τ_d in the model**.** Every spike of the presynaptic neuron j at time $t_j^{(k)}$ triggered a jump in both $A_{ij}^{(1,2)}(t)$, making the synaptic conductance rise continuously after a synaptic delay τ_d.

External periodic inputs were also modeled as double-exponential conductance-based currents with g_{syn} in (3.2,3.3) replaced by g_{ext}. The time constants and delay were as for the within-network synaptic inputs.

Heterogeneous tonic input. The bias currents $I_i^{(bias)}$ of the ING network were Gaussian distributed around $I^{(I)}$ with a coefficient of variation $CV^{(I)}$ and arranged in increasing order, $I_1^{(bias)} < I_2^{(bias)} ... < I_N^{(bias)}$

$$I_i^{(bias)} = I^{(I)} + \sqrt{2}I^{(I)}CV^{(I)}\mathrm{erf}^{-1}(-1 + \frac{2i}{1+N}), \qquad 1 \le i \le N, \tag{3.4}$$

where erf is the error function to implement the Gaussian distribution of the heterogeneity. For the PING network, all excitatory neurons received a heterogeneous bias

$I_E^{(bias)}$ with mean $I^{(E)}$ and a coefficient of variation $CV^{(E)}$. Similarly, the bias currents $I_I^{(bias)}$ to the inhibitory neurons were characterized by their mean $I^{(I)}$ and their coefficient of variation $CV^{(I)}$. Without the excitatory input from principal cells, the voltage of interneurons remained below the spiking threshold. In our investigation of the impact of the neuronal heterogeneity on the phase response and entrainment of the PING rhythm we kept $CV^{(I)}$ fixed and varied $CV^{(E)}$.

3.2.2. Macroscopic Phase-response Curve for Finite-Amplitude Perturbations (fmPRC).

ING rhythm. For a single ING network, we applied a single inhibitory δ-pulse to each neuron $j = 1, ...N_I^{(ING)}$ at time t_{inh} (dashed green line in Fig 3.1B) and recorded the resulting phase shift $\Delta\varphi$. The amplitude of the inhibitory perturbation to each neuron was the same. The phase of the inhibition relative to the rhythm was defined as

$$\phi_{inh} = \frac{t_{inh} - t_{firstspike}^{(unperturbed)}}{T}, \tag{3.5}$$

where T was the period of the network LFP and $t_{firstspike}^{(unperturbed)}$ the time of the first spike in the spike volley of the unperturbed network that was closest to t_{inh}. The phase shift $\Delta\phi$ resulting from the perturbation was given by

$$\Delta\phi = \frac{\left(t_{firstspike}^{(unperturbed)} - t_{firstspike}^{(perturbed)}\right)}{T}, \tag{3.6}$$

where $t_{firstspike}^{(perturbed)}$ is the time of the first spike in the corresponding volley in the perturbed network. $\Delta\phi$ and ϕ_{inh} were taken to be in the range $[-0.5\ 0.5)$. Positive $\Delta\phi$ indicated that the network was advanced by the perturbation, while negative indicated a delay.

The periodic input ('clock') that was used to test the synchronizability of the ING-rhythm was generated by a homogeneous ING network. The phase of the network relative to the periodic input in the n^{th} clock cycle was defined by

$$\Phi_{inh}^{(n)} = \frac{\left(t_{firstspike}^{(clock)(n)} + \tau_d - t_{firstspike}^{(network)(n)}\right)}{T}, \tag{3.7}$$

where $t_{firstspike}^{(network)(n)}$ was the time of the first spike in the spike volley of the network in the n^{th} cycle and $t_{firstspike}^{(clock)(n)}$ the time of the spike of the clock. In contrast to the definition of ϕ_{inh} in (3.5), the definition of $\Phi_{inh}^{(n)}$ included the delay τ_d, since the inhibition generated by the clock arrived with delay τ_d in the network.

PING rhythm. To probe the phase response of the PING network we used the same approach as for the ING rhythm, except that we used excitatory instead of inhibitory δ-pulses and applied them only to the E-cells. The phase of the excitation ϕ_{exc} and the resulting phase shift $\Delta\phi$ were determined similarly as in the case of the ING rhythm,

$$\phi_{exc} = \frac{t_{exc} - t_{firstspike}^{(unperturbed)}}{T}, \tag{3.8}$$

$$\Delta\phi = \frac{(t_{firstspike}^{(unperturbed)} - t_{firstspike}^{(perturbed)})}{T}, \tag{3.9}$$

where $t_{firstspike}^{(perturbed)}$ and $t_{firstspike}^{(unperturbed)}$ were the times of the first spike in the respective spike volleys of the E-population.

Analogous to $\Phi_{inh}^{(n)}$, the phase of the network during the n^{th} clock cycle was defined by

$$\Phi_{exc}^{(n)} = \frac{(t_{firstspike}^{(clock)(n)} + \tau_d - t_{firstspike}^{(network)(n)})}{T}. \tag{3.10}$$

Throughout, the tonic, Gaussian distributed input to the interneurons in the PING network was fixed: $I^{(I)} = 36$ pA, $CV^{(I)} = 0.167$.

ING network

Parameter	Value
τ_I, membrane time constant	20 ms
u_{rest}, resting potential	-55 mV
V_{peak}, spiking threshold	-50 mV
V_{reset}, reset voltage	-60 mV
τ_d, synaptic delay	3 ms
$N_I^{(ING)}$, # of interneurons	500
W, synaptic strength within the network	7.5×10^{-3}
$W^{(ext)}$, synaptic strength for the input from the clock network	1.8×10^{-3}

PING network

Parameter	Value
τ_E, membrane time constant of principal cells	20 ms
τ_I, membrane time constant of interneurons	10 ms
u_{rest}, resting potential	-70 mV
V_{peak}, spiking threshold	-52 mV
V_{reset}, reset voltage	-59 mV
τ_d, synaptic delay	1 ms
$N_I^{(PING)}$, # of interneurons	200
$N_E^{(PING)}$, # of principal cells	800
W^I, inhibitory synaptic strength within the network	5.4×10^{-3}
W^E, excitatory synaptic strength within the network	1.67×10^{-3}
$W^{(ext)}$, clock-network synaptic strength	1.6×10^{-3}

Synaptic currents

Parameter	Value
τ_1^E, time constant of rise in excitatory synapse	0.5 ms
τ_2^E, time constant of decay in excitatory synapse	2 ms
τ_1^I, time constant of rise in inhibitory synapse	0.5 ms
τ_2^I, time constant of decay in inhibitory synapse	5 ms
V_{rev}^I, reversal potential of inhibitory synapse	-70 mV
V_{rev}^E, reversal potential of excitatory synapse	0 mV

Synaptic conductances

Parameter	Value
Excitatory input on principal cells : $g_{ext}^{(PING)}$, $g_{bias\ E}^{(PING)}$	0.19 nS
Excitatory input on interneurons: $g_{bias}^{(ING)}$, $g_{syn\ EtoI}^{(PING)}$, $g_{bias\ I}^{(PING)}$	0.3 nS
Inhibitory input on principal cells: $g_{syn\ ItoE}^{(PING)}$	2.5 nS
Inhibitory input on interneurons: $g_{ext}^{(ING)}$, $g_{syn}^{(ING)}$	4 nS

Table 3.1. Parameters used in the network model of IF neurons. Most parameters are based on [**73**, **76**].

3.2.3. Networks of quadratic integrate-and-fire (QIF) neurons and their exact mean-field reduction

Neuron model. The QIF neuron [**77**] is characterized by a membrane potential $V_i(t)$ satisfying

$$\tau_{E,I}\frac{d}{dt}V_i = \eta_i + V_i^2(t) + I_{E,I}(t), \tag{3.11}$$

where $\tau_{E,I}$ are the membrane time constants of the E- and I-cells, respectively. $I_{E,I}(t)$ is the total synaptic current that the E-, I- neurons receive from the other neurons within the network. Upon the i^{th} neuron reaching the spiking threshold V_{peak}, the voltage V_i is reset to the fixed value V_{reset}. In order to facilitate the analysis of the reduction, the limit $V_{peak} \to \infty$, $V_{reset} \to -\infty$ is taken. Analogous to (3.4), the tonic, external bias currents $\eta_i = \bar{\eta}_{E,I} + \Delta_{E,I}\tan(\pi(\frac{i}{1+N} - \frac{1}{2}))$ implement the heterogeneity of the neuron properties and are distributed according to a Lorentzian distribution,

$$\mathcal{L}_{E,I}(\eta) = \frac{1}{\pi}\frac{\Delta_{E,I}}{(\eta - \bar{\eta}_{E,I})^2 + \Delta_{E,I}^2}, \tag{3.12}$$

with $\eta_1 < \eta_2 < ... < \eta_N$. Here $\bar{\eta}_{E,I}$ is the mean value in the principal value sense and $\Delta_{E,I}$ the half-width of the distribution of η for the E- and I-cells, respectively. Note that the heavy tail of the Lorentzian distribution implies that – for arbitrary $\bar{\eta}$ and Δ with sufficiently many neurons to resolve the tail – there are always neurons

receiving extremely weak input and unable to overcome the within-network inibition to spike. Parameters for the neuron were kept fixed throughout all simulations (see Table 3.2). Again, in the spiking network, the local field potential (LFP) of the network was approximated as the mean voltage across all neurons in the respective population.

Network model. We studied two types of QIF-networks: an ING network and a PING network. The ING network was modeled as an all-to-all inhibitory network of $N_I^{(ING)}$ interneurons. The PING network was modeled as a network of $N_I^{(PING)}$ interneurons and $N_E^{(PING)}$ principal cells with all-to-all interneuron-principal and principal-interneuron connections (i.e., without principal-principal and interneuron-interneuron connections).

Synaptic currents.

In the ING rhythm, the total synaptic current $I(t)$ to each I-cell is the recurrent inhibition:

$$I_I(t) = -\tau_I s_{II}(t) \ . \tag{3.13}$$

In the PING network, the total synaptic current $I(t)$ to each E-cell is the inhibition from the I-cells,

$$I_E(t) = -\tau_E s_{EI}(t) \ , \tag{3.14}$$

and that to each I-cell is given by the excitation from the E-cells,

$$I_I(t) = \tau_I s_{IE}(t) \ . \tag{3.15}$$

Here $s_{\alpha\beta}(t)$ denotes the synaptic variable characterizing the synapse from the population β to the population α. In order to include the effective synaptic delay, we assumed that each spike triggers a double-exponential current. Extending [**57**], the synaptic variable $s_{\alpha\beta}(t)$ is therefore modeled by

$$s_{\alpha\beta}(t) = s_{\alpha\beta,2}(t) - s_{\alpha\beta,1}(t) \tag{3.16}$$

with $s_{\alpha\beta,1}(t)$ and $s_{\alpha\beta,2}(t)$ satisfying

$$\frac{d}{dt} s_{\alpha\beta,1}(t) = -\frac{1}{\tau_1} s_{\alpha\beta,1}(t) + J_{\alpha\beta} r_\beta(t) \tag{3.17}$$

$$\frac{d}{dt} s_{\alpha\beta,2}(t) = -\frac{1}{\tau_2} s_{\alpha\beta,2}(t) + J_{\alpha\beta} r_\beta(t) \, . \tag{3.18}$$

Here $J_{\alpha\beta}$ is the synaptic strength. The time constants τ_1, τ_2 of $s_{\alpha\beta,1}(t)$, $s_{\alpha\beta,2}(t)$ satisfy $\tau_2 > \tau_1$. $r_{E,I}(t)$ are the population firing rates of the E- and I-populations, respectively.

The mean-field theory. As shown in [**67**], in the limit of infinitely many neurons, the system eqs.(3.11, 3.12) is described by coupled equations for the mean

potential and population firing rate,

$$\begin{cases} \tau_{E,I}\frac{d}{dt}r_{E,I}(t) = \frac{\Delta_{E,I}}{\pi\tau_{E,I}} + 2r_{E,I}(t)V_{E,I}(t) \\ \tau_{E,I}\frac{d}{dt}V_{E,I}(t) = V_{E,I}(t)^2 + \bar{\eta}_{E,I} + I_{E,I} - \tau_{E,I}^2\pi^2 r_{E,I}(t)^2\,, \end{cases} \tag{3.19}$$

where $V_{E,I}(t)$ is the mean potential and $r_{E,I}(t)$ the population firing rate of the respective populations.

So, with the synaptic current defined in eqs.(3.14– 3.18), the ING network is reduced to

$$\begin{cases} \tau_I\frac{d}{dt}r_I(t) = \frac{\Delta_I}{\pi\tau_I} + 2r_I(t)V_I(t) \\ \tau_I\frac{d}{dt}V_I(t) = V_I(t)^2 + \bar{\eta}_I - \tau_I\left(s_{II,2}(t) - s_{II,1}(t)\right) - \tau_I^2\pi^2 r_I(t)^2 \\ \frac{d}{dt}s_{II,1}(t) = -\frac{1}{\tau_1}s_{II,1}(t) + J_{II}r_I(t) \\ \frac{d}{dt}s_{II,2}(t) = -\frac{1}{\tau_2}s_{II,2}(t) + J_{II}r_I(t)\,, \end{cases} \tag{3.20}$$

while the PING network is reduced to

$$
\begin{cases}
\tau_I \frac{d}{dt} r_I(t) = \frac{\Delta_I}{\pi \tau_I} + 2 r_I(t) V_I(t) \\
\tau_I \frac{d}{dt} V_I(t) = V_I(t)^2 + \bar{\eta}_I + \tau_I \left(s_{IE,2}(t) - s_{IE,1}(t) \right) - \tau_I^2 \pi^2 r_I(t)^2 \\
\tau_E \frac{d}{dt} r_E(t) = \frac{\Delta_E}{\pi \tau_E} + 2 r_E(t) V_E(t) \\
\tau_E \frac{d}{dt} V_E(t) = V_E(t)^2 + \bar{\eta}_E - \tau_E \left(s_{EI,2}(t) - s_{EI,1}(t) \right) - \tau_E^2 \pi^2 r_E(t)^2 \\
\frac{d}{dt} s_{EI,1}(t) = -\frac{1}{\tau_1} s_{EI,1}(t) + J_{EI} r_I(t) \\
\frac{d}{dt} s_{EI,2}(t) = -\frac{1}{\tau_2} s_{EI,2}(t) + J_{EI} r_I(t) \\
\frac{d}{dt} s_{IE,1}(t) = -\frac{1}{\tau_1} s_{IE,1}(t) + J_{IE} r_E(t) \\
\frac{d}{dt} s_{IE,2}(t) = -\frac{1}{\tau_2} s_{IE,2}(t) + J_{IE} r_E(t)
\end{cases}
\tag{3.21}
$$

Infinitesimal macroscopic PRC (imPRC) of the reduced network. For a dynamical system like eqs.(3.20, 3.21), within the parameter regime admitting a stable limit cycle, the adjoint method can be applied to determine the macroscopic phase response for infinitesimal perturbations to the limit cycle [**60**]. To be consistent with the fmPRC obtained with the direct simulation of the spiking network, we adjusted the normalization condition to make the phase range from 0 to 1. Due to the Lorentzian distribution used for the QIF network input, some neurons spike incessantly, making it impossible to define the beginning of a spike volley. We therefore defined phase 0 as the peak of the synaptic variable $s_{II}(t) = s_{II,2}(t) - s_{II,1}(t)$ for the ING rhythm and as the peak of $s_{EI}(t) = s_{EI,2}(t) - s_{EI,1}(t)$ for the PING rhythm. The phase shift $\Delta\phi$ resulting from the perturbation was given by the time

difference between the peaks of $s_{II}(t)$ (ING rhythm) or $s_{EI}(t)$ (PING rhythm) in the perturbed and the unperturbed system normalized by the period.

ING network	
Parameter	Value
τ_I, membrane time constant	10
V_{peak}, spiking threshold	500 (spiking network) $+\infty$ (reduction)
V_{reset}, reset voltage	-500 (spiking network) $-\infty$ (reduction)
$N_I^{(ING)}$, # of interneurons in spiking network	5000
J_{II}, synaptic strength	15
$\bar{\eta}_I$, the mean of the bias input to interneurons	20
Synaptic currents	
τ_1, time constant of rise in all types of synapses	0.98
τ_2, time constant of decay in all types of synapses	1

PING network	
Parameter	Value
τ_E, membrane time constant of principal cells	10
τ_I, membrane time constant of interneurons	10
V_{peak}, spiking threshold	500 (spiking network) $+\infty$ (reduction)
V_{reset}, reset voltage	-500 (spiking network) $-\infty$ (reduction)
$N_I^{(PING)}$, # of interneurons in spiking network	5000
$N_E^{(PING)}$, # of principal cells in spiking network	5000
J_{EI}, inhibitory synaptic strength	15
J_{IE}, excitatory synaptic strength	15
$\bar{\eta}_E$, the mean of the bias input to principal cells	5
$\bar{\eta}_I$, the mean of the bias input to interneurons	-5

Table 3.2. Parameters used in the network model of QIF neurons and its eMFT reduction. Most parameters are based on [**57**, **71**].

3.3. Results

We investigated the impact of neuronal heterogeneity on the response of the phase of γ-rhythms to brief external perturbations and the resulting ability of rhythms to synchronize to periodic input. As described in the Methods, we used networks comprised of minimal linear (IF) and quadratic (QIF) integrate-and-fire neurons

that interact with each other through synaptic pulses modeled via delayed double-exponentials. To study ING-rhythms, all neurons were inhibitory and all-to-all coupled, while for the PING-rhythms we used excitatory-inhibitory networks with all-to-all E-I and I-E connections. Throughout, we implemented the neuronal heterogeneity by injecting a different steady bias current I_{bias} into each neuron. Our analysis suggests that the origin of the neuronal heterogeneity plays only a minor role as long as it leads to a dispersion of their spike times [**73**].

3.3.1. Paradoxical Phase Response of Heterogeneous Networks: ING-Rhythm

In the absence of external perturbations the all-to-all inhibition among the neurons leads to rhythmic firing of the neurons. Due to their heterogeneity they did not spike synchronously but sequentially, as shown in Fig 3.1A, where the neurons are ordered by the strength of their bias current. The dependence of the phase dispersion on the coefficient of variation of the heterogeneity in the bias current (CV) is shown in Fig 3.1C. For sufficiently large heterogeneity some neurons never spiked: while the weak bias current they received would have been sufficient to induce a spike eventually, the strong inhibition that was generated by the neurons spiking earlier in the cycle suppressed those late spikes. Neurons with strong bias current could spike multiple times.

A brief, inhibitory external input delivered to all neurons (green dashed line in Fig 3.1B) delayed each neuron. The degree of this individual delay depended on

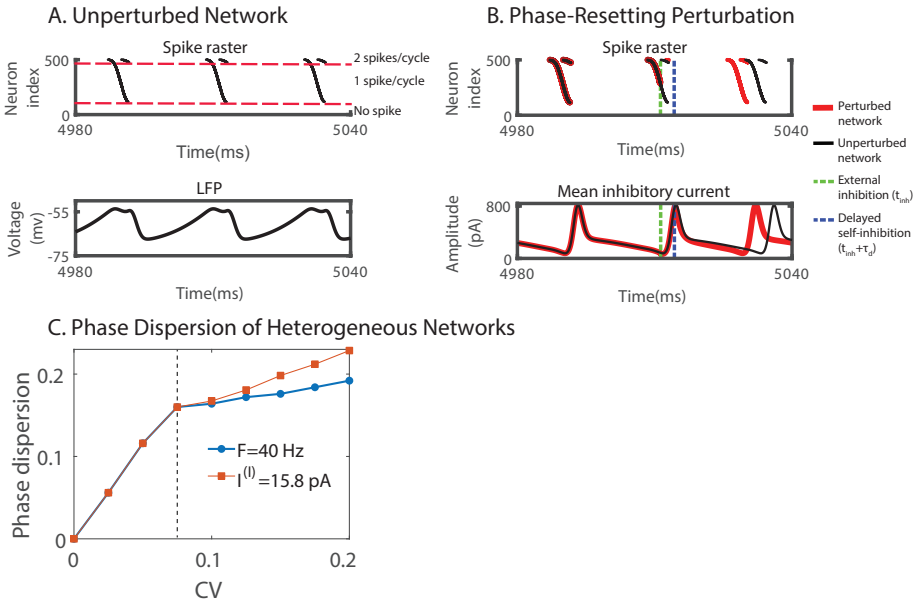

Figure 3.1. ING-rhythm can be advanced by inhibition while individual neurons are delayed. (A) Top: spike raster of neurons spiking sequentially on the order of their input strength (increasing with neuron index). Bottom: mean voltage across the network (LFP). (B) External inhibition advanced the rhythm. Top: raster plot of spikes without (black) and with (red) external inhibitory pulse. Bottom: Average of the total inhibitory current each neuron received from the other neurons within the network. In (A) and (B), $I^{(I)} = 20.4$ pA, $C_V^{(I)} = 0.15$, $f_{network} = 47$ Hz. In (B), perturbations were made with a square-wave inhibitory current pulse with duration 0.1 ms and amplitude 3200 pA to each neuron, resulting in a 4 mV rapid hyperpolarization. (C) Dependence of the phase dispersion on the heterogeneity of the bias current. The phase dispersion was determined as the time difference between the first and the last spike in the same spike volley normalized by the period. Blue: fixed natural frequency ($f_{network} = 40$Hz) for different neuronal heterogeneity. Red: fixed mean input strength ($I^{(I)} = 15.8$ pA) for different neuronal heterogeneity. For $CV \geq 0.075$ (dashed line), some neurons spike more than once in a cycle.

the timing of the input, as is reflected in the PRC of the individual neurons. If the perturbation was applied during the time between the spike volleys, the delay of each neuron had no further consequence and the overall rhythm was delayed. However, if the same inhibitory perturbation arrived during a spike volley (dashed green line in

Fig 3.1B), it could advance the overall rhythm. As illustrated in Fig 3.1B, only the spiking of the late neurons was delayed by the perturbation. Importantly, with this delay some neurons did not spike before the within-network inhibition triggered by the early-spiking neurons (dashed blue line in Fig 3.1B) became strong enough to suppress the spiking of the late neurons altogether. With fewer neurons spiking, the all-to-all inhibition within the network was reduced, allowing all neurons to recover earlier, which lead to a shorter time to the next spike volley. If the speed-up was larger than the immediate delay induced by the external inhibition, the overall phase of the rhythm was advanced by the delaying inhibition.

As the example in Fig 3.1B shows, the paradoxical phase response requires proper timing of the perturbation. We therefore determined quantitatively the macroscopic phase-response curve (mPRC) of the rhythm. To do so we measured computationally the amount a brief current injection shifted the phase of the rhythm (Fig 3.2A). We defined the phase ϕ_{inh} of the perturbation as the normalized time since the first spike in the most recent volley of spikes. Reflecting the strictly positive PRC of the individual IF neurons, without heterogeneity ($CV = 0$) external inhibition always delayed the rhythm, independent of the timing of the pulse. In contrast, in heterogeneous networks the rhythm could be advanced if the same inhibitory perturbation was applied shortly after the first spikes in the spike volley ($\phi_{inh} > 0$). Increasing the neuronal heterogeneity enhanced this phase advance, since it shifted the within-network inhibition driven by the leading neurons to earlier times, while it delayed the lagging neurons. As a result, for the same external perturbation, a

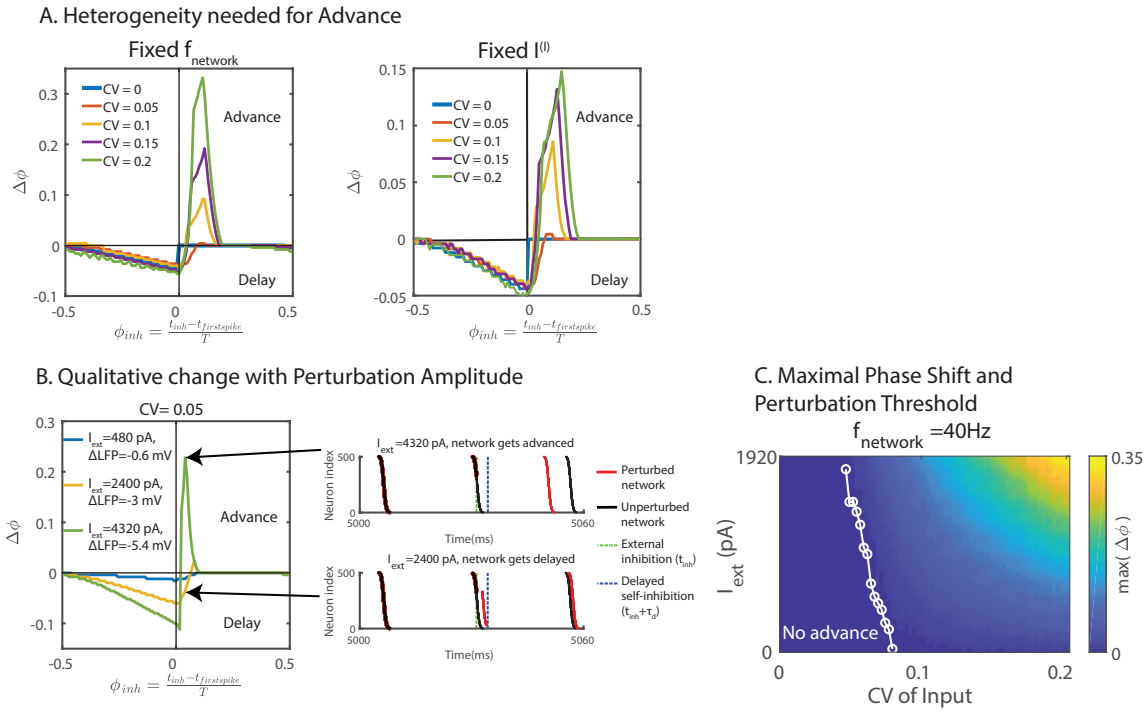

Figure 3.2. fmPRC of heterogeneous ING network. (A) Phase shift in response to inhibition for different neuronal heterogeneity but fixed natural frequency (left, $f_{network}$ = 40Hz) or fixed steady current (right, $I^{(I)}$ =15.8 pA). The paradoxical phase advance increased with neuronal heterogeneity. (B) fmPRC changed qualitatively with the amplitude of the perturbation. Left: fmPRC for three different perturbation amplitudes. Right: raster plot of spikes without (black) and with (red) external inhibition. Top: strong perturbation advanced the network. Bottom: weak perturbation applied at the same time as in the top figure. The network was delayed. (C) Maximal phase advance as a function of neuronal heterogeneity and external inhibition strength. The threshold of the inhibition amplitude to obtain an advance decreased with heterogeneity (white line). $f_{network}$ was kept constant ($f_{network}$ = 40Hz). In (A)-(C), perturbations were made with a square-wave inhibitory current pulse with duration 0.1 ms to each interneuron. In (A), the amplitude of the current was 1600 pA, resulting in a 2 mV rapid hyperpolarization.

larger fraction of neurons that would spike in the absence of the external inhibition was sufficiently delayed to have their spikes be suppressed by the within-network inhibition (cf. Fig 3.1B), reducing the within-network inhibition and with it the

time to the next spike volley. To keep the frequency of the unperturbed network fixed in Fig 3.2A left, we reduced the tonic input with increasing heterogeneity, which enhanced the phase advance. However, even if the tonic input was kept fixed, the phase advance increased with heterogeneity (Fig 3.2A right).

For weak heterogeneity the paradoxical phase response occurred only for sufficiently strong perturbations, i.e. it did not arise in the infinitesimal macroscopic PRC (imPRC). Thus, the phase response changed qualitatively when the amplitude of the perturbation was strong enough to delay the spikes of sufficiently many slow neurons until the self-inhibition of the network set in and suppressed their spikes (Fig 3.2B). With sufficiently large heterogeneity, the dispersion was large enough that the spikes of the lagging neurons were suppressed by the self-inhibition of the network even in the absence of an external perturbation. In that regime the paradoxical phase response occurred even for infinitesimal perturbations (to the right of the white line in Fig 3.2C).

The paradoxical phase response was robust with respect to changes in the natural frequency of the network, the coupling strength, and the effective synaptic delay, as long as the rhythm persisted. The paradoxical phase advance increased with decreasing natural frequency of the network, since the inhibition had a stronger effect for lower mean input strength (Fig 3.3A). Varying the within-network coupling strength by more than a factor of 20 only moderately affected the paradoxical phase response (Fig 3.3B) and the strength of the rhythm (Fig 3.3C). With increasing within-network coupling strength, a larger fraction of spiking neurons was delayed,

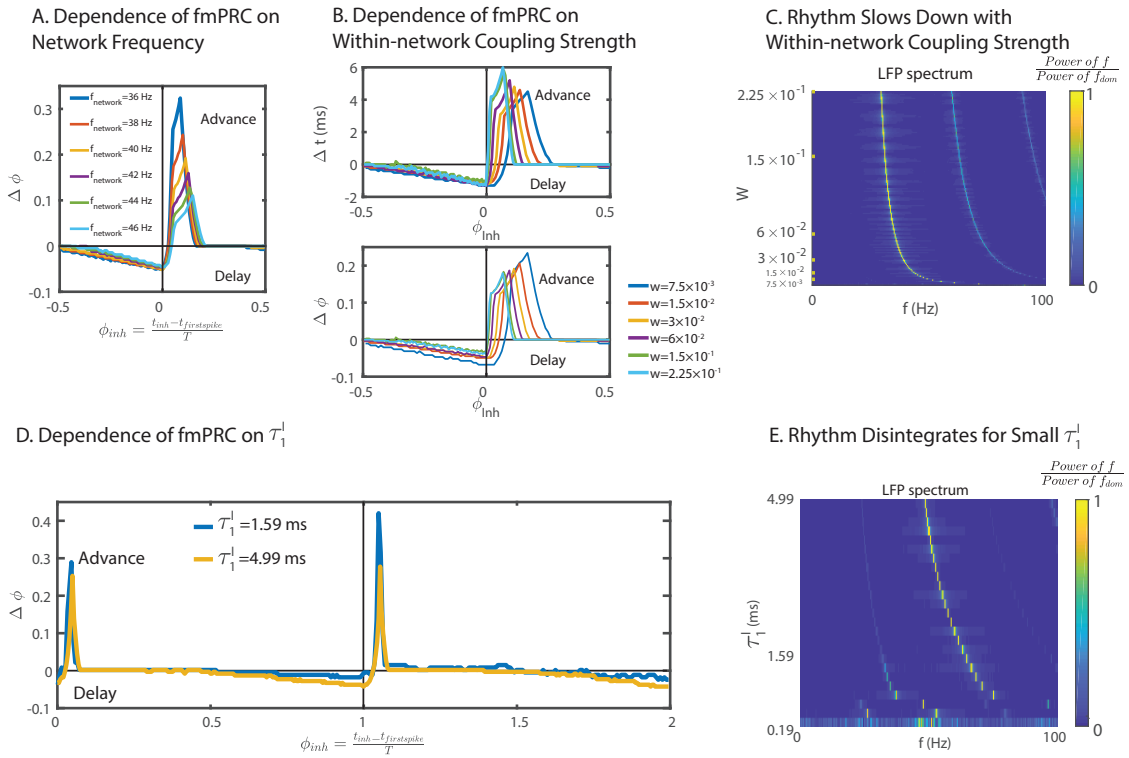

Figure 3.3. The paradoxical phase response of a heterogeneous ING network is robust. (A) The phase advance of the fmPRC decreased with the natural frequency ($CV^{(I)} = 0.15$). (B) The fmPRC did not depend sensitively on the within-network coupling strength W ($CV^{(I)} = 0.15$, $I^{(I)}$ =15.8 pA). Top: the temporal advance increased with within-network coupling strength. Bottom: the phase advance decreased with within-network coupling strength. (C) The Fourier spectrum of the LFP as a function of the within-network coupling strength W. Parameters as in (B). (D) Paradoxical phase response in the absence of an explicit delay, $\tau_d = 0$, for different synaptic rise times τ_1^I ($CV^{(I)} = 0.05$, $I^{(I)}$ =15.8 pA). For low τ_1^I (blue curve), the PRC alternated in subsequent cycles reflecting the subharmonic nature of the rhythm, but it still showed a strong paradoxical component. (E) The Fourier spectrum of the LFP as a function of the synaptic time constant of rise τ_1^I. With decreasing τ_1^I, a subharmonic peak emerged and eventually the rhythm disintegrated. Parameters as in D. In (A), (B) and (D), perturbations were made with a square-wave inhibitory current pulse with duration 0.1 ms to each interneuron. In (A) and (B), the amplitude of the current was 1600 pA, resulting in a 2 mV rapid hyperpolarization. In (D), the amplitude of the current was 400 pA, resulting in a 0.5 mV rapid hyperpolarization.

resulting in a larger temporal advance (Fig 3.3B top). Nevertheless, since the rhythm slowed down with increasing within-network coupling strength (Fig 3.3C, size of the perturbations in Fig 3.3B marked in the y-axis tick labels), the phase advance, which was defined as the temporal advance normalized by the period of the LFP, decreased with coupling strength (Fig 3.3B bottom). Additionally, even without explicit synaptic delay ($\tau_d = 0$), the effective delay given by the double-exponential synaptic interaction was sufficient to render a paradoxical response (Fig 3.3D). However, when this effective delay was reduced by decreasing the rise time τ_1^I of the synaptic current, the rhythm itself developed a strong subharmonic component and eventually disintegrated (Fig 3.3E). In the subharmonic regime the paradoxical phase advance alternated in consecutive cycles of the rhythm (yellow line in Fig 3.3D).

3.3.2. Enhancing entrainment of ING-rhythms through neuronal heterogeneity

In order to allow communication by coherence [**55**, **78**], the rhythms in different brain areas need to be sufficiently phase-locked with each other. As a simplification of two interacting γ-rhythms, we therefore investigated the ability of the rhythm in a network to be entrained by a periodic external input, particularly focusing on the possibly facilitating role of neuronal heterogeneity. Motivated by the paradoxical phase response induced by the heterogeneity, we addressed, in particular, the question whether an ING network can be sped up by inhibition to entrain it with a faster network.

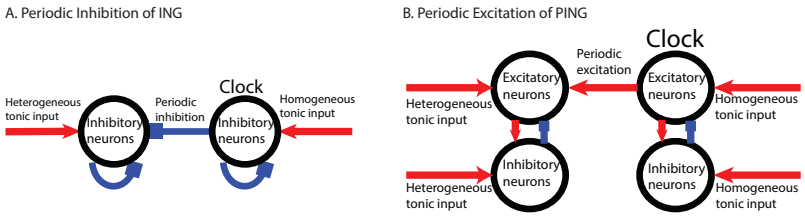

Figure 3.4. Sketch of computational models. (A) ING rhythm receives periodic inhibitory input generated from another 'clock' ING rhythm. (B) PING rhythm receives periodic excitatory input by its E-population generated from another 'clock' PING rhythm.

The network considered here was the same as that used to analyze the fmPRC. The within-network interaction was an all-to-all inhibition with synaptic delay τ_d, resulting in a rhythm with natural frequency $f_{natural}$. Each neuron received heterogeneous input I_{bias} and inhibitory periodic pulses with frequency f_{clock}. The latter can be considered as the output of another ING-network and were, in fact, generated that way (Fig 3.4A). We refer to this external input as the 'clock'. All neurons in the 'clock' network received the same input. Thus, their spiking had no dispersion and their spikes were perfectly synchronous. The detuning $\Delta f = f_{clock} - f_{natural}$ was a key control parameter.

For periodic input the fmPRC allows the definition of an iterated map for the phase $\Phi_{inh}^{(n)}$ of the network relative to the n^{th} clock cycle. For periodic δ-pulses that map is shown in Fig 3.5A. For positive detuning, i.e. when the clock is faster than the network, entrainment requires that the phase response is paradoxical in order for the rhythm to be sped up by the inhibition. If the heterogeneity and the resulting phase response are sufficiently large, the maximum of the iterated map crosses the

diagonal, generating a stable and an unstable fixed point. The former is the desired entrained state.

As the detuning is increased the iterated map is shifted downward. This can decrease the slope of the iterated map at the fixed point below -1, destabilizing the fixed point in a period-doubling bifurcation. For periodic pulses comprised of double-exponential inhibitory currents (cf. eqs.(3.2,3.3)) a rich bifurcation scenario emerged (Fig 3.5B). Note that the strength of the periodic input is significantly larger than that of the δ-pulses used in Fig 3.5A. As a result, the map is not continuous and not unimodal (cf. first bottom panel of Fig 3.5B). Nevertheless, for $\Delta f < 7.17$ Hz the attractor remains near the unstable fixed point and displays a period-doubling cascade to chaos and multiple periodic windows. For $\Delta f > 7.28$ Hz, however, the attractor includes points on both sides of the discontinuity (cf. third bottom panel in Fig 3.5B).

Having clarified the role of the fmPRC in the network's synchronizability and ability to phase-lock, we investigated the role of neuronal heterogeneity in more detail (Fig 3.6). To do that, we adjusted for each value CV of the input heterogeneity the mean input strength $I^{(I)}$ (cf. eqs.(3.4)) so as to keep the natural frequency $f_{network}$ constant ($f_{network} = 44$ Hz). Then we determined the extent of synchronization and phase-locking of the network under the influence of periodic inhibitory input as a function of the detuning Δf and neuronal heterogeneity CV. As shown above, with heterogeneity, the fmPRC could be biphasic with the amplitude of the paradoxical phase response increasing with neuronal heterogeneity. Expecting that

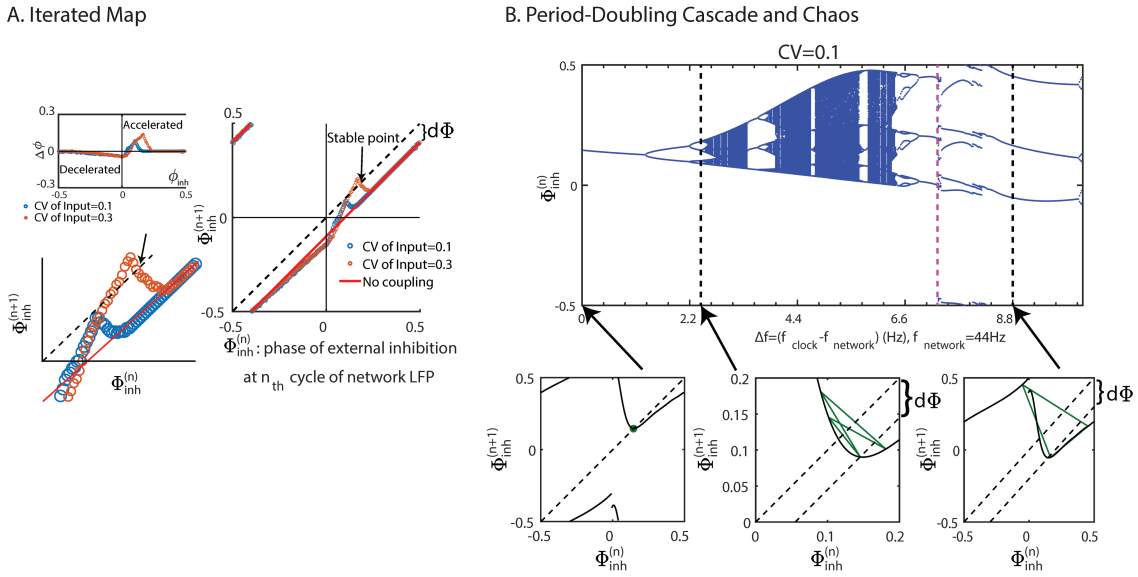

Figure 3.5. Connection between fmPRC and the synchronization of γ-rhythms. (A) Iterated map for the phase $\Phi_{inh}^{(n)}$ of the network relative to the periodic inhibition. Without coupling the network falls back by $d\Phi$ in each cycle. For sufficiently large advancing phase response the network can be synchronized by faster periodic inhibition. (B) Top: The bifurcation diagram of the iterated map for $\Phi_{inh}^{(n)}$ with varying detuning Δf. To the right of the magenta dashed line ($\Delta f = 7.28$ Hz) the attractors involve points on both sides of the discountinuity of the map. Bottom from left to right: iterated maps for $\Phi_{inh}^{(n)}$ for $\Delta f = 0, 2.44, 8.8$ Hz. The distance between the diagonal and subdiagonal line represents the detuning between the network and periodic input. In (A), the fmPRC was determined for a δ-pulse perturbation, in (B) for a double-exponential inhibitory current (cf. eqs.(3.2,3.3)) was used as in Fig 3.6.

for sufficiently large heterogeneity an ING-rhythm could be accelerated by a faster periodic inhibition, we tested phase-locking predominantly for positive detuning, corresponding to $f_{clock} > f_{network}$. We first investigated how neuronal heterogeneity affected the synchronization by comparing the dominant frequency f_{dom} in the

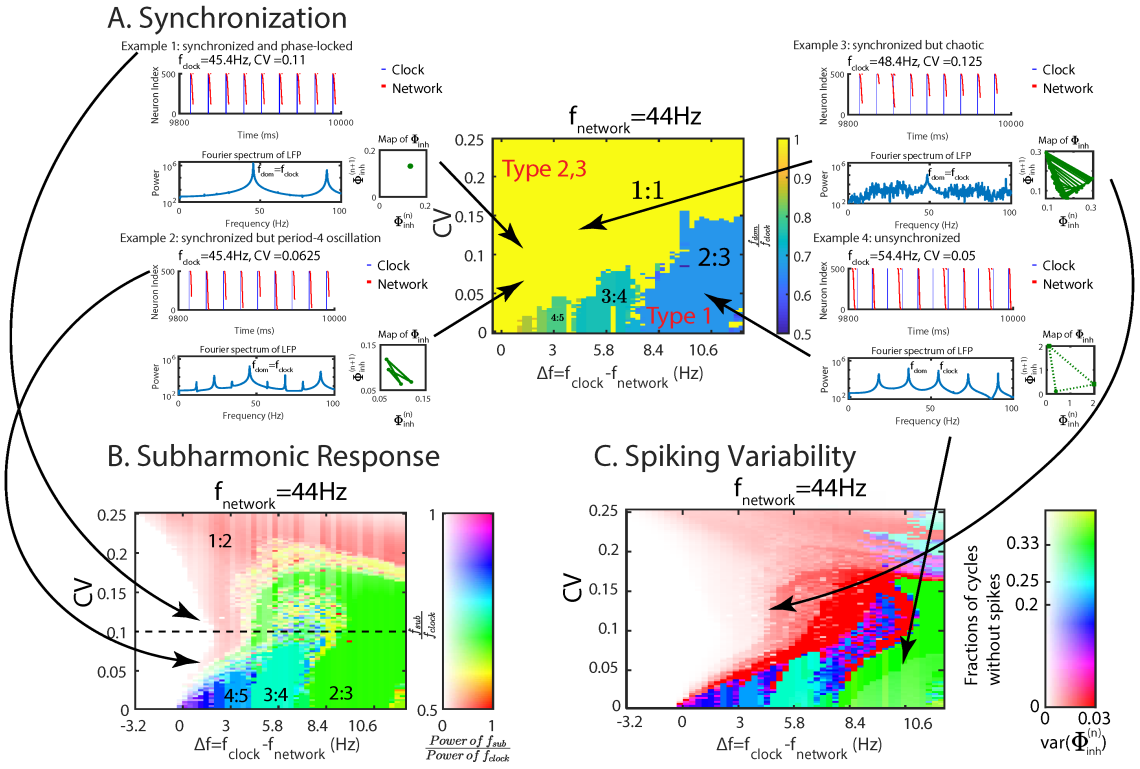

Figure 3.6. Neuronal heterogeneity enhances synchronization and phase-locking of periodically driven ING rhythm. (A) Synchronization quantified using $f_{dom} : f_{clock}$ with f_{dom} and f_{clock} being the dominant frequencies of the Fourier spectrum of the LFP of the network and the clock, respectively. The neuronal heterogeneity enhanced the synchronization by shifting f_{dom} to f_{clock}. Example 1: Synchronized with 1:1 phase-locking. Example 2: Synchronized with subharmonic response (period 4). Example 3: synchronized with subharmonic response (chaotic). Example 4: Not synchronized. Squares and dashed lines in the iterated map for $\Phi_{inh}^{(n)}$ indicate clock cycles in which the network did not spike ($\Phi_{inh}^{(n)}$ was arbitrarily set to 2). (B) Subharmonic response. Color hue and saturation indicate the frequency ratio $f_{sub} : f_{clock}$ and the ratio of the Fourier power at these two frequencies. f_{sub} is the frequency of the dominant peak of the network power spectrum that satisfies $f_{sub} < f_{clock}$. The power ratio is capped at 1. Dashed line marks the value of input heterogeneity used in Fig 3.5B. (C) Spiking variability and var($\Phi_{inh}^{(n)}$) as a function of neuronal heterogeneity and detuning. Color hue indicates the fraction of clock cycles without spikes in the network. In particular, red indicates that the network spikes in every cycle. Color saturation indicates var($\Phi_{inh}^{(n)}$). The neuronal heterogeneity enhances the tightness of the phase-locking.

Fourier spectrum of the network's LFP with f_{clock}. In Fig 3.6A, the color hue indicates the ratio $f_{dom} : f_{clock}$. For small heterogeneity, f_{dom} was a rational multiple of f_{clock} that depended on the detuning, while for sufficiently large CV the network became synchronized in the sense that $f_{dom} = f_{clock}$ (yellow). The range of Δf allowing synchronization became wider with increasing neuronal heterogeneity, implying that the neuronal heterogeneity enhanced the synchronization of the ING-rhythm. However, note that $f_{dom} = f_{clock}$ did not imply a perfectly synchronized or a 1:1 phase-locked state. In fact, various different subharmonic responses arose: example 2 shows a period-4 state, while in example 3 the dynamics were actually chaotic (Fig 3.6A) even though $f_{dom} = f_{clock}$. Motivated by these observations, we divided the states into three types:

- Type 1: $f_{dom} \neq f_{clock}$, not synchronized, not phase-locked (Fig 3.6 example 4).
- Type 2: $f_{dom} = f_{clock}$ with subharmonic response ('frequency synchronization'). The network may display rational ratio phase-locking with the forcing (Fig 3.6 example 2) or may be poorly phase-locked (Fig 3.6 example 3).
- Type 3: $f_{dom} = f_{clock}$, no subharmonic response, ('phase synchronization'). The network is 1-to-1 phase-locked with the forcing (Fig 3.6 example 1).

The phase diagram Fig 3.6A does not differentiate between types 2 and 3. It only shows that neuronal heterogeneity enhanced the synchronization of the network by shifting f_{dom} to f_{clock}. Therefore, we studied whether neuronal heterogeneity also

enhanced the synchronization by weakening the subharmonic response and changing the synchronized state from type 2 to type 3, as well as whether the dynamics of the fmPRC shown in the bifurcation diagram Fig 3.5B could predict the phase relationship between the network and the clock. Using the same simulation setup as in Fig 3.6A, the subharmonic response is shown in Fig 3.6B. The color hue indicates the ratio $f_{sub} : f_{clock}$, where f_{sub} is the frequency of the dominant peak of the LFP power spectrum that satisfies $f_{sub} < f_{clock}$. The color saturation gives the ratio of the powers at f_{sub} and f_{clock} (capped at 1). Thus, over most of the range of positive detuning and neuronal heterogeneity tested, the fading-away of the color with increasing heterogeneity reveals that the neuronal heterogeneity weakened the subharmonic response. Over a small range of positive detuning, increasing neuronal heterogeneity from small values induced perfect synchronization (type 3) by weakening the subharmonic response with frequency ratio $f_{sub} : f_{clock} = 1 : 2$; the system traversed a continuous period-doubling bifurcation in reverse, with type 2 (red) giving way to type 3 (white). Together with Fig 3.6A, this showed that neuronal heterogeneity could enhance the synchronization both by making $f_{dom} = f_{clock}$ (from type 1 to type 2) and by weakening the subharmonic response (from type 2 to type 3). The range of detuning where increasing heterogeneity induced a type 3 synchronization became wider for larger synaptic delay within the network (Fig3.7). Note that the bifurcation diagram (Fig 3.5B) based on the fmPRC agrees well with the subharmonic response marked along the dashed line at $CV = 0.1$ in Fig 3.6B,

suggesting that the fmPRC can well predict the subharmonic response and persistent phase response of the network.

In addition to enhancing the frequency synchonization, neuronal heterogeneity was also able to increase the tightness of the phase-locking. Over most of the parameter regime investigated, the variance of the phase of the network relative to the periodic input $\mathrm{var}(\Phi_{inh}^{(n)})$ decreased with increasing heterogeneity, as indicated by the decrease in the color saturation in Fig 3.6C. In fact, for detuning between 0 Hz and 2 Hz the heterogeneity reduced $\mathrm{var}(\Phi_{inh}^{(n)})$ to 0 (white), corresponding to the 1:1 phase-locked state. Even for the 1:2 phase-locked state (cf. the red area in Fig 3.6B) $\mathrm{var}(\Phi_{inh}^{(n)})$ was very small for a range of heterogeneity and detuning (2 Hz to 4 Hz), indicating tight phase locking. Except for type-3 synchronized states the size of the spike volleys varied between clock cycles. In fact, over wide ranges of the parameters the network did not spike in each of the clock cycles, as indicated by the color hue in Fig 3.6C, which gives the fraction of cycles with no network spikes (e.g., Fig 3.6 example 4).

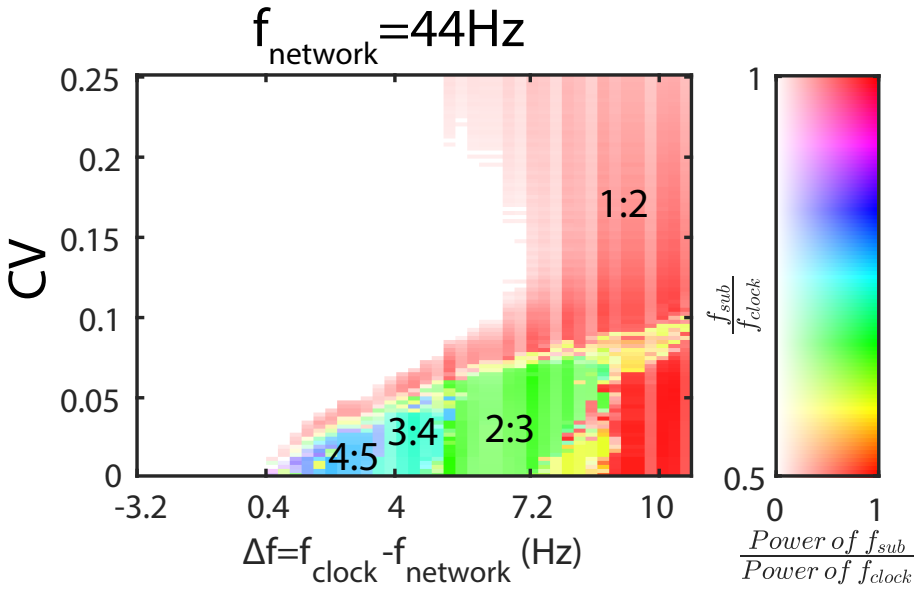

Figure 3.7. Subharmonic response of the ING rhythm with a longer synaptic delay within the network ($\tau_d = 5$ ms) receiving periodic inhibitory input. For each value of the input heterogeneity, the natural frequency $f_{network}$ was kept constant ($f_{network} =$ 44 Hz) by adjusting the mean input strength $I^{(I)}$. The range of detuning where increasing heterogeneity induced a type 3 synchronization became wider compared to Fig 3.6B, where $\tau_d = 3$ ms. $W^{(ext)} = 1.2 \times 10^{-3}$.

3.3.3. Paradoxical phase response and entrainment of PING rhythms

Many γ-rhythms involve not only inhibitory neurons, but arise from the mutual interaction of excitatory (E) and inhibitory (I) neurons (PING rhythm) [**79**]. The key elements to obtain a paradoxical phase response and the ensuing enhanced synchronization are self-inhibition within the network, neuronal heterogeneity and effective synaptic delay. Since in PING rhythms the connections from E-cells to I-cells and back to the E-cells form an effective self-inhibiting loop, we asked whether PING-rhythms can exhibit behavior similar to the behavior we identified for ING-rhythms.

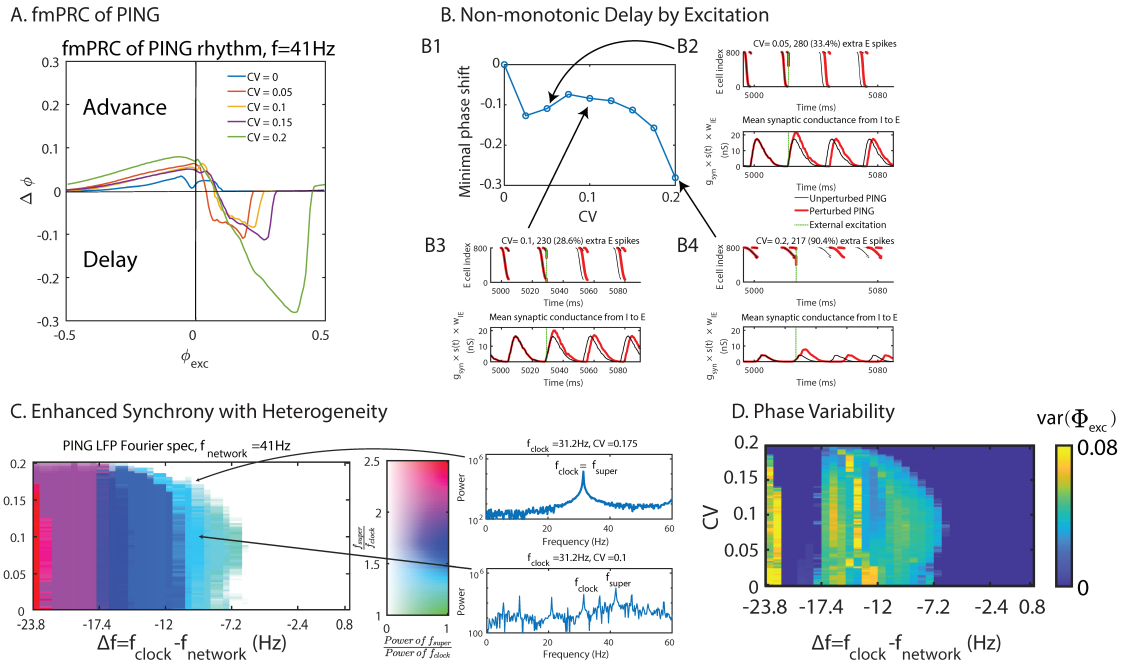

Figure 3.8. Neuronal heterogeneity enhances the synchronization and the tightness of phase-locking of the PING rhythm. (A) fmPRC of PING networks with constant natural frequency ($f_{network}$ = 41 Hz) but different neuronal heterogeneity. Only with neuronal heterogeneity the phase was delayed by the excitation. (B) Non-monotonicity of the paradoxical delay with constant natural frequency ($f_{network} = 41$ Hz). B2-4: Top: raster plot of spikes in E-population (input strength increased with cell index). Bottom: mean inhibitory synaptic conductance within the PING network. The titles show the absolute and relative increase in spike number (B2: $CV = 0.05$, B3: $CV = 0.1$, B4: $CV = 0.2$). (C) Subharmonic response of the PING rhythm with periodic excitation as function of neuronal heterogeneity and detuning. $f_{network}$ was fixed at 41 Hz. Color hue and saturation indicate the frequency ratio and power ratio at the frequencies f_{super} and f_{clock} of the E-population's LFP. f_{super} was the frequency of the dominant peak of the LFP power spectrum that satisfies $f_{super} > f_{clock}$. The power ratio was capped at 1. Generally, the neuronal heterogeneity enhanced the synchronization of the PING rhythm by weakening subharmonic response. (D) The tightness of the phase-locking ($var(\Phi_{exc})$) as a function of neuronal heterogeneity and detuning. The neuronal heterogeneity enhanced the tightness of the phase-locking. For $\Delta f \in [-22\text{Hz}, -17.4\text{Hz}]$ the clock was twice as fast as the network, resulting in vanishing $var(\Phi_{exc})$.

Considering a PING-rhythm generated by an E-I network comprised of IF neurons, we first studied its fmPRC. To avoid that all I-cells receive identical input and therefore spike as a single unit, the I-cells received, in addition to the excitation from the E-cells, heterogeneous, tonic, Gaussian-distributed subthreshold input with mean $I^{(I)} = 36$ pA and $CV^{(I)} = 0.167$. The phase response of the network was probed by applying an identical external excitatory perturbation to all E-cells and recording the resulting phase shift (cf. eqs.(3.8,3.9)) of the E-population, averaged across 500 realizations of the subthreshold input to the I-cells (Fig 3.8A). More specifically, the perturbations consisted of a square-wave excitatory current pulse with amplitude 76 pA and duration 0.1 ms to each E-cell, resulting in a 2 mV rapid depolarization. Without neuronal heterogeneity the external excitation always advanced the phase of the rhythm resulting in an fmPRC that was strictly positive. In the heterogeneous case, however, the PING rhythm exhibited a paradoxical phase response, whereby the collective rhythm was delayed while the individual neurons were advanced by the excitation. The delay was caused by the increase of self-inhibition within the network that was generated by the additional spikes in the E-population, which in turn drove additional spikes in the I-population. In contrast to the fmPRC of the ING-rhythm, this paradoxical phase response was not monotonic in the heterogeneity. While weak heterogeneity resulted in strong delay, the delay decreased with increasing intermediate CV-values and only increased again for larger CV (Fig 3.8B left top). This non-monotonicity arose because we kept the frequency of the network constant as we increased its heterogeneity. This required a decrease in the tonic input

to the E-cells with increasing heterogeneity. For the stronger tonic input used for weak heterogeneity the same external perturbation elicited more additional spikes than it did for strong heterogeneity where the tonic input was weaker (cf. titles of subpanels of Fig 3.8B). The total number of spikes occurring in each cycle of the unperturbed network also decreased with increasing heterogeneity. Consequently, the relative change in the number of spikes and in the inhibitory synaptic conductance induced by the perturbation were non-monotonic in the heterogeneity. As a result, the phase delay became non-monotonic.

As for the ING rhythm, we investigated the role of neuronal heterogeneity in the synchonizability and the ability of phase-locking of coupled PING rhythms. In analogy to the ING-case, we considered the case of the E-population of a PING network receiving periodic excitation generated by a clock PING network (Fig 3.4B). As before, we adjusted the tonic input strength to the E-population to keep the natural frequency of the network constant as we changed its heterogeneity ($f_{network} = 41$Hz). To probe the impact of the paradoxical phase response on the synchronization we focused on negative detuning for which the periodic external excitation needed to slow down the network in order to achieve phase-locking. Indeed, with increasing heterogeneity the network could become synchronized with the slower clock over a larger range of the detuning as indicated by the fading saturation of the color in Fig 3.8C. Here the color hue indicates the ratio $f_{super} : f_{clock}$, where f_{super} was determined as the frequency with the most power among the frequencies higher than f_{clock} in the Fourier spectrum of the E-population's LFP. The color saturation indicates the ratio

of the power at the frequencies f_{super} and f_{clock}. Thus, a color hue closer to green ($f_{super} : f_{clock} = 1 : 1$) or with a lower saturation implies better synchronization. By observing how the width of the range of detuning allowing synchronization varied with neuronal heterogeneity, we concluded that, generally, the neuronal heterogeneity enhanced the synchronizability of the PING rhythm by weakening the subharmonic response. Note that for $CV \in [0, 0.1]$ the synchonizability of the PING rhythm decreased slightly with neuronal heterogeneity. This was consistent with the non-monotonicity exhibited by the fmPRC seen in Fig 3.8B. The neuronal heterogeneity played a similar role in the tightness of the phase-locking as in the synchronizability (Fig 3.8D).

3.3.4. Paradoxical phase response in QIF networks and their mean-field reduction

To demonstrate the generalizability of our results beyond IF neurons, we studied the collective phase response for networks of QIF neurons, which display biologically more realistic voltage traces. All-to-all coupled networks of QIF neurons have the additional advantage – in the limit of infinitely many neurons and if the heterogeneity of the neurons is chosen to follow a Lorentzian distribution – that they can be captured by an exact mean-field theory (eMFT) that reduces the network to two coupled ordinary differential equations. These equations describe the mean voltage and the mean firing rate of the neurons [**67**, **80**] (see also [**69**]). This reduction allowed to obtain the imPRC by applying the adjoint method rather than by direct

simulation of spiking networks [**71**]. In [**57**,**71**], this methodology has been applied to study the imPRCs of both PING and ING rhythms in detail, finding good agreement with the direct simulations of the corresponding spiking networks.

Given the importance of the effective synaptic delay for the paradoxical collective phase response, we went beyond [**57**, **71**] and included an effective synaptic delay in the eMFT and studied its impact, combined with that of the neuronal heterogeneity, on the imPRC, obtained by the adjoint method, as well as the fmPRC, obtained by direct simulation of the spiking networks as well as the eMFT.

We introduced the effective synaptic delay via double-exponential synaptic interaction without including an explicit synaptic delay. We first focused on the ING rhythm. Its imPRC, obtained with the adjoint method from the eMFT, agreed well with the fmPRC obtained from weak direct perturbations of the spiking network, regardless of the sign of the perturbation (Fig 3.9A). Thus, the agreement between the fmPRC for weak perturbations and the imPRC found in [**57**, **71**] carried over to the case with effective synaptic delay. With increasing perturbation amplitude the shape of the fmPRC changed substantially, resulting in strong deviations from the imPRC (Fig 3.9B). Nevertheless, the fmPRC of the spiking network always agreed well with the fmPRC obtained with the eMFT (Fig 3.9B).

Strikingly, due to the effective delay the paradoxical phase response even arose in the imPRC (Fig 3.9A). Simulation of the eMFT showed that the paradoxical phase response was caused by the paradoxical change in the level of the within-network inhibition: as in the IF-networks with Gaussian heterogeneity, external inhibition

decreased the total within-network inhibition while external excitation increased it (Fig 3.9C). Furthermore, the amplitude of the paradoxical phase response of the imPRC from the eMFT also increased with neuronal heterogeneity (Fig 3.9D). However, in contrast to the case discussed above where the distribution of the input currents was Gaussian and the paradoxical phase response occurred only for sufficiently strong perturbations or sufficiently strong heterogeneity (Fig 3.2C), for the Lorentzian distributed input a paradoxical phase response arose in the imPRC, i.e. without a threshold for the perturbation amplitude, even for arbitrarily small neuronal heterogeneity (Fig 3.9D right). This reflects the fact that in the limit of infinitely many neurons even for small heterogeneity Δ there were always neurons in the heavy tail of the Lorentz distribution that were on the border between spiking and not spiking for whom an infinitesimal external inhibition was sufficient to suppress their spiking.

For the PING rhythm with effective synaptic delay, we investigated all possible perturbation scenarios: excitation to E-cells, inhibition to E-cells, excitation to I-cells, inhibition to I-cells. For small perturbation amplitudes the imPRC obtained with the adjoint method applied to the eMFT of the E-I network again agreed well with the fmPRC of the spiking E-I network (Fig 3.10A). We determined the dynamical regime of the eMFT in terms of the heterogeneities of the E-population (Δ_E) and of the I-population (Δ_I). Similar to the result in [**57**, **71**], the eMFT displayed a Hopf bifurcation when decreasing either neuronal heterogeneity (Fig 3.10B). Note that for very small heterogeneities the numerical solution diverged (below the orange line in Fig 3.10B, which corresponds to the black area below the white line in Fig

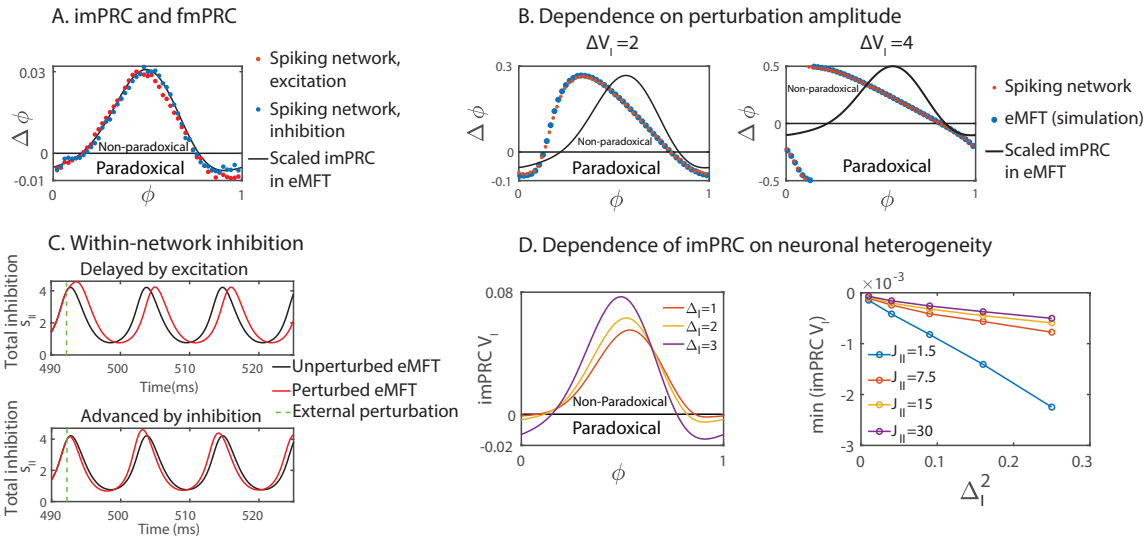

Figure 3.9. ING rhythms in heterogeneous QIF networks and their eMFT-reduction. (A) The imPRC (black line) of the eMFT multiplied by the signed perturbation strength agreed well with the fmPRCs (blue=excitation, orange=inhibition) from the spiking network simulation. (B) Even for strong perturbations, the fmPRC obtained from simulations of the eMFT agreed well with that of the spiking network. (C) As in the IF networks, the paradoxical phase response of the eMFT arose from the paradoxical change in the within-network inhibition. Top: external excitation increased the within-network inhibition. Bottom: external inhibition decreased the within-network inhibition. (D) Left: the amplitude of the paradoxical phase response of the imPRC in the eMFT increased with neuronal heterogeneity. Right: the imPRC of the eMFT exhibited a paradoxical phase response for arbitrarily weak neuronal heterogeneity. Parameters: voltage perturbations ΔV_I were made to the membrane potential or the mean potential variable $V_I(t)$ with a square-wave pulse of duration 0.02 ms. In (A), $\Delta V_I = \pm 0.2$. In (B), $\Delta V_I = 2$ (left), $\Delta V_I = 4$ (right). In (C), $\Delta V_I = 3$. In (A)-(C), $\Delta_I = 3$.

3.10C), reflecting an approach to perfect synchrony in the limit of vanishing heterogeneity. Within the oscillatory regime, we studied the influence of Δ_E and Δ_I on the fmPRC by simulating the eMFT rather than the spiking network. The paradoxical phase response, either an advance under external inhibition or a delay under external

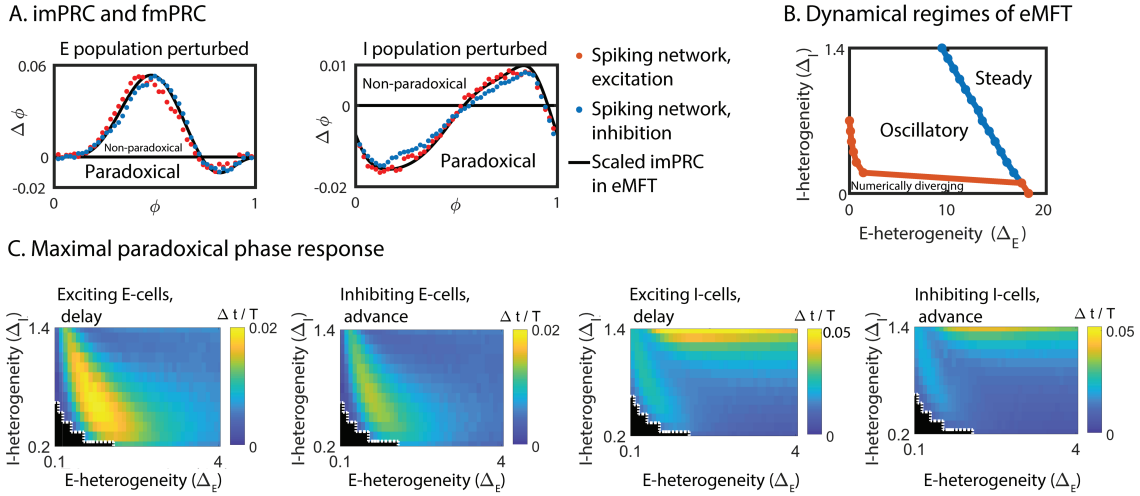

Figure 3.10. PING rhythms in heterogeneous QIF networks and their eMFT-reduction. (A) The imPRC (black line) of the eMFT multiplied by the signed perturbation strength agreed well with the fmPRCs (blue=excitation, orange=inhibition) from the spiking network simulations when perturbing the E-population (top) or the I-population (bottom). (B) Dynamical regimes of the PING rhythm in the eMFT. (C) The maximal paradoxical phase response obtained from simulations of the eMFT. Paradoxical phase response always existed. The black regions below the white dashed line correspond to the area below the orange line in (B). Parameters: voltage perturbations $\Delta V_{E,I}$ were made to the membrane potential or the mean potential variable $V_{E,I}(t)$ with a square-wave pulse of duration 0.02 ms. In (A), $\Delta V_{E,I} = \pm 0.2$, $\Delta_E = 1$, $\Delta_I = 1$. In (C), $\Delta V_{E,I} = \pm 0.2$.

excitation, existed in all perturbation scenarios (Fig 3.10C). As in the ING rhythm, it was caused by a paradoxical change in the level of the within-network inhibition.

Thus, the results of the IF networks with Gaussian heterogeneity carry over to QIF networks with Lorentzian heterogeneity and their eMFT-description.

3.4. Discussion

The key element of the mechanism driving the paradoxical phase response and the enhanced synchronization is the cooperation of the external perturbation and the effectively delayed within-network inhibition. In the ING-network a suitably timed external perturbation delays the lagging — but not the early — neurons sufficiently to allow the within-network inhibition triggered by the early neurons to keep the lagging neurons from spiking. This reduces the overall within-network inhibition and with it the duration of the cycle. Thus, the perturbation modifies the internal dynamics of the rhythm, which leads to changes in the phase of the rhythm that can dominate the immediate phase change the perturbation induces. The situation is somewhat similar to that investigated in [**62**]. There it had been pointed out that an external perturbation of a collective oscillation can lead to changes in its phase in two stages: i) an immediate change of the phases of all oscillators as a direct result of the perturbation and ii) a subsequent slower change in the collective phase resulting from the convergence of the disturbed phases back to the synchronized state. That analysis was based on a network of phase oscillators and could therefore not include a key element of our results, which is the perturbation-induced change in the dynamics within the network that is associated with a change in the number of spiking neurons and induces a change of the period of the rhythm. As discussed in [**75**, **81**], for ING-rhythms such a change in the number of spiking neurons underlies also the enhanced phase-locking found in [**74**].

Going beyond ING-rhythms, we showed that PING-rhythms can also exhibit a paradoxical phase response *via* a mechanism that is analogous to that of ING-rhythms. For that analysis we have focused on excitatory-inhibitory networks with only connections between but not within the excitatory and inhibitory populations. For excitatory inputs to the excitatory cells to generate a paradoxical phase response it is necessary that the additional spikes of the excitatory neurons that are caused by the external perturbation induce additional spikes of the inhibitory neurons. This behavior arises if the inibitory population is also allowed to be heterogeneous. Moreover, the within-network inhibition has to be strong enough to be able to suppress the spiking of lagging excitatory neurons. This is, e.g., found in mice piriform cortex, where principal neurons driven by sensory input from the olfactory bulb arriving early during a sniff recruit inhibitory interneurons via long-range recurrent connections, resulting in the global, transient suppression of subsequent cortical activity [**82**]. A characteristic feature of the paradoxical phase response of the PING rhythm is the extended cycle time following enhanced activation of the excitatory cells. A strong such correlation between the cycle time and the previous LFP amplitude has been observed for the γ-rhythm in hippocampus [**83**]. To assess whether this rhythm exhibits paradoxical phase response it would be interesting to compare the macroscopic phase response [**84**] with that of indvidual participating neurons.

In order for the global perturbation to affect the various neurons differently, they have to be at different phases in their cycle. Our analysis suggests that the specific cause for this heterogeneity in the spike times does not play an important

role. Indeed, as shown in [**73**], even fluctuating heterogeneities that are generated by noise rather than static heterogeneities reflecting intrinsic properties of neurons can enhance the synchronization of multiple γ-rhythms in interconnected networks of identical neurons. Note that the noise driving this synchronization is uncorrelated across neurons. The analysis of that system revealed the same mechanism at work as the one identified here.

In various previous analytical and computational analyses it has been found that the dynamics of the macroscopic phase of a collective oscillation can qualitatively differ from that of the microscopic phase [**61**, **64**–**66**, **72**]. Thus, for interacting groups of noisy identical phase oscillators the macroscopic phases of the groups can tend to line up with each other, even if all pair-wise interactions between individual oscillators prefer the antiphase state, and vice versa [**64**]. An analogous result has been obtained for heterogeneous populations of noiseless oscillators [**61**].

Qualitative changes have also been found in the macroscopic phase response of rhythms in noisy homogeneous networks when the noise level was changed [**65**,**66**,**72**]. Using a Fokker-Planck approach for globally coupled excitable neurons, a type-I mPRC was obtained for weak noise, where the rhythm emerges through a SNIC bifurcation, while a type-II mPRC arose for strong noise that led to a Hopf bifurcation [**65**]. A similar approach was used to obtain the imPRC via the adjoint method for an extension of the theta-model that implements conductance-based synaptic interactions. Again, although individual theta-neurons have a type-I PRC, a type-II

imPRC was obtained for the rhythm, which arose in a Hopf bifurcation [**66**]. This was also the case in an extension to networks of excitable and inhibitory neurons [**72**].

Thus, results reminiscent of those presented here have been obtained previously. However, the mechanism underlying them was not addressed in detail and remained poorly understood. We expect that our analysis will provide insight into those systems. The key element of the mechanism discussed here is that due to the dispersion of the spike times, which either results from neuronal heterogeneity or noise, the external perturbation enables the within-network inhibition to suppress the spiking of a larger number of neurons than without it. In our system this was facilitated by the delay with which spikes triggered the within-network inhibition, which allowed some neurons to escape its impact in the absence of the external perturbation, but not in its presence. Our analysis showed, however, that an explicit delay is not necessary; the effective delay resulting from a double-exponential synaptic interaction is sufficient. In fact, when reducing that effective delay the paradoxical phase response did not disappear until the delay was so short that the rhythm itself developed a strong subharmonic component and disintegrated.

Previous work on the enhancement of synchronization among γ-rhythms *via* noise-induced spiking heterogeneity has demonstrated that this enhanced synchronization does not depend sensitively on the neuron type. Comparable results were obtained also with Morris-Lecar neurons for parameters in which the periodic spiking arises from a SNIC-bifurcation, resulting in a type-I PRC for the individual neurons

as is the case for integrate-and-fire neurons, but also for parameters for which the spiking is due to a Hopf bifurcation, resulting in a type-II PRC [**73**].

In [**73**] the results were also found to be robust with respect to significant changes in the network connectivity (random instead of all-to-all) as well as the reversal potential of the inhibitory synapses, as long as the rhythm itself persisted robustly (cf. [**85**]). In fact, the coupling did not even have to be synaptic; collective oscillations of relaxation-type chemical oscillators that were coupled diffusively were also shown to exhibit noise-induced synchronization. These results suggest that the paradoxical phase response found here arises in a much wider class of macroscopic collective oscillations.

The strong paradoxical phase response that we demonstrated for heterogeneous networks allows their rhythm to synchronize with a periodic external input over a range of detuning that increases substantially with the neuronal heterogeneity. This is reminiscent of computational results for anterior cingulate cortex that investigated networks of excitatory neurons coupled via a common population of inhibitory neurons. There heterogeneity was also found to enhance the synchrony of rhythms, as measured in terms of coincident spikes within 10ms bins [**86**].

The heterogeneity-enhanced synchrony we have identified suggests that the coherence of γ-rhythms emerging in different interacting networks could also be enhanced by neuronal heterogeneity. It has been proposed that the coherence of different γ-rhythms, which has been observed to be modified by attention [**1**], plays an important

role in the communication between the corresponding networks [**55**, **78**]. Computational studies have shown that the direction of information transfer between networks depends on the relative phase of their rhythms [**56**, **57**], which can be changed by switching between different base states [**87**, **88**]. Whether the enhanced synchrony resulting from neuronal heterogeneity enhances this information transfer is still an open question.

Disrupted γ-rhythms have been observed in multiple brain regions in neurological diseases, especially Alzheimer's disease. Optogenetic and sensory periodic stimulation at γ-frequencies has been found to entrain the γ-rhythm in hippocampus and visual cortex, respectively, and has resulted in a significant reduction in total amyloid level [**89**]. Similar neuro-protective effects of entrainment by external γ-stimulation have also been found for other sensory modalities [**58**, **90**]. This suggests that γ-stimulation by sensory input might be a feasible therapeutic approach. Our results suggest a potential role of neuronal heterogeneity in this context.

From a functional perspective, it has been shown that the noise-induced synchronization mentioned above can facilitate certain learning processes [**91**]. Specifically, a read-out neuron was considered that received input from neurons in two networks *via* synapses that exhibited spike-timing dependent plasticity. The two networks were interacting with each other and each of them exhibited a γ-rhythm, albeit at different frequencies. For low noise the two rhythms were not synchronized and the read-out neuron received inputs from the two networks at uncorrelated times. These

inputs drove the plasticity inconsistently, leading only to a very slow overall evolution of the synaptic weights, if any. However, for stronger noise the two networks were synchronized, providing a more consistent spike timing that lead to substantial changes in the synaptic weights. As a result, the read-out neuron was eventually only driven by the network that had the larger natural frequency in the absence of the coupling between the networks. It is expected that synchrony by neuronal heterogeneity will have a similar impact.

CHAPTER 4

Conclusion and Outlook

4.1. Summary

In this thesis, we explored the neural mechanisms in the brain at multiple spatio-temporal scales: from a single neuron with synapses to a neural network, from long-term learning to brain rhythms.

In Chapter 2, we used computational modeling to investigate the development of orientation selectivity and its binocular matching in mouse V1. The model focused on a hypothetical neuron that received inputs from both eyes via plastic synapses. The evolution of the synaptic weights was driven by stimuli representing gratings with randomly switching orientation. In an initial phase these inputs were uncorrelated between the two eyes to mimic spontaneous retinal or thalamic activity before eye-opening [**24**]. After eye-opening the inputs were chosen to be perfectly correlated between left and right. Our model captured key experimental observations [**23**, **26**]:

(1) the matching is predominantly achieved by shifting the preferred orientation for input from the weaker eye.

(2) the resulting binocular orientation selectivity increases with decreasing mismatch.

In addition, the model provided insight into a number of further experimental observations and put forward testable predictions:

(1) The matching speed increases with initial ocular dominance, suggesting ocular dominance as a key driver of the binocular matching process.

(2) While the matching improves more slowly for cells that are more orientation-selective, the selectivity increases faster for better matched cells during the matching process. This suggests that matching drives orientation selectivity but not vice versa.

(3) There are two main routes to matching: the preferred orientations either drift towards each other or one of the orientations switches quite suddenly, involving a transient loss of binocularity, which can become permanent if it occurs towards the end of the critical period. While drifting occurs for small initial mismatch, switching is specific for large mismatch.

Furthermore, we explored how the learning process and outcome depend on the input characteristics. With binocular and potentially unmatched input synapses, most key features of the matching process were qualitatively the same as for the scenario with monocular input synapses. Surprisingly, we found that with matched binocular input synapses, the matching occurred already during the monocular vision. Complex cells in the visual system are presumably best described by binocular inputs with a modest degree of mismatch.

In Chapter 3, we have analyzed the response of collective oscillations of inhibitory and of excitatory-inhibitory networks of linear and of quadratic integrate-and-fire

neurons to external perturbations. For the QIF networks with Lorentzian heterogeneity we made extensive use of the eMFT that reduces the network dynamics to two coupled ordinary differential equations [**67**]. For ING- and PING-rhythms in all-to-all networks comprised of IF or QIF neurons, we have shown that the combination of neuronal heterogeneity and effective synaptic delay can qualitatively change the phase response compared to the phase response of the individual neurons generating the rhythm. Thus, perturbations that delay the I-cells can paradoxically advance the ING-rhythm and perturbations that advance the E-cells can delay the PING-rhythm. As a result, the macroscopic phase-response curve for finite-amplitude perturbations (fmPRC) of the rhythm can change sign as the phase of the perturbation is changed (type-II), even though the PRC of all individual cells is strictly positive (type-I). This change of the fmPRC enhances the ability of the γ-rhythm to synchronize with other rhythms.

4.2. Future Work

4.2.1. Matching of preferences in the network model

In Chapter 2, we have considered in our model only a single neuron and its feed-forward inputs. In the mammalian V1 the L2/3 and the L4 neurons are, however, part of a recurrent network. This recurrent connectivity plays a key role in the development of the ocular dominance columns and orientation maps [**20**, **34**, **36**] that are found in higher mammals like cats, ferrets, and monkeys [**92**, **93**]. Mouse V1,

however, does not exhibit such maps. In spite of that, mouse V1 exhibits stereotypical connectivity between the pyramidal cells and parvalbumin-expressing (PV) inhibitory cells. Recurrent connections between the pyramidal cells are sparse and weak. In contrast, connections from the pyramidal cells to PV cells are dense and strong [**94**, **95**]. The PV cells are less selective than most pyramidal cells [**96**], which can be explained by the dense connections from the pyramidal cells with different preferred orientations to the PV cells [**94**, **95**]. A recent computational study has explored how such connectivity emerges with homeostatic synaptic plasticity, in which the less selective PV cells are proposed to stabilize the network by preventing fluctuation in the synaptic weights [**97**]. In addition, it has been experimentally shown that the binocular matching of preferred orientations occurred only after the broadening of inhibitory tuning curves [**98**]. It would therefore be interesting to investigate the effect of the recurrent connectivity and the function of inhibitory cells during the process of binocular matching in an E-I network model capturing such connectivity with plastic synapses.

4.2.2. Matching of preferences in multisensory systems

The framework of our model in Chapter 2 can readily be applied to neurons in other multi-channel systems such as binaural auditory neurons or multisensory neurons to capture the development and matching of multiple, single-channel receptive fields that represent corresponding physical properties (e.g., orientation, position). For multisensory neurons in superior colliculus, for example, it has been shown that the

selectivity of multisensory neurons develops after the development of selectivity of its upstream unisensory neurons [**12**], which is similar to the setup in our model. The binocular vision and its ensuing matching of orientation selectivity through binocular vision in our visual cortex model corresponds to sensing the same event through different modalities simultaneously and the matching of their corresponding receptive fields. Thus, it would be interesting to study if the ideas and results developed here can carry over to explain experimental results for the development and matching of receptive fields in other sensory cortices integrating inputs across modalities [**12**].

4.2.3. Macroscopic phase response in the networks of type-II neurons

In Chapter 3, we have focused on two specific, very simple neuronal models, the linear and the quadratic leaky integrate-and-fire model with pulsatile coupling. Both have a type-I PRC, which is non-negative. This makes the paradoxical aspect of the mPRC of the rhythm easier to identify and analyze. It would be interesting to explore the dependence of the macroscopic phase response on the neuronal heterogeneity and the ensuing ability of synchronization for neurons with biphasic PRC (type-II, e.g., Hodgkin-Huxley neuron), where the sign of the phase shift of each individual neuron depends on its phase and therefore may vary from neuron to neuron for a given perturbation. We expect that the interplay between the within-network inhibition and the external perturbation can again substantially and qualitatively modify the mPRC by changing the number of neurons participating in the rhythm.

4.2.4. Macroscopic phase response in the networks of multiple subtypes of interneurons

There are multiple interneuron subtypes within the mouse visual cortex. Three major subtypes of interneurons, parvalbumin-expressing (PV), somatostatin-expressing (SOM), and vasointestinal peptide-expressing (VIP) neurons comprise 80–90% of inhibitory neurons [**99**], following typical rules of connectivity [**100**]: PV neurons preferentially inhibit one another, SOM neurons avoid one another and inhibit all other types of interneurons, VIP neurons preferentially inhibit SOM neurons, and the inhibition onto pyramidal neurons is mainly from PV and SOM neurons. PV neurons play a crucial rule in regulating the excitation-inhibition balance [**101**] and generating gamma rhythms [**102**]. SOM neurons have been shown essential to visually-induced gamma rhythms as well as the coherence between gamma rhythms in distinct V1 locations [**103**]. Moreover, VIP neurons have been reported to disinhibit the pyramidal neurons in layer 2/3 [**104**], which controls the impact of context on V1 responses [**105**]. This mechanism of disinhibition cannot be captured in a model that includes only a single population of interneurons. Theoretical studies have also been done on E-I cortical networks including diverse inhibitory populations [**106**,**107**]. It would be interesting to investigate the collective phase response in networks with such diversity of interneurons, studying the effect of the disinhibition arising from the SOM-PV, VIP-SOM connections as well as the role of the neuronal heterogeneity within each population of interneurons in the synchronization between gamma rhythms.

4.2.5. The relationship between the network dynamics and synaptic plasticity

In both Chapter 2,3, we have constrained the modeling in the neural mechanisms on a single timescale. It would be interesting to study the interaction between neural mechanisms operating on different timescales, e.g., the relationship between the network dynamics and synaptic plasticity. Mature cortical networks have been shown to operate in a 'stabilized supralinear network (SSN)' regime [**108**, **109**]. With supralinear transfer functions, these networks have strong recurrent excitatory connections, stabilized by feedback inhibition. Extended from inhibition stabilized networks (ISNs) [**110**], SSNs also display the paradoxical property that increasing excitatory input to inhibitory neurons leads to a decrease in both inhibitory and excitatory neurons' activity. That is similar to the paradoxical collective phase response we have found in Chapter 3 where the overall level of the recurrent inhibition increases with external excitation and leads to a paradoxical response. The nonlinearity of the transfer function enables SSNs to operate in two distinct regimes: a non-ISN regime for weak inputs where feedforward input dominates, and an ISN regime for stronger inputs where recurrent input dominates. It would be interesting to study the role of synaptic plasticity in this context – how and which synaptic plasticity mechanisms can make neuronal networks operate as ISNs (potentially SSNs), and how such dynamics in turn can modulate plasticity in cortical networks. The primary visual cortex, with diverse interneurons and stereotypical connectivity, experiences significant plasticity modification during the critical period [**9**], after which it operates in a

'stabilized supralinear' regime. That makes the primary visual cortex a good model to study the interaction between the synaptic plasticity and the network dynamics during the developmental phase of cortical networks.

References

[1] Conrado A Bosman, Jan-Mathijs Schoffelen, Nicolas Brunet, Robert Oostenveld, Andre M Bastos, Thilo Womelsdorf, Birthe Rubehn, Thomas Stieglitz, Peter De Weerd, and Pascal Fries. Attentional stimulus selection through selective synchronization between monkey visual areas. *Neuron*, 75:875–888, Sep 2012.

[2] Robert S. Zucker and Wade G. Regehr. Short-term synaptic plasticity. *Annu. Rev. Physiol.*, 64(1):355–405, March 2002.

[3] L. F. Abbott and Wade G. Regehr. Synaptic computation. *Nature*, 431(7010):796–803, 2004.

[4] Nicolas Y. Masse, Matthew C. Rosen, and David J. Freedman. Reevaluating the role of persistent neural activity in short-term memory. *Trends in Cognitive Sciences*, 24(3):242–258, 2020.

[5] Gina G. Turrigiano, Kenneth R. Leslie, Niraj S. Desai, Lana C. Rutherford, and Sacha B. Nelson. Activity-dependent scaling of quantal amplitude in neocortical neurons. *Nature*, 391(6670):892–896, 1998.

[6] Gina G. Turrigiano and Sacha B. Nelson. Homeostatic plasticity in the developing nervous system. *Nat Rev Neurosci*, 5(2):97–107, February 2004.

[7] Eric R. Kandel. The molecular biology of memory storage: A dialogue between genes and synapses. *Science*, 294(5544):1030, November 2001.

[8] Stefano Fusi, Patrick J. Drew, and L. F. Abbott. Cascade models of synaptically stored memories. *Neuron*, 45(4):599–611, February 2005.

[9] Bryan M. Hooks and Chinfei Chen. Circuitry underlying experience-dependent plasticity in the mouse visual system. *Neuron*, 106(1):21–36, 2020.

[10] Xize Xu, Jianhua Cang, and Hermann Riecke. Development and binocular matching of orientation selectivity in visual cortex: a computational model. *Journal of Neurophysiology*, 123(4):1305–1319, January 2020.

[11] Xize Xu and Hermann Riecke. Paradoxical phase response of gamma rhythms facilitates their entrainment in heterogeneous networks. *PLOS Computational Biology*, 17(6):e1008575, June 2021.

[12] Barry E. Stein and Benjamin A. Rowland. Organization and plasticity in multisensory integration: Early and late experience affects its governing principles. *Progress in Brain Research*, 191:145–163, 2011.

[13] Barry E. Stein and M. Alex Meredith. *The merging of the senses*. MIT Press, Cambridge, MA, US, 1993.

[14] M. T. Wallace, M. A. Meredith, and B. E. Stein. Converging influences from visual, auditory, and somatosensory cortices onto output neurons of the superior colliculus. *Journal of Neurophysiology*, 69(6):1797–1809, June 1993.

[15] Michael F. Huerta and John K. Harting. Connectional organization of the superior colliculus. *Trends in Neurosciences*, 7(8):286–289, August 1984.

[16] Veronica Fuentes-Santamaria, Juan C. Alvarado, John G. McHaffie, and Barry E. Stein. Axon morphologies and convergence patterns of projections from different sensory-specific cortices of the anterior ectosylvian sulcus onto multisensory neurons in the cat superior colliculus. *Cerebral Cortex (New York, NY)*, 19(12):2902–2915, April 2009.

[17] Michael S. Brainard and Eric I. Knudsen. Sensitive periods for visual calibration of the auditory space map in the barn owl optic tectum. *J. Neurosci.*, 18(10):3929, May 1998.

[18] Bor-Shuen Wang, Liang Feng, Mingna Liu, Xiaorong Liu, and Jianhua Cang. Environmental enrichment rescues binocular matching of orientation preference in mice that have a precocious critical period. *Neuron*, 80(1):198–209, October 2013.

[19] Joshua A. Gordon and Michael P. Stryker. Experience-dependent plasticity of binocular responses in the primary visual cortex of the mouse. *Journal of Neuroscience*, 16(10):3274–3286, 1996.

[20] K. D. Miller, J. B. Keller, and M. P. Stryker. Ocular dominance column development - analysis and simulation. *Science*, 245(4918):605–615, August 1989.

[21] David Hansel and Carl van Vreeswijk. The mechanism of orientation selectivity in primary visual cortex without a functional map. *The Journal of Neuroscience*, 32(12):4049–4064, 2012.

[22] C. Clopath, L. Büsing, E. Vasilaki, and W. Gerstner. Connectivity reflects coding: a model of voltage-based STDP with homeostasis. *Nature Neuroscience*, 13(3):344–U19, March 2010.

[23] Bor-Shuen Wang, Rashmi Sarnaik, and Jianhua Cang. Critical period plasticity matches binocular orientation preference in the visual cortex. *Neuron*, 65(2):246, January 2010.

[24] J. Sebastian Espinosa and Michael P. Stryker. Development and plasticity of the primary visual cortex. *Neuron*, 75(2):230–249, July 2012.

[25] Taro Toyoizumi, Hiroyuki Miyamoto, Yoko Yazaki-Sugiyama, Nafiseh Atapour, Takao K. Hensch, and Kenneth D. Miller. A theory of the transition to critical period plasticity: Inhibition selectively suppresses spontaneous activity. *Neuron*, 80(1):51–63, October 2013.

[26] Jared N Levine, Hui Chen, Yu Gu, and Jianhua Cang. Environmental enrichment rescues binocular matching of orientation preference in the mouse visual cortex. *The Journal of Neuroscience*, 37:5822–5833, June 2017.

[27] Romain Brette and Wulfram Gerstner. Adaptive exponential integrate-and-fire model as an effective description of neuronal activity. *Journal of Neurophysiology*, 94(5):3637–3642, 2005.

[28] Laurent Badel, Sandrine Lefort, Romain Brette, Carl C. H. Petersen, Wulfram Gerstner, and Magnus J. E. Richardson. Dynamic I-V curves are reliable predictors of naturalistic pyramidal-neuron voltage traces. *Journal of Neurophysiology*, 99(2):656–666, 2008.

[29] Xinyu Zhao, Mingna Liu, and Jianhua Cang. Sublinear binocular integration preserves orientation selectivity in mouse visual cortex. *Nature Communications*, 4:2088–2088, 2013.

[30] Cristopher M. Niell and Michael P. Stryker. Highly selective receptive fields in mouse visual cortex. *The Journal of Neuroscience*, 28(30):7520–7536, July 2008.

[31] Jennifer L. Hoy and Cristopher M. Niell. Layer-specific refinement of visual cortex function after eye opening in the awake mouse. *The Journal of Neuroscience*, 35(8):3370–3383, December 2015.

[32] Liming Tan, Elaine Tring, Dario L. Ringach, S. Lawrence Zipursky, and Joshua T. Trachtenberg. Vision changes the cellular composition of binocular circuitry during the critical period. *Neuron*, 108(4):735–747.e6, 2020.

[33] T. D. Mrsic-Flogel, S. B. Hofer, K. Ohki, R. C. Reid, T. Bonhoeffer, and M. Hubener. Homeostatic regulation of eye-specific responses in visual cortex during ocular dominance plasticity rid b-9481-2009. *Neuron*, 54(6):961–972, June 2007.

[34] K. D. Miller. A model for the development of simple cell receptive-fields and the ordered arrangement of orientation columns through activity-dependent competition between on-and off-center inputs. *J. Neurosci.*, 14(1):409–441, January 1994.

[35] C. Piepenbrock, H. Ritter, and K. Obermayer. The joint development of orientation and ocular dominance: Role of constraints. *Neural Comput.*, 9(5):959–970, July 1997.

[36] E. Erwin and K. D. Miller. Correlation-based development of ocularly matched orientation and ocular dominance maps: Determination of required input activities. *J. Neurosci.*, 18(23):9870–9895, December 1998.

[37] E. L. Bienenstock, L. N. Cooper, and P. W. Munro. Theory for the development of neuron selectivity: orientation specificity and binocular interaction in visual cortex. *J. Neurosci.*, 2:32, 1982.

[38] E. E. Clothiaux, M. F. Bear, and L. N. Cooper. Synaptic plasticity in visual-cortex - comparison of theory with experiment. *J. Neurophysiol.*, 66(5):1785–1804, 1991.

[39] B. Chapman and M. P. Stryker. Development of orientation selectivity in ferret visual cortex and effects of deprivation. *J. Neurosci.*, 13(12):5251, December 1993.

[40] Michael C. Crair, Deda C. Gillespie, and Michael P. Stryker. The role of visual experience in the development of columns in cat visual cortex. *Science*, 279(5350):566, January 1998.

[41] Kenta M. Hagihara, Tomonari Murakami, Takashi Yoshida, Yoshiaki Tagawa, and Kenichi Ohki. Neuronal activity is not required for the initial formation and maturation of visual selectivity. *Nature Neuroscience*, 18:1780, November 2015.

[42] Michela Fagiolini and Takao K. Hensch. Inhibitory threshold for critical-period activation in primary visual cortex. *Nature*, 404:183, March 2000.

[43] L. Tan, J. T. Trachtenberg, and D. L. Ringach. Diverse developmental trajectories of single identified pyramidal neurons during the critical period in the visual cortex. *Society for Neuroscience, Nanosymposium 353.03*, 2018.

[44] David A. Arroyo and Marla B. Feller. Spatiotemporal features of retinal waves instruct the wiring of the visual circuitry. *Frontiers in Neural Circuits*, 10:54–54, July 2016.

[45] Kurt A. Sailor, Matthew T. Valley, Martin T. Wiechert, Hermann Riecke, Gerald J. Sun, Wayne Adams, James C. Dennis, Shirin Sharafi, Guo-Li Ming, Hongjun Song, and Pierre-Marie Lledo. Persistent structural plasticity optimizes sensory information processing in the olfactory bulb. *Neuron*, 91(2):384–396, July 2016.

[46] H. Bruesselbach, D. C. Jones, M. S. Mangir, M. Minden, and J. L. Rogers. Self-organized coherence in fiber laser arrays. *Optics Letters*, 30(11):1339–1341, June 2005.

[47] K. Wiesenfeld, P. Colet, and S. H. Strogatz. Synchronization transitions in a disordered Josephson series array. *Phys. Rev. Lett.*, 76(3):404–407, January 1996.

[48] C. Liu, D. R. Weaver, S. H. Strogatz, and S. M. Reppert. Cellular construction of a circadian clock: Period determination in the suprachiasmatic nuclei. *Cell*, 91(6):855–860, December 1997.

[49] O. F. Venzin and A. C. Oates. What are you synching about? emerging complexity of notch signaling in the segmentation clock. *Developmental Biology*, 460(1):40–54, April 2020.

[50] X.-J. Wang. Neurophysiological and computational principles of cortical rhythms in cognition. *Physiol. Rev.*, 90(3):1195–1268, July 2010.

[51] Christoph Börgers, Steven Epstein, and Nancy J. Kopell. Background gamma rhythmicity and attention in cortical local circuits: a computational study. *Proc Natl Acad Sci U S A*, 102(19):7002–7007, May 2005.

[52] C. Börgers and N.J. Kopell. Gamma oscillations and stimulus selection. *Neural Comput*, 20(2):383–414, Feb 2008.

[53] M. J. Roberts, E. Lowet, N. M. Brunet, M. Ter Wal, P. Tiesinga, P. Fries, and P. De Weerd. Robust gamma coherence between macaque V1 and V2 by dynamic frequency matching. *Neuron*, 78(3):523–536, May 2013.

[54] G. Buzsaki and E. W. Schomburg. What does gamma coherence tell us about inter-regional neural communication? *Nature Neuroscience*, 18(4):484–489, April 2015.

[55] Pascal Fries. Rhythms for cognition: Communication through coherence. *Neuron*, 88:220–235, Oct 2015.

[56] Agostina Palmigiano, Theo Geisel, Fred Wolf, and Demian Battaglia. Flexible information routing by transient synchrony. *Nature Neuroscience*, 20:1014–1022, July 2017.

[57] Gregory Dumont and Boris Gutkin. Macroscopic phase resetting-curves determine oscillatory coherence and signal transfer in inter-coupled neural circuits. *PLoS Computational Biology*, 15:e1007019, May 2019.

[58] Chinnakkaruppan Adaikkan, Steven J Middleton, Asaf Marco, Ping-Chieh Pao, Hansruedi Mathys, David Nam-Woo Kim, Fan Gao, Jennie Z Young, Ho-Jun Suk, Edward S Boyden, Thomas J McHugh, and Li-Huei Tsai. Gamma entrainment binds higher-order brain regions and offers neuroprotection. *Neuron*, 102:929–943.e8, June 2019.

[59] N. W. Schultheiss and R. J. Butera. *Phase Response Curves in Neuroscience*. Springer, 2012.

[60] E. Brown, J. Moehlis, and P. Holmes. On the phase reduction and response dynamics of neural oscillator populations. *Neural Comput.*, 16(4):673–715, April 2004.

[61] Yoji Kawamura, Hiroya Nakao, Kensuke Arai, Hiroshi Kori, and Yoshiki Kuramoto. Phase synchronization between collective rhythms of globally coupled oscillator groups: noiseless nonidentical case. *Chaos (Woodbury, N.Y.)*, 20:043110, December 2010.

[62] Zoran Levnajic and Arkady Pikovsky. Phase resetting of collective rhythm in ensembles of oscillators. *Physical Review. E, Statistical, nonlinear, and soft matter physics*, 82:056202, November 2010.

[63] Y. Kawamura, H. Nakao, K. Arai, H. Kori, and Y. Kuramoto. Collective phase sensitivity. *Phys. Rev. Lett.*, 101(2):024101, July 2008.

[64] Y. Kawamura, H. Nakao, K. Arai, H. Kori, and Y. Kuramoto. Phase synchronization between collective rhythms of globally coupled oscillator groups: Noisy identical case. *Chaos*, 20(4):043109, December 2010.

[65] Yoji Kawamura, Hiroya Nakao, and Yoshiki Kuramoto. Collective phase description of globally coupled excitable elements. *Physical Review. E, Statistical, nonlinear, and soft matter physics*, 84:046211, October 2011.

[66] Kiyoshi Kotani, Ikuhiro Yamaguchi, Lui Yoshida, Yasuhiko Jimbo, and G Bard Ermentrout. Population dynamics of the modified theta model: macroscopic phase reduction and bifurcation analysis link microscopic neuronal interactions to macroscopic gamma oscillation. *J R Soc Interface*, 11(95):20140058, 2014.

[67] Ernest Montbrió, Diego Pazó, and Alex Roxin. Macroscopic description for networks of spiking neurons. *Phys. Rev. X*, 5:021028, Jun 2015.

[68] E. Ott and T. M. Antonsen. Low dimensional behavior of large systems of globally coupled oscillators. *Chaos*, 18(3):037113, September 2008.

[69] T. B. Luke, E. Barreto, and P. So. Complete classification of the macroscopic behavior of a heterogeneous network of theta neurons. *Neural Computation*, 25(12):3207–3234, December 2013.

[70] K. M. Hannay, V. Booth, and D. B. Forger. Collective phase response curves for heterogeneous coupled oscillators. *Physical Review E*, 92(2):022923, August 2015.

[71] Gregory Dumont, G Bard Ermentrout, and Boris Gutkin. Macroscopic phase-resetting curves for spiking neural networks. *Physical Review E*, 96:042311, October 2017.

[72] A. Akao, Y. Ogawa, Y. Jimbo, G. B. Ermentrout, and K. Kotani. Relationship between the mechanisms of gamma rhythm generation and the magnitude of the macroscopic phase response function in a population of excitatory and inhibitory modified quadratic integrate-and-fire neurons. *Physical Review E*, 97(1):012209, January 2018.

[73] John Hongyu Meng and Hermann Riecke. Synchronization by uncorrelated noise: interacting rhythms in interconnected oscillator networks. *Scientific Reports*, 8:6949, May 2018.

[74] J. A. White, M. I. Banks, R. A. Pearce, and N. J. Kopell. Networks of interneurons with fast and slow gamma-aminobutyric acid type a (gaba(a)) kinetics provide substrate for mixed gamma-theta rhythm. *Proceedings of the National Academy of Sciences of the United States of America*, 97(14):8128–8133, July 2000.

[75] A. K. Serenevy and N. J. Kopell. Effects of heterogeneous periodic forcing on inhibitory networks. *SIAM Journal on Applied Dynamical Systems*, 12(3):1649–1684, 2013.

[76] N. Brunel and X. J. Wang. What determines the frequency of fast network oscillations with irregular neural discharges? I. Synaptic dynamics and excitation-inhibition balance. *J. Neurophysiol.*, 90(1):415–430, July 2003.

[77] E. M. Izhikevich. *Dynamical Systems in Neuroscience: the Geometry of Excitability and Bursting*. MIT Press, 2005.

[78] P. Fries. A mechanism for cognitive dynamics: Neuronal communication through neuronal coherence. *Trends Cogn. Sci*, 9(10):474–480, October 2005.

[79] Marlene Bartos, Imre Vida, and Peter Jonas. Synaptic mechanisms of synchronized gamma oscillations in inhibitory interneuron networks. *Nature Reviews Neuroscience*, 8(1):45–56, January 2007.

[80] E. Montbrio and D. Pazo. Exact mean-field theory explains the dual role of electrical synapses in collective synchronization. *Physical Review Letters*, 125(24):248101, December 2020.

[81] Jonathan Cannon, Michelle M McCarthy, Shane Lee, Jung Lee, Christoph Börgers, Miles A Whittington, and Nancy Kopell. Neurosystems: brain rhythms and cognitive processing. *The European Journal of Neuroscience*, 39:705–719, March 2014.

[82] Kevin A Bolding and Kevin M Franks. Recurrent cortical circuits implement concentration-invariant odor coding. *Science (New York, N.Y.)*, 361, September 2018.

[83] B. V. Atallah and M. Scanziani. Instantaneous modulation of gamma oscillation frequency by balancing excitation with inhibition. *Neuron*, 62(4):566–577, May 2009.

[84] T. Akam, I. Oren, L. Mantoan, E. Ferenczi, and D. M. Kullmann. Oscillatory dynamics in the hippocampus support dentate gyrus-ca3 coupling. *Nature Neuroscience*, 15(5):763–768, May 2012.

[85] Christoph Börgers, Martin Krupa, and Stan Gielen. The response of a classical Hodgkin-Huxley neuron to an inhibitory input pulse. *J. Comput. Neurosci.*, 28(3):509–526, June 2010.

[86] N. E. Adams, J. S. Sherfey, N. J. Kopell, M. A. Whittington, and F. E. N. LeBeau. Hetereogeneity in neuronal intrinsic properties: A possible mechanism for hub-like properties of the rat anterior cingulate cortex during network activity. *Eneuro*, 4(1):UNSP e0313–16.2017, January 2017.

[87] Annette Witt, Agostina Palmigiano, Andreas Neef, Ahmed El Hady, Fred Wolf, and Demian Battaglia. Controlling the oscillation phase through precisely timed closed-loop optogenetic stimulation: a computational study. *Front Neural Circuits*, 7:49, 2013.

[88] C. Kirst, M. Timme, and D. Battaglia. Dynamic information routing in complex networks. *Nature Communications*, 7:11061, April 2016.

[89] H. F. Iaccarino, A. C. Singer, A. J. Martorell, A. Rudenko, F. Gao, T. Z. Gillingham, H. Mathys, J. Seo, O. Kritskiy, F. Abdurrob, C. Adaikkan, R. G. Canter, R. Rueda, E. N. Brown, E. S. Boyden, and L. H. Tsai. Gamma frequency entrainment attenuates amyloid load and modifies microglia. *Nature*, 540(7632):230–+, December 2016.

[90] Anthony J Martorell, Abigail L Paulson, Ho-Jun Suk, Fatema Abdurrob, Gabrielle T Drummond, Webster Guan, Jennie Z Young, David Nam-Woo Kim, Oleg Kritskiy, Scarlett J Barker, Vamsi Mangena, Stephanie M Prince, Emery N Brown, Kwanghun Chung, Edward S Boyden, Annabelle C Singer, and Li-Huei Tsai. Multi-sensory gamma stimulation ameliorates alzheimer's-associated pathology and improves cognition. *Cell*, 177:256–271.e22, April 2019.

[91] John H. Meng and Hermann Riecke. Synchronization by uncorrelated noise: interacting rhythms in interconnected neuronal networks. *BMC Neuroscience*, 19 (Suppl 2):116, 2018.

[92] D. H. Hubel and T. N. Wiesel. Receptive fields and functional architecture of monkey striate cortex. *The Journal of Physiology*, 195(1):215–243, March 1968.

[93] V. B. Mountcastle. The columnar organization of the neocortex. *Brain*, 120(4):701–722, April 1997.

[94] Sonja B. Hofer, Ho Ko, Bruno Pichler, Joshua Vogelstein, Hana Ros, Hongkui Zeng, Ed Lein, Nicholas A. Lesica, and Thomas D. Mrsic-Flogel. Differential connectivity and response dynamics of excitatory and inhibitory neurons in visual cortex. *Nature Neuroscience*, 14(8):1045–1052, 2011.

[95] Davi D. Bock, Wei-Chung Allen Lee, Aaron M. Kerlin, Mark L. Andermann, Greg Hood, Arthur W. Wetzel, Sergey Yurgenson, Edward R. Soucy, Hyon Suk Kim, and R. Clay Reid. Network anatomy and in vivo physiology of visual cortical neurons. *Nature*, 471(7337):177–182, 2011.

[96] Kazuhiro Sohya, Katsuro Kameyama, Yuchio Yanagawa, Kunihiko Obata, and Tadaharu Tsumoto. Gabaergic neurons are less selective to stimulus orientation than excitatory neurons in layer ii/iii of visual cortex, as revealed by in vivo functional Ca^{2+} imaging in transgenic mice. *Journal of Neuroscience*, 27(8):2145–2149, 2007.

[97] Jacopo Bono. Synaptic plasticity: From single cell to microcircuit. *Ph.D. thesis*, 2017.

[98] Sandra J. Kuhlman, Elaine Tring, and Joshua T. Trachtenberg. Fast-spiking interneurons have an initial orientation bias that is lost with vision. *Nature Neuroscience*, 14(9):1121–1123, 2011.

[99] Bernardo Rudy, Gordon Fishell, SooHyun Lee, and Jens Hjerling-Leffler. Three groups of interneurons account for nearly 100gabaergic neurons. *Devel Neurobio*, 71(1):45–61, January 2011.

[100] Carsten K. Pfeffer, Mingshan Xue, Miao He, Z. Josh Huang, and Massimo Scanziani. Inhibition of inhibition in visual cortex: the logic of connections between molecularly distinct interneurons. *Nature Neuroscience*, 16(8):1068–1076, 2013.

[101] Mingshan Xue, Bassam V. Atallah, and Massimo Scanziani. Equalizing excitation-inhibition ratios across visual cortical neurons. *Nature*, 511(7511):596–600, 2014.

[102] Marlene Bartos, Imre Vida, and Peter Jonas. Synaptic mechanisms of synchronized gamma oscillations in inhibitory interneuron networks. *Nature Reviews Neuroscience*, 8(1):45–56, 2007.

[103] Julia Veit, Richard Hakim, Monika P. Jadi, Terrence J. Sejnowski, and Hillel Adesnik. Cortical gamma band synchronization through somatostatin interneurons. *Nature Neuroscience*, 20(7):951–959, 2017.

[104] Yu Fu, Jason M. Tucciarone, J. Sebastian Espinosa, Nengyin Sheng, Daniel P. Darcy, Roger A. Nicoll, Z. Josh Huang, and Michael P. Stryker. A cortical circuit for gain control by behavioral state. *Cell*, 156(6):1139–1152, 2014.

[105] Andreas J. Keller, Mario Dipoppa, Morgane M. Roth, Matthew S. Caudill, Alessandro Ingrosso, Kenneth D. Miller, and Massimo Scanziani. A disinhibitory circuit for contextual modulation in primary visual cortex. *Neuron*, 108(6):1181–1193.e8, 2020.

[106] Ashok Litwin-Kumar, Robert Rosenbaum, and Brent Doiron. Inhibitory stabilization and visual coding in cortical circuits with multiple interneuron subtypes. *Journal of Neurophysiology*, 115(3):1399–1409, January 2016.

[107] Hannah Bos, Anne-Marie Oswald, and Brent Doiron. Untangling stability and gain modulation in cortical circuits with multiple interneuron classes. *bioRxiv*, page 2020.06.15.148114, January 2020.

[108] Daniel B. Rubin, Stephen D. Van Hooser, and Kenneth D. Miller. The stabilized supralinear network: A unifying circuit motif underlying multi-input integration in sensory cortex. *Neuron*, 85(2):402–417, 2015.

[109] Guillaume Hennequin, Yashar Ahmadian, Daniel B. Rubin, Máté Lengyel, and Kenneth D. Miller. The dynamical regime of sensory cortex: Stable dynamics around a single stimulus-tuned attractor account for patterns of noise variability. *Neuron*, 98(4):846–860.e5, 2018.

[110] Hirofumi Ozeki, Ian M. Finn, Evan S. Schaffer, Kenneth D. Miller, and David Ferster. Inhibitory stabilization of the cortical network underlies visual surround suppression. *Neuron*, 62(4):578–592, 2009.